Non-Reflecting Boundary Conditions for Time Domain Simulations of Unsteady Turbomachinery Flows

Dissertation
zur
Erlangung des Grades
Doktor-Ingenieur

der
Fakultät für Maschinenbau
der Ruhr-Universität Bochum

von

Daniel Schlüß

aus Bocholt

Bochum 2023

Abstract

This thesis presents the implementation of a spectral, non-reflecting boundary condition (NRBC) for time-marching, unsteady simulations of flows in turbomachinery components. It is well known that reflections from artificial boundaries can impair the prediction of unsteady flow phenomena. In the context of turbomachinery flows, some frequency domain methods for the most part overcome this problem using spectral NRBCs. Since these NRBCs are non-local in space and time, a transfer to time domain solvers is not straightforward. Challenges for a time domain implementation are highlighted and a detailed description of the underlying theory as well as of the specific implementation is given. This work particularly addresses time domain-related aspects of the implementation.

The NRBC presented in this work is exact for two-dimensional flows that satisfy the linearized Euler equations. For three-dimensional, nonlinear, viscous flows, the NRBC is approximately non-reflecting.

This work includes an extensive validation of the NRBC exhibiting substantially reduced reflections in comparison to widely-used, local approximations of this NRBC. The validation section comprises three basic, two-dimensional test cases: a transonic turbine cascade, the propagation of a single, acoustic mode in a circular duct and a popular flutter test case known as tenth standard configuration. Moreover, this thesis shows the application of the spectral NRBC to the flutter analysis of a transonic steam turbine blade and to blade row interactions in a modern, transonic compressor. These realistic configurations confirm the increased accuracy due to reduction of artificial reflections and additionally demonstrate the necessary stability of the implemented NRBC.

Therefore, this thesis presents a reliable, accurate NRBC and, thus, offers a contribution to more accurate time domain simulations for real-world research and design tasks.

Zusammenfassung

In dieser Arbeit wird die Implementierung einer spektralen, nichtreflektierenden Randbedingung (NRBC, engl.: non-reflecting boundary condition) für instationäre Zeitbereichssimulationen von Strömungen in Turbomaschinenkomponenten vorgestellt. Es ist allgemein bekannt, dass Reflektionen an künstlichen Rändern die Vorhersage instationärer Strömungsphänomene beeinträchtigen können. Im Kontext von Turbomaschinenströmungen beheben einige Frequenzbereichsmethoden dieses Problem mit spektralen NRBCs im Wesentlichen. Da diese NRBCs räumlich und zeitlich nicht lokal sind, ist eine Übertragung auf Zeitbereichslöser nicht einfach. Die Herausforderungen für eine Implementierung im Zeitbereich werden erläutert und die zugrundeliegende Theorie sowie die konkrete Implementierung detailliert vorgestellt. Dabei wird insbesondere auf die Aspekte eingegangen, die sich aus der Implementierung in ein Zeitbereichsverfahren ergeben.

Die in dieser Arbeit vorgestellte nichtreflektierende Randbedingung ist exakt für zweidimensionale Strömungen, die durch die linearisierten Euler-Gleichungen beschrieben werden können. Für dreidimensionale, nichtlineare, viskose Strömungen ist die NRBC näherungsweise nichtreflektierend.

Eine umfassende Validierung der nichtreflektierenden Randbedingung zeigt, dass diese im Vergleich zu weit verbreiteten, lokalen Approximationen dieser NRBC wesentlich geringere Reflektionen aufweist. Der Validierungsteil umfasst drei grundlegende, zweidimensionale Testfälle: eine transsonische Turbinenkaskade, die Ausbreitung einer einzelnen akustischen Mode in einem Ringkanal und einen weit verbreiteten Flattertestfall, bekannt als zehnte Standardkonfiguration. Darüber hinaus wird in dieser Arbeit die Anwendung der spektralen NRBC auf die Flatteranalyse einer transsonischen Dampfturbinenschaufel und auf die Schaufelreiheninteraktion in einem modernen, transsonischen Verdichter gezeigt. Diese realistischen Konfigurationen bestätigen die Genauigkeitssteigerung durch Reduktion künstlicher Reflexionen und demonstrieren weiterhin die Stabilität der implementierten NRBC.

Somit stellt diese Arbeit eine tatsächlich praxistaugliche und zuverlässige, nichtreflektierende Randbedingung vor und leistet damit einen Beitrag zu genaueren Zeitbereichssimulationen für reale Forschungs- und Auslegungsaufgaben.

Vorwort und Danksagung

Contents

Nomenclature

Latin symbols

a	Speed of sound
A_f	Cell face area
b	Blade span / thickness of quasi 2D streamsurface
c	Chord length
c_p, c_v	Isobaric and isochoric specific heat capacities
d_{max}	Maximum displacement of structural mode
d	Distance between boundary surface and leading/trailing edge
E	Specific total energy
F, G, H	Vectors of fluxes in x-,y- an z-direction (conservative variables)
$\mathcal{F}$	Flux vector $(F, G, H)^T$
f	Frequency
h_t	Specific stagnation enthalpy
$\mathbf{i}$	Imaginary unit
I	Identity matrix
k	Boundary-normal (angular) wavenumber in radians per unit distance
l	Circumferential (angular) wavenumber in radians per unit distance
l_i	i-th left eigenvector
L	Matrix of left eigenvectors to dispersion relation, Inverse of R
m	Non-dimensional circumferential wavenumber, a.k.a. (signed) nodal diameter ($m = lr$)
$\dot{m}$	Mass flow
Ma	Mach number
Ma_{is}	Isentropic Mach number
$\mathbb{N}$	Set of natural numbers
N	Number of time steps to resolve one fundamental period
n	Surface-normal unit vector
p	Pressure
p_{dyn}	Dynamic pressure at entry (compressible definition)
p_t	Stagnation pressure
P	Power
P	Pitch: arc length between either two blades or circumferential extent of a computational domain
Pr	Prandtl number
Pr_t	Turbulent Prandtl number
q	Vector of primitive variables
r	Radius
r_i	i-th right eigenvector
R	Matrix of right eigenvectors to dispersion relation
R	Specific ideal gas constant
$\mathrm{Re}\,q, \mathrm{Im}\,q$	Real and imaginary part of a complex quantity q

s	Specific entropy
t	Time
T	Period associated with fundamental frequency
T	Temperature
T_t	Stagnation temperature
U	Vector of conservative variables
u, v, w	Velocity components along coordinates x, y and z
u_g, v_g, w_g	Group velocity components
$u_\varphi, v_\varphi, w_\varphi$	Phase velocity components
V	Velocity vector
V_c	Cell volume
W_{aero}	Aerodynamic work per cycle
x	Coordinate perpendicular to boundary or axial position
y	Circumferential coordinate ($y = r\vartheta$)
y^+	Non-dimensional wall distance
z	Coordinate tangent to boundary, but perpendicular to y
$\mathbb{Z}$	Set of integers

Greek symbols

$\alpha_{rad}, \alpha_{circ}$	Radial and circumferential flow angles
$\hat{\alpha}$	Vector of modal amplitudes α_i
α	Blade pitching angle
γ	Heat capacity ratio
γ_{geom}	Stagger angle
Γ	Reflection coefficient ($\hat{p}^{in}/\hat{p}^{out}$)
δ_{ij}	Kronecker delta
η_{ts}	Isentropic efficiency based on
	total inlet and static outlet quantities
κ	Turbulent kinetic energy
λ	Thermal conductivity
μ	Dynamic viscosity
μ_t	Eddy viscosity
ϱ	Density
σ	Inter-blade phase angle (IBPA)
σ_0	Minimum nozzle cross-section (throat)
ξ	Cut-off ratio (ω_{crit}/ω), $\xi > 1$: cut-off
Ξ	Non-dimensional aerodynamic damping coefficient
Ψ	Structural eigenmode
ω	Angular frequency
ω_c	Acoustic resonance (angular) frequency
ω^*	Reduced frequency ($(\omega\,c)\,/\,(2\|V\|)$)

Subscripts, superscripts and diacritics

R_{1D}, L_{1D}	One-dimensional eigenvector matrices,
	backward and forward characteristics transformation matrix
q_{abs}	q in the absolute/stationary frame of reference
q_c	State in a cell
q_f	State at a boundary face
q_i	State in boundary-adjacent, inner cell
q_o	State in boundary-adjacent, outer cell (ghost cell)

$\hat{q}$	Fourier coefficient of q
$\overline{q}$	Time-mean area average of q
$\widetilde{q}$	Instantaneous area average of q
F^E	Convective/Euler portion of flux vector F
F^D	Diffusive portion of flux vector F
q^F	Flux or mixed-out average of q
q^H	Hermitian transpose of q
q^n	Flow state at discrete time step n
q'	Disturbance in q from $\overline{q}$
$x^{in,out}$	Incoming and outgoing components of a vector x or associated rows and columns of a matrix x

Abbreviations

BPF	Blade passing frequency
CFD	Computational fluid dynamics
DFT	Discrete Fourier transform
DLR	German Aerospace Center (ger.: Deutsches Zentrum für Luft- und Raumfahrt)
DNS	Direct numerical simulation
FFT	Fast Fourier transform
HB	Harmonic balance
HPC	High pressure compressor
IBPA	Inter-blade phase angle
IGV	Inlet guide vane
KTH	KTH Royal Institute of Technology (Kungliga Tekniska högskolan)
LE	Leading edge
LES	Large eddy simulation
LPT	Low pressure turbine
MPI	Message-Passing Interface
NRBC	Non-reflecting boundary condition
NSV	Non-synchronous vibration
PDE	Partial differential equations
PML	Perfectly matched layer
(U)RANS	(Unsteady) Reynolds-averaged Navier-Stokes
SAF	Sustainable aviation fuels
TE	Trailing edge
TMTF	Turning mid turbine frame
VKI	von Karman Institute for Fluid Dynamics
VPF	Vane passing frequency

1 Introduction

1.1 Motivation

1.1.1 The need for accurate flow simulation tools

The aviation industry is facing massive, technological challenges today. On the one hand, long-term forecasts still predict about 5 % annular growth rate in global air traffic, primarily fueled by economical growth and social participation in countries of the Global South. On the other hand, the need to mitigate the climate change demands a swift and large-scale reduction of CO_2 emissions. In order to comply with the European Green Deal, i.e. becoming climate neutral by 2050, German Aerospace Center (DLR) has recently updated its aviation strategy (see German Aerospace Center, 2021).
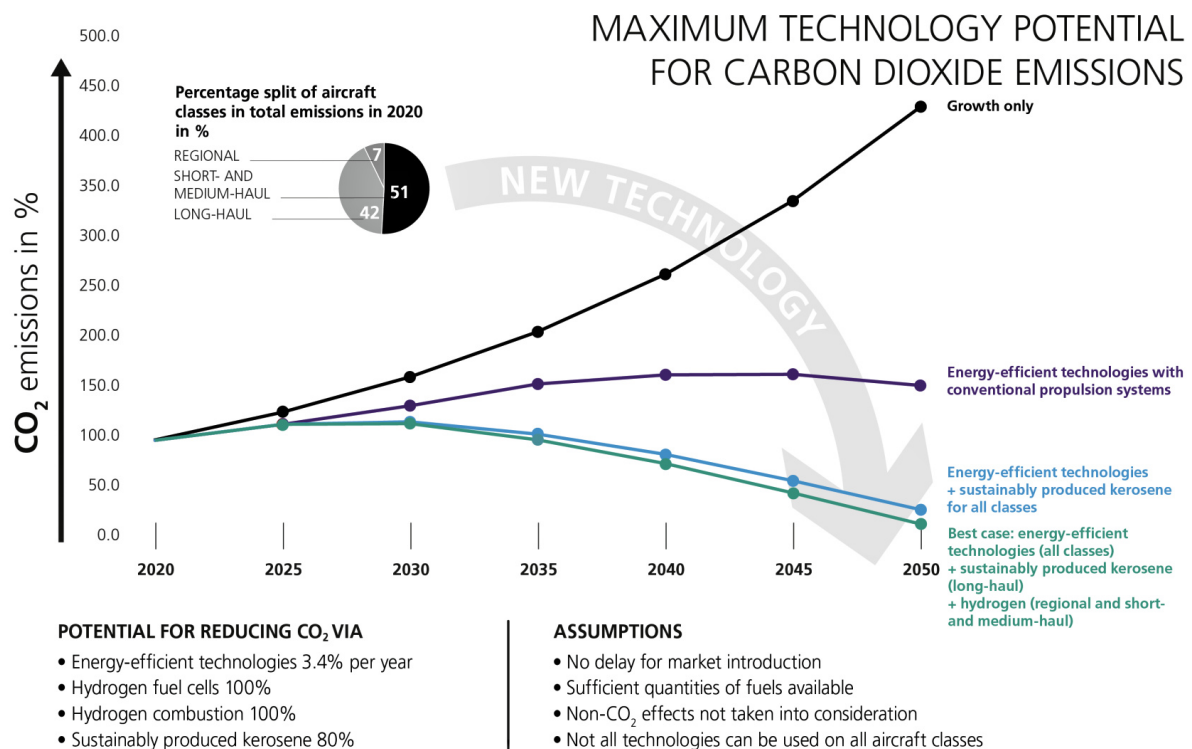
Figure 1.1: Estimation of maximum potential for CO_2 savings with new technologies according to DLR's 2021 aviation strategy. (from: German Aerospace Center (2021), CC BY-NC-ND 3.0)

Figure 1.1 displays how CO_2 emission could develop until 2050 in a best case scenario according to DLR's aviation strategy. Although the public debate is primarily concerned with electric propulsion and aviation fuel cells, the figure underlines the strong

necessity to achieve substantial efficiency improvements for conventionally propelled aircraft because it is assumed that the former technologies might not be applicable to long-haul aviation and possibly only partially applicable to medium-haul aviation. This leaves a targeted, average, annual efficiency gain of more than 3 % to airframe and conventional engine technology advancements.

Since the term *conventional* refers to combustion of kerosene or sustainable aviation fuels (SAF) in this context, DLR's strategy does include advanced core engine, propulsion and airframe integration concepts to meet this ambitious goal rather than just gradual enhancements of existing turbofan configurations. Possibly, hydrogen fueled gas turbines could lead to additional technology demands.

In order to realize the required CO_2 reduction on schedule, academia and industries will have to accomplish revolutionary developments in relatively short time compared to past technological advancements in aviation, surpassed maybe only by the rapid progress in aviation technology during and due to World War 2 and the early Cold War. In contrast to evolutionary technology development, which often relies on a lot of existing experience, high fidelity simulation and design tools are needed to break new ground more quickly. Such tools can reduce the required amount of costly and time-consuming experimental testing and help gain a deeper understanding of new or early technologies.

Additionally, there is still a need to further improve existing, very mature technology. Here, more accurate or more comprehensive computational models can play a key role e.g. in reducing uncertainties that have to be respected with generous safety margins today or prevent more radical designs.

1.1.2   Frequency and time domain methods for unsteady flow phenomena

Modern turbine and compressor design strategies tend towards lighter and more compact components with high aerodynamic loading. This implies less structural damping while unsteady blade row interactions become more pronounced (see Vahdati *et al.*, 2019). Flutter and forced response analysis have predominantly been performed by means of time-linearized methods for the last decades (see e.g. Whitehead, 1982; Hall & Crawley, 1989; Kahl & Klose, 1993; Clark & Hall, 1999; Petrie-Repar *et al.*, 2007; Kersken *et al.*, 2012). Dowell (2015) predicts in his popular textbook on aeroelasticity that nonlinear effects and, hence, tools will play an increasingly important role in the future.

For example, recent studies indicate that interactions with and acoustic reflections from adjacent blade rows can have a significant impact on aerodynamic damping and excitation (see Schoenenborn & Ashcroft, 2014; Sanders *et al.*, 2019; Vahdati *et al.*, 2019). Such interactions are not regarded in classical, linear computations, which feature only single blade rows and one-way coupling of perturbations via so called gust boundary conditions for excitation calculations (see Frey *et al.*, 2013).

Moreover, there are examples highlighting the limitations of rudimentary turbulence and transition modelling in time-linearized computations based on the so-called frozen eddy viscosity approximation. This method takes the eddy viscosity field from a preceding steady-state computation and regards it as time-invariant. Heners *et al.* (2019) show that the inclusion of unsteady turbulence and transition effects can have a non-negligible impact on the aerodynamic excitation of an LPT blade caused by the wake of a TMTF. A flutter analysis of a transonic HPC vane with local shock-induced separation

reveals large discrepancies between linear calculations with the frozen eddy viscosity simplification and nonlinear calculations with unsteady turbulence modelling (Heners *et al.*, 2022).

Other recent research topics in aeroelasticity requiring nonlinear analysis tools deal with e.g. flutter-tolerant designs allowing small limit cycle oscillations (see e.g. Berthold *et al.*, 2022) and aerodynamic forcing predictions for fans in innovative engine integration concepts with boundary layer ingestion (e.g. Mårtensson, 2021).

Furthermore, unsteady simulations become increasingly important for aerodynamic performance analysis due to the general design trends mentioned above. But also research topics like non-axisymmetric casing treatments (e.g. Goinis *et al.*, 2021) or aerodynamic assessment and design of new engine integration concepts with boundary layer ingestion (e.g. Mennicken *et al.*, 2022) depend on unsteady flow analysis. Better prediction of film cooling with respect to unsteady effects (see e.g. Brind & Pullan, 2020) or unsteady rim seal purge flow interactions with endwall boundary layers (see e.g. Chilla *et al.*, 2013; Schuepbach *et al.*, 2010) can potentially yield thermal and aerodynamic efficiency gains.

This list is far from exhaustive, but exemplifies the contribution that nonlinear, unsteady flow simulations can make to future developments of turbomachinery engineering.

For turbomachinery flows, which are characterized by periodically unsteady effects, nonlinear frequency domain methods like the nonlinear harmonic (see e.g. He & Ning, 1998) or the harmonic balance (HB) method (see e.g. Hall *et al.*, 2002; McMullen, 2003; Frey *et al.*, 2014, 2015; Crespo *et al.*, 2015) have emerged as highly efficient tools compared to conventional time marching simulations. These approaches solve the Fourier-transformed URANS equations for distinct frequencies of interest, usually blade interaction frequencies or structural eigenfrequencies and higher harmonics thereof.

To date, methods like harmonic balance are not only popular in academia, but they are on the verge of being routinely employed in industrial design tasks. However, there are still some well-known issues, ongoing developments and intrinsic limitations of such methods. Firstly, the high level of robustness and stability, we are used to from time marching methods, is not (yet) reached by HB methods (see e.g. Huang & Ekici, 2014; Heners *et al.*, 2022). Furthermore, state of the art turbulence and transition modelling is an ongoing research topic with respect to model adjustments, validation and robustness (e.g. Ashcroft *et al.*, 2018; Kügeler *et al.*, 2018; Müller *et al.*, 2022; Heners, 2022).

Depending on the goal of a study or design task, the setup of HB computations often requires a deeper understanding of the method and the expected unsteady phenomena in comparison to more costly time domain simulations. While for the latter only the temporal discretization has to be chosen appropriately, the HB user has to define every interaction mode to be considered not only in terms of base frequency and number of higher harmonics thereof, but also with respect to circumferential periodicity and relative rotational direction. These specifications can, of course, be standardized and automated to a certain extent, e.g. by taking a specific number of direct interaction modes with adjacent blade rows into account. Yet, in multistage turbomachinery components, indexing effects and acoustic scatter can lead to very complex unsteady flow fields (Junge *et al.*, 2015; Frey *et al.*, 2018). Thus, capturing all relevant effects is not a trivial task, but can have a significant impact, e.g. on flutter and forced response of embedded blade rows (see e.g. Vahdati *et al.*, 2005; Gallardo *et al.*, 2019; Terstegen

et al., 2019).

Beyond the question as to which interaction modes have to be taken into account, there is no universal rule how many higher harmonics of those fundamental modes need to be considered in order to achieve a required level of accuracy (see e.g. Frey *et al.*, 2015; Schlüß & Frey, 2018; Ashcroft *et al.*, 2018). Furthermore, the well-established harmonic balance variant based on a so-called harmonic set approach neglects cross-coupling terms between individual harmonic sets while more recent approaches overcome this simplification, albeit at higher computational costs (see Junge *et al.*, 2018, 2021).

Further development of the harmonic balance technique is needed and currently addressed regarding extended applicability to more complex geometry features, such as non-axisymmetric casing treatments, seals and cavities. Moreover, frequency domain methods are only applicable if all fluctuations are strictly periodic and all relevant frequencies are known. Thus, phenomena like shock boundary layer interaction, unsteady wakes, vortex shedding or NSV pose additional challenges to frequency domain methods.

On the other hand, scale-resolving methods may progressively fill a niche between wind tunnel and rig testing on the one side and (U)RANS-based CFD on the other, in particular augmenting turbulence modelling and other more basic fluid dynamic-driven topics. However, scale-resolving simulations are still too expensive and time-consuming to replace (U)RANS-based CFD for most turbomachinery research and design tasks. Especially, their computational effort does not seem justified for those tasks where turbulence modelling is not deemed to be the primary source of errors or uncertainties.

Therefore, nonlinear, time domain (U)RANS simulations constitute the highest, feasible level of modelling unsteady flow phenomena in turbomachinery. Although nonlinear frequency domain methods are becoming more and more important due to their efficiency advantage over time domain methods, the latter will still play an important role for all the reasons mentioned above.

Due to ongoing progress in the development of hardware resources and software tools, time domain simulations have become more affordable and sufficiently fast not only for research purposes, but also for some tasks in everyday industrial design. Additionally, time domain computations play a key role for further development, validation and qualification of frequency domain tools by providing accurate, detailed and specifically tailored reference data. In the long run, if or when nonlinear frequency domain methods are considered state-of-the-art tools for the analysis of unsteady turbomachinery flows, time domain methods can be a valuable asset to complement frequency domain methods wherever the accuracy of the latter is at question, e.g. due to lack of exact knowledge about spectral content or periodicity of a flow.

1.1.3   Non-reflecting boundary conditions

However, numerical reflections arising from artificial, open boundaries at finite computational domains can strongly deteriorate the accuracy of flow solutions and especially the prediction of unsteady pressure fluctuations, which is in particular detrimental to applications in aeroelasticity. Besides computational costs, another advantage of frequency domain methods is that, in the frequency domain, the boundary flow field can be decomposed into waves with known direction of propagation. This allows for the implementation of accurate, spectral non-reflecting boundary conditions (NRBC)

in a relatively straightforward manner (see e.g. Hall & Crawley, 1989; Montgomery & Verdon, 1997; Moinier *et al.*, 2007; Petrie-Repar, 2010; Kersken *et al.*, 2014, and Section 2.3)). The term *spectral* indicates that these boundary conditions use fundamental wave propagation considerations based on spectral properties, i.e. wavenumbers and frequencies.[1]

For time domain simulations, the implementation of such boundary conditions is therefore more involved. Consequently, time domain methods often rely on time-local boundary conditions, which work well in some situations, but must be regarded as generally less accurate because they are prone to producing spurious reflections (see Section 2.2). Higher-order approximate NRBC are local in time and offer improved reflection properties compared to state-of-the-art NRBC in time domain simulations (see Section 2.2.3). Yet, they cannot be applied together with phase-shifted periodic boundary conditions, which poses a severe limitation for aeroelasticity applications.

This works aims at contributing to an accuracy improvement of time domain simulations by integration of spectral non-reflecting boundary conditions. These are well-established in the context of frequency domain methods and known for their excellent accuracy.

Moreover, these NRBC offer the benefit of being consistent with popular steady NRBC when applied in steady-state computations as well as with their frequency domain counterparts when applied in unsteady computations. The first aspect is important when comparing results from steady-state simulations with unsteady results in order to assess unsteady effects (rather than possible differences due to inconsistent boundary conditions). The latter is considered helpful because it makes very close comparisons between results from frequency domain and time domain computations possible. Having one CFD solver offering consistent implementations of turbulence models, numerical methods (except for time discretization), postprocessing routines and finally boundary conditions, greatly facilitates true comparability, which in turn is important since frequency domain and time domain methods are intended to complement each other as a cost effective alternative or a high-fidelity backup and validation tool, respectively.

1.2 Objective and outline

The objective of the present thesis is to develop an implementation of two-dimensional, spectral non-reflecting boundary conditions, adapted to time domain simulations with dual time-stepping, into DLR's turbomachinery CFD solver TRACE.

The term *two-dimensional* refers to the fact that the underlying theory is based on two-dimensional flow equations, but does not preclude the application of these boundary conditions to three-dimensional flow simulations using a quasi-three-dimensional approach. It should be noted, however, that viable, three-dimensional methods are subject to similar, simplifying assumptions (see Section 2.3) and, therefore, the expected accuracy advantage is limited while increased complexity and numerical effort might significantly impair their usability in time domain simulations.

Furthermore, the theory is derived based on linear hyperbolic systems of PDE. The

---

[1] In the literature, such boundary conditions are often referred to as *exact* because, when they were introduced, two-dimensional, linearized Euler methods were widely used and only for such methods these NRBC are indeed exact. Therefore, the term *spectral* is usually preferred in this work apart from passages where referenced literature uses the term *exact*.

NRBC can still be applied to nonlinear flow calculations, accepting a potential loss of accuracy due to the linearization error. As there is no equivalent theory for nonlinear flows in two or three dimensions, this error is inevitable.

Further conceptual decisions appear too technical for this section. Such decisions, their implications as well as conceptual limitations are, therefore, thoroughly discussed in Chapters 2 and 3.

Academic test cases of simplified complexity are studied in order to assess the reduction of spurious reflections in comparison to existing methods. The application to two realistic turbomachinery test cases confirms the improved accuracy and additionally underlines the maturity of the presented implementation for applications in real-world research and design scenarios. Numerical and experimental reference results are presented where available.

As the boundary condition is non-local in time and space, the challenge is to devise an implementation that offers not only the intended reduction of spurious reflections, but also the required stability and convergence characteristics for realistic applications beyond basic test cases. In particular, the dependence on a temporally spectral representation of the transient flow field needs to be addressed.

The scope of this work is limited to artificial or open inflow and outflow boundaries for flows which are subsonic in boundary-normal direction, like they are typically found in turbomachinery. Note that Mach numbers greater than one are still permitted in case of non-vanishing pitch-wise velocity components in the respective frame of reference. Supersonic boundary conditions are, firstly, deemed unproblematic and, secondly, of lesser relevance. Furthermore, the boundary conditions presented in this work are intended to be used in Euler- or (U)RANS-based simulations of turbomachinery flows since they rely on certain prerequisites that do not hold true for scale resolving simulations.

The structure of this work is as follows:

Chapter 2 reviews the existing literature and provides an overview of different approaches in the context of non-reflecting boundary conditions. After a brief introduction to the central mathematical concept, two different strategies are discerned. One group of boundary conditions seeks to formulate local, approximate and, hence, relatively simple, but also more universal boundary conditions. Such boundary conditions are considered state of the art for the vast majority of conventional time marching simulations. On the other hand, frequency domain methods often employ more accurate boundary conditions which incorporate a representation reflection of the original mathematical concept.

In **Chapter 3**, theory and implementation of the NRBC presented in this work are discussed. Firstly, those aspects of the underlying time domain flow solver are outlined, which are relevant for a successful implementation. Subsequently, the theoretical background of the spectral NRBC is discussed in detail, including explanations regarding their relationship to the popular set of boundary conditions proposed by Giles (1988). Finally, their implementation into a time marching solver is presented with particular emphasis on aspects that require additional considerations compared to frequency domain implementations.

Chapter 4 deals with three basic validation test cases. The flow in a transonic turbine cascade poses a challenge for existing, approximate boundary conditions due to the interaction of a suction-sided shock with the outlet boundary. For a single acoustic mode in a thin, annular duct, the reflection coefficient is evaluated and compared to existing

boundary conditions in TRACE. The flutter analysis of a two-dimensional compressor cascade (tenth standard configuration) demonstrates how reduced numerical reflections improve the prediction of aerodynamic damping.

In **Chapter 5**, the NRBC is applied to two realistic turbomachinery configurations. Firstly, we consider flutter of a transonic steam turbine blade with the spectral NRBC and a one-dimensional, characteristic NRBC and two computational domains. Secondly, the unsteady blade row interaction in a modern, highly loaded compressor is studied. The correct prediction of unsteady blade pressure distributions is critical for forced response analysis, although no aeroelastic postprocessing is presented here. An analysis with focus on the impact of numerical reflections at inlet and outlet boundaries is shown for both test cases.

Finally, **Chapter 6** summarizes the thesis and offers an outlook on possible future developments.

2 State of the art

2.1 Well-posedness of multi-dimensional, hyperbolic systems

Before the subsequent sections will outline various approaches available in the literature to formulate (non-reflecting) boundary conditions, it appears worthwhile to discuss some basic concepts in the context of partial differential equations (PDE) in this section. The formulation of boundary conditions for systems of PDE is closely linked to the question whether the resulting mathematical problem is well-posed, i.e. whether there is a unique and bounded solution to the problem. The question of well-posedness, however, depends on fundamental properties of the system of PDE.

The time-dependent Navier-Stokes and URANS equations are characterized as mixed parabolic-hyperbolic systems, where the parabolic nature of the system is associated with diffusive effects through heat conductivity and viscosity, while the hyperbolic nature is associated with advection phenomena. Aside from very low Reynolds number flows (which are of no concern in engineering aerodynamics) and from boundary layers in the very vicinity of solid walls, it is reasonable to assume that the impact of diffusion is small. Thus, the Navier-Stokes and URANS equations are often regarded as essentially hyperbolic and they are numerically solved using methods that have originally been developed for the actually hyperbolic Euler equations with extensions for diffusive phenomena where needed (cf. e.g. Toro, 1999).

The steady-state equations can be elliptic, parabolic or hyperbolic depending on local flow conditions, which implies different requirements for numerical methods. Therefore, the steady-state equations are often solved using a pseudo-time approach, which restores the (parabolic-)hyperbolic character of the system and thereby allows the application of the same spatial discretization methods as for the time-dependent problem (see Hirsch, 2007).

For the development of open, artificial boundaries, it is assumed that the parabolic portion of the system is negligible in the vicinity of such boundaries and, therefore, well-established theories for hyperbolic systems apply. For multi-dimensional, hyperbolic systems of PDE, Kreiss (1970) and Majda & Osher (1975) have devised theoretical considerations, that are deemed a cornerstone in the development of boundary conditions today. "The theory is extremely complicated and algebraic; its physical meaning tends to get buried by lengthy and detailed studies of various matrices" as Higdon (1986*b*) puts it in his paper. Higdon provides a physical and geometrical interpretation of the above mentioned works and applies the theory, for example, to Maxwell's equations, to the shallow water equations or to the linearized, isentropic Euler equations. Therefore, this work is often mentioned along with the original works when the topic is approached by researchers from applied mathematics, physics and engineering.

9

To analyse if a system is well-posed, one often invokes energy estimates, i.e. one shows that the (physical) energy within the system at hand remains bounded. Higdon stresses, that such energy arguments are sufficient to prove well-posedness, but not necessary. That means such a proof can fail even though the problem is indeed well-posed. The theory by Kreiss (1970) and Majda & Osher (1975) provides a sufficient and necessary condition based on a so-called normal mode analysis. The argument is derived for linear systems. Hence, it is also applicable to linearized versions of nonlinear problems (cf. Higdon, 1986*b*).

The key aspect of this theory is that, in order to obtain well-posed initial boundary value problems (IBVP), one needs to formulate boundary conditions such that the propagation of information is correctly taken into account. More precisely, the direction of propagation needs to be determined somehow and information from inside must be able to leave the computational domain unhindered while incoming information must be specified by means of a boundary condition.

For one-dimensional problems, this distinction is usually simple and based on characteristic variables as covered by almost every introductory course or textbook on numerical methods for fluid dynamics (e.g. see again Hirsch, 2007; Toro, 1999). The characteristics represent wave-like portions of the solution with known propagation properties.

However, the identification of such wave-like parts of the solution may become complicated for two- and three-dimensional problems as these cannot be brought into a diagonal form by transformation into characteristic variables. Here, the normal mode analysis can be carried out by means of ansatz functions in the form of plane wave solutions (see Section 3.2). This approach requires the spectral properties of the waves, i.e. frequencies and wavenumbers, to be known. Hence, the exact normal mode analysis is no longer local in space and time, instead it requires a spectral representation of the solution. Boundary conditions based on the exact normal mode analysis are, therefore, also non-local in space and time, which complicates their implementation in numerical solvers.

In the following, we distinguish two groups of strategies for the formulation of boundary conditions: The first group circumvents the non-local nature of the normal mode analysis by either requiring further, simplifying assumptions or introducing local approximations with various levels of accuracy and complexity. Section 2.2 provides an overview of these methods without any claim of being comprehensive; it is rather supposed to summarize the most important contributions from a turbomachinery aerodynamics perspective. For a more general overview, the interested reader is referred to a review article by Givoli (1991). It contains developments and examples from different disciplines of physics, e.g fluid dynamics, hydrodynamics, electromagnetics, seismology, meteorology and acoustics.

Givoli concludes his work with a comment that local NRBCs often perform well under certain conditions, but quite poorly in other situations. He considers non-local, exact formulations to be more promising if they can be realized such that the numerical solution of the IBVP can be computed efficiently. Therefore, Section 2.3 will deal with the application of exact boundary conditions to turbomachinery flows.

2.2 Concepts of approximate non-reflecting boundary conditions

2.2.1 Very basic boundary conditions

Simple types of artificial boundary conditions were used before the closely related well-posedness theory by Kreiss and others was established. Some of them are still in use today, but they are generally not well suited for internal flows, in particular not for unsteady problems.

If the solution can be expected to correspond to radiation of simple waves, Sommerfeld-type radiation conditions can be applied at open boundaries in the far-field (see Givoli, 1991). However, this approach requires knowledge of the sought solution at infinity and can lead to large errors if the assumed solution at infinity does not properly match the actual solution at the far-field boundary. For internal flows, two main problems arise: Firstly, due to geometrical constraints, it is often not possible to extend the computational domain such that the boundary flow field could adequately be considered as a far-field. Secondly, the solution is often more complex and cannot be described by a simple radiation pattern. Even if an analytical far-field solution exists, it is usually much more difficult to find it a-priori.

Therefore, one often finds simple, mixed boundary conditions, where some components of the boundary flow state vector are prescribed at the boundary while others are extrapolated from the inside. The number of variables to be prescribed or extrapolated, respectively, is determined with considerations based on one-dimensional flows and characteristics. For two- and three-dimensional flows the rationale is carried over, i.e. the characteristics transformation is performed with respect to the boundary-normal direction. The well-known result is that e.g. for subsonic, three-dimensional flows, four variables have to be specified at an inflow and the remaining one needs to be extrapolated from inside and vice versa at outflow boundaries. For flows with supersonic boundary-normal speed, the complete flow state has to be described at the inflow and no variable is needed at the outflow.

The choice, which combinations of variables are prescribed and which ones are extrapolated in the subsonic case, is not unique and often made heuristically to some extend. Although numerical solvers can solve different representations of the conservation equations, i.e. in conservative or primitive variables and with various combinations of variables defining the thermodynamic state of the fluid, the admissible sets of specified variables remain the same and depend only on the flow state. A stringent well-posedness analysis was only presented later for some combinations (see Hirsch, 1990, and references therein). For many applications, the velocity vector and temperature are specified at inlets, while pressure is prescribed at outlets. In turbomachinery aerodynamics, it is more common to specify stagnation pressure and stagnation temperature together with the flow direction, most often in terms of the usual flow angle definitions, at inlets. As the specified boundary values are held fixed at any point in time and space, they inherently do not allow passing waves. Hence, this kind of boundary conditions are known to be highly reflective and therefore of very limited use in advanced turbomachinery design tools, in particular when dealing with unsteady flows.

2.2.2 Characteristics-based approaches

The probably most widely used class of non-reflecting boundary conditions for time domain flow solvers, in particular for general purpose CFD tools, are those which utilize the diagonalizability of the one-dimensional Euler equations and the resulting variable transformation to so-called characteristic variables.

For two- and three-dimensional flows, it is impossible to diagonalize the flux Jacobians associated with each spatial dimension simultaneously. However, one can define a characteristic variable transformation with respect to a given direction analogously to the one-dimensional case. As a result, the characteristic variables will in general not entirely decouple except for special cases (see Hirsch, 1990).

They should not be confused with the modes in the sense of Kreiss's normal mode analysis, which are independent of each other (under the linearization assumption). All approaches based on characteristics can be understood as a first-order approximation to the non-local normal mode analysis of Kreiss, although not all of the methods presented in this section are explicitly derived as an approximation to the normal mode analysis.

Hedstrom (1979) is credited with being the first researcher to formulate non-reflecting boundary conditions for the Euler equations based on characteristic variables. He considers the one-dimensional, nonlinear Euler equations and in this case the diagonalization of the quasi-linear form does in fact not even require linearization. The nonlinear counterparts to the characteristic variables are called Riemann invariants.

A variant of a boundary condition using Riemann invariants in the boundary-normal direction for three-dimensional flows is described by Blazek (2001). It is implemented in TRACE as a steady boundary condition and will be employed in Section 4.1.

The work of Higdon (1986*a*) is seen as a further important step towards non-reflecting boundary conditions for multi-dimensional hyperbolic systems. He enhances the one-dimensional approach for the scalar wave equation to arbitrary directions. By that, he found a boundary condition which is able to perfectly absorb waves which hit the boundary non-perpendicularly. The drawback of his method is that the incidence angles for perfect absorption need to be defined beforehand. But the boundary condition is able to consider multiple expected incidence angles and Higdon shows that his method provides good reflection properties with a limited number of specified incidence angles.

Thompson (1987) expands Hedstrom's approach to two-dimensional and later to three-dimensional Euler equations (Thompson, 1990). He applies the characteristics transformation in boundary-normal direction and, as mentioned above, the boundary condition is no longer exactly non-reflecting since derivatives in boundary-parallel direction lead to source or coupling terms in the transport equations of the characteristics. Colonius (2004) reviews various, approximate non-reflecting boundary conditions and demonstrates that Thompson's boundary conditions yields lower reflection coefficients than Hedstrom's (one-dimensional) boundary condition for oblique acoustic waves at outflows, but produces stronger reflections for outgoing vorticity waves and for acoustic upstream waves at inflows.

Chernysheva (2004) presents a similar approach which does not necessarily perform the characteristics transformation with respect to the boundary normal direction. Instead, she chooses the reference direction with respect to local flow conditions and pressure gradients and introduces some additional considerations to minimize the cou-

pling terms. Only under certain conditions, the coupling terms vanish entirely, e.g. when the flow is uniform or one-dimensional (i.e. all gradients perpendicular to the mean flow direction vanish when solving the two- or three-dimensional Euler equations). Chernysheva demonstrates that this approach is capable of dealing with single, large amplitude acoustic waves and weak shocks with moderate angle of incidence in uniform background flow, exhibiting greatly improved reflection properties compared to boundary-normal characteristic boundary formulations. Yet, no further application of this boundary condition to more complex flows or waves with shallower incident angles has been published to the best knowledge of the author of this thesis.

A boundary condition that has received a lot of attention, in especially from LES and DNS communities, is an evolution of Thompson's method proposed by Poinsot & Lele (1992). This method offers two essential improvements that benefit in particular applications in LES and DNS. Firstly, the method takes viscosity and thermal conductivity into account, which appears more important in scale resolving simulations than in (U)RANS methods since the parabolic nature of the Navier-Stokes equations is more pronounced on small scales. Secondly, it does not rely on simple extrapolation of outgoing characteristics, but rather casts flow equations in a mixed form, which regards all derivatives in boundary-normal direction in terms of characteristic variables while retaining all boundary-parallel derivatives in conservative variables. Thus, one can properly integrate the temporal evolution of the boundary flow field using higher-order discretization schemes with appropriate one-sided stencils for the outgoing characteristic variables. To determine the incoming characteristics on the boundary surface, the authors describe a variety of recipes to translate user-defined boundary values, such as inflow velocity or stagnation quantities or outflow pressure, into values for the incoming characteristics. However, the boundary condition is still only approximately non-reflecting since the calculation of incoming characteristics is subject to approximations, viz. diffusion terms and cross-derivatives are disregarded. Hence, the authors state that this boundary condition is well suited for one-dimensional flows or flows with small transverse gradients.

Poinsot & Lele (1992) also discuss one problem that all temporally and spatially local boundary conditions inherently have in common (unless linear flow equations with constant mean state are considered): When, for example, one wants to prescribe a static pressure at an outflow, it is impossible to enforce this pressure at all time instances and simultaneously allow acoustic waves to pass the boundary without reflection because the acoustic wave will obviously induce a pressure perturbation. A local boundary condition offers the mathematical tool to pursue either of the following two, opposing strategies. On the one hand, the pressure can be kept constant by imposing an equally strong incoming acoustic wave or, on the other hand, one can let the wave pass freely and never impose an incoming wave. In the latter case, however, there is no mechanism to make sure that the originally specified pressure will ever be reached, indicating an ill-posed problem. Therefore, relaxed incoming waves, i.e. some reflections, are usually imposed to prevent the boundary value from drifting away. The ideal amount of relaxation is a matter of tuning and depends on the application and on individual requirements regarding reflection properties, although there are popular proposals regarding an optimal relaxation parameter (e.g. Rudy & Strikwerda, 1980).

From this perspective, it appears advantageous to replace the local boundary condition by a condition based on averaged and, thus, non-local boundary states. Giles (1988) suggests such an approach for URANS simulations of turbomachinery flows (see also Giles, 1990, 1991, and Section 3.3.1). Here, one can exploit the associated periodicity

of the flow and easily define a suitable, spatial and/or temporal mean state. Then, an incoming mean characteristic can be specified with respect to the deviation of that mean state from user-defined target values, which will be exactly zero once the mean-state is converged at the target values, and, thus, the incoming mean characteristic will vanish as well. The condition to suppress reflections at the boundary is then simply that the local portion of the incoming characteristic is always zero. This boundary condition is technically non-local due to the averaging process involved, but still very simple to implement. In Giles' paper, he refers to this boundary condition as unsteady, one-dimensional NRBC.

It should be noted that for non-periodic flows, such as LES or DNS, it is not trivial to define a mean state that converges entirely unless the averaging is performed over very large periods of time, which then causes a considerable lag in the development of temporal averages and, therefore, leads to very slow convergence.

2.2.3   Higher-order approximate boundary conditions

A pioneering work for the development of numerous higher-order approximate non-reflecting boundary conditions has been achieved by Engquist & Majda (1977). As mentioned in Section 2.1, the exact condition to discern incoming and outgoing waves is non-local in space and time since it is expressed as a function of frequency and wavenumber components. The idea of Engquist and Majda is to replace this function with a local approximation using either a Taylor polynomial or a Padé approximant (a similar approximation technique using a rational function instead of a polynomial) around the one-dimensional case, i.e. waves crossing the boundary surface perpendicularly. Using this approximation, they develop a sequence of local boundary conditions for wave equations with increasing order of accuracy and present an application to the linearized shallow water equations. They show that the use of Taylor polynomials of higher than second order will produce ill-posed IBVP while higher-order boundary conditions can be obtained with higher-order Padé approximants. As mentioned in the previous section, boundary conditions based on characteristics correspond to the class of first-order boundary conditions in the terms of Engquist and Majda's approach.

Following their work, Giles (1990) presents variants of Enquist and Majda's method for the two-dimensional Euler equations and especially for turbomachinery flows. See also Giles (1988) for more theoretical background and Giles (1991) for a description of implementation details. These boundary conditions have gained huge popularity in the turbomachinery community. The one-dimensional or first-order unsteady boundary condition has already been mentioned in the previous section.

Moreover, a second-order variant is presented. It is referred to as approximate, two-dimensional boundary condition because the higher-order term of the Taylor polynomial leads to a boundary-parallel derivative in the final equation (see also Section 3.3.2 and for details about its implementation in TRACE Ashcroft & Schulz (2004)). Giles proves that the second-order inflow boundary condition is ill-posed in its original formulation, but well-posed in a modified version (see Giles, 1988). The two-dimensional boundary condition generally exhibits significantly improved reflection properties over the first-order boundary condition (see Sections 4.2 and 4.3). However, for low frequency perturbations or waves with shallow incidence angles, especially towards acoustic resonance, the two-dimensional boundary conditions becomes reflective too.

An exact, unsteady variant for single-frequency flows will be discussed in Section 2.3. A special case of this single frequency boundary condition is the steady boundary condition, which is obtained straightforwardly in the zero frequency limit (see Section 3.3.3). This boundary condition requires a Fourier transformation of the boundary flow field in circumferential direction because it uses the exact mode decomposition matrix. Although it is hence not an approximate boundary condition, it is listed here as it clearly belongs to the group of Giles's boundary conditions and it represents a crucial stepping stone in the development of turbomachinery boundary conditions, including those that follow in the remainder of this section.

Saxer & Giles (1993) extend the exact steady, exact, two-dimensional boundary conditions to three-dimensional flows using a quasi-three-dimensional procedure, i.e. the two-dimensional approach is applied in blade-to-blade stream surfaces of constant radius assuming the flow varies sufficiently slowly in radial direction. The boundary condition is, hence, radially decoupled apart from the fact that the flow in each plane is linearized about its respective mean flow at the respective radial position. Other two-dimensional boundary conditions can be applied to three-dimensional flows accordingly and also the two-dimensional boundary condition presented in this work follows this technique (see Chapter 3).

Fan & Lakshminarayana (1996) employ the boundary-parallel derivative, that arises in Giles's second-order, two-dimensional boundary condition, also in spanwise direction of three-dimensional flows. This yields a second-order, three-dimensional boundary condition. It should be note, however, that they assume the underlying wave ansatz in terms of Fourier modes is also valid in three-dimensional flows which is not true in turbomachinery flows as there is no periodicity in spanwise direction.

With the exception of Giles's exact steady boundary conditions, all aforementioned boundary conditions for fluid dynamics applications are of second or lower order accuracy (in terms of different expressions describing deviations from boundary-normal waves, e.g. circumferential wavenumber or angle of incidence). Bayliss & Turkel (1982) present a first, higher-order approximate boundary condition with applications to flow problems, yet not following Engquist and Majda's approach, but as a higher-order farfield (or radiation) boundary condition. Hence, the asymptotic expansion is not around normal incidence angles but around an analytical solution at infinity, i.e. in terms of the reciprocal boundary distance. Bayliss and Turkel report one fundamental difficulty for the development of higher-order approximate boundary conditions that also arises when one wants to incorporate higher-order terms in Engquist and Majda's method: higher-order terms occur (by inverse Fourier transformation) as higher-order differential operators in the local, approximate boundary conditions, which poses a challenge for their efficient and robust implementation (see e.g. Givoli, 2004).

Collino (1993) suggests replacing these higher-order derivatives with auxiliary variables, for which additional first-order evolution equations must be solved in the boundary surface. This concept is used by Hagstrom (1997) to present boundary conditions of higher-order NRBC based on Engquist and Majda's Padé approach for the isentropic, compressible Euler equations. It is shown that the boundary condition is well-posed for arbitrarily high orders of accuracy. The first implementation and numerical experiments are presented by Goodrich & Hagstrom (1996).

However, the time- and space-local boundary conditions accumulate numerical errors over time such that under some conditions they are theoretically not stable over long integration times. Hagstrom & Goodrich (2003) show that using very high orders of accuracy for simulations over long periods of time can mitigate the error. An im-

proved method is presented by Alpert *et al.* (2002) for the wave equation and later adopted by Henninger *et al.* (2015) and Henninger (2019) as extension of Giles's approximate, unsteady boundary condition with up to 33rd order accuracy in TRACE. This approach remedies the long term integration error at the cost of becoming non-local in space. This means similarly to Giles's exact, steady boundary condition, a circumferential Fourier transformation of the boundary flow field is needed. Unlike the spectral boundary condition presented in this work, Henninger's boundary condition is not compatible with phase-shifted periodic boundaries, as they are often used in turbomachinery applications. This limits their efficient applicability, in particular for aeroelastic analysis of flutter or conventional forced response problems (based on two-row configurations without neighbouring rows).

Rowley & Colonius (2000) introduce a sequence of boundary conditions, which is similar to the group of local, higher-order Hagstrom-type boundary conditions, but they incorporate a correction for the artificial dispersion of the respective numerical scheme in the dispersion relation, which is otherwise usually obtained from the continuous PDE and is the starting point of the eigenvector problem to discern incoming and outgoing waves. Therefore, they refer to their method as discretely non-reflecting boundary condition.

Beyond the scope of (turbomachinery) aerodynamics, the interested reader is referred to a review article by Givoli (2004) to learn more about higher-order approximate boundary conditions in other domains of physics. In that article, the author designates all boundary conditions as exact which converge to the exact pseudo-differential operator of the normal mode analysis with increasing approximation order. This should not be confused with exact, non-local boundary conditions, which are addressed in Section 2.3 and presented in this work for time domain simulations.

2.2.4 Buffer layers

This section deals with a group of techniques which are technically no boundary conditions, but often developed or applied in this context. Hence, they should at least be outlined in brevity here. There is no unique term for such tools, they are usually called buffer layers, sponge layers, absorbing zones or something similar. They are usually employed in combination with a mathematical boundary condition in order to mitigate errors that arise when suitable non-reflecting boundary conditions are not available, not only in CFD applications, but also in other numerical methods solving wave propagation problems.

The basic idea is to add a layer of the computational grid next to the boundary surface, in which outgoing waves, that might induce reflections at an artificial boundary, as well as reflected perturbations are damped as much as possible. Thus, spurious reflections have no impact on the actual flow field outside of this layer.

A good overview of such techniques is provided by Colonius & Lele (2004) with focus on aeroacoustics and Colonius (2004) with emphasis on shear flows and turbulence resolving simulations. Besides different kinds of buffer layers, the articles also address (actual) boundary conditions for such flows and the particular challenges involved, e.g. non-uniform base flows, nonlinearity of the flow, and implications for higher-order discretization schemes.

The most basic technique, which does not even require code modifications and can be done on user level during the meshing process, is grid stretching in the far-field

towards the artificial boundary. This adds numerical dissipation up to the point that small scale perturbations can no longer be resolved and are effectively filtered. Often such grid inflation is supplemented by adding artificial viscosity, using dissipative, biased discretization stencils or central schemes with additional low pass filtering (see e.g. Rai & Moin, 1993; Colonius *et al.*, 1993).

More sophisticated techniques modify the underlying equations within the buffer layer by adding artificial convection, often in combination with artificial damping. Ta'asan & Nark (1995) introduce an artificial convection term which causes supersonic conditions in the buffer zone, thereby preventing reflected waves at outflow boundaries from re-entering the region of interest. At inflow boundaries, outgoing waves cannot reach the boundary plane and, thus, no artificial reflection is generated. The opposite strategy is suggested by Karni (1996), who decelerates waves by an artificial convection term such that they remain within the buffer zone as long as possible (ideally forever) where they are damped by artificial and/or numerical damping.

All of these methods suffer from one common difficulty, i.e. they modify the dispersion properties of the continuous or discrete system, either as a by-product of inducing dissipation or intentionally as in the latter methods. Since changes of dispersion properties in a medium always produce (partial) reflection of waves, these interventions have to be introduced gradually within the buffer zone, yielding rather big additional domains if a small level of reflection is needed. Colonius (2004) highlights that such methods are, therefore, usually not perfectly non-reflecting and the achievable damping is scale-dependent. Hence, a considerable amount of heuristic tuning to specific applications and flow conditions and some experience with that is required.

A more recent paper by Mueller *et al.* (2021) investigates the use of such methods for turbomachinery flutter calculations with commercial CFD tools which do not feature effective non-reflecting boundary conditions. The authors show considerably improved accuracy of the flutter prediction when adding rather large, additional inlet and outlet buffer zones. However, this also has a moderate effect on the mean flow and may be difficult to apply to geometrically more complex real-world turbomachinery configurations or even multi-row setups due to the necessary extent of the buffer zones.

A systematic approach to impose the above mentioned local modifications in an optimized way is the so-called Perfectly Matched Layer (PML), first introduced by Berenger (1994) for electromagnetic waves. Hu (1996) and Abarbanel *et al.* (1999) showcase the first PML for the linearized Euler equations with applications to flows with uniform mean flow. In the PML, a coordinate transformation is performed such that the dispersion relation is conserved locally. For this purpose, a plane wave ansatz is considered, very much like for the development of non-reflecting boundary conditions, yielding a set of inhomogeneous PDE with source terms as functions of spectral parameters, i.e. frequencies and wavenumbers. These source terms are then replaced by auxiliary variables with the aim of providing ideal, non-physical damping independently of the spectral parameters. As a result, additional ODE are obtained for those auxiliary variables, which have to be solved along with the transformed, original equations.

Initial stability issues have been addressed by Bécache *et al.* (2003) and extensions to the linearized Euler equations with inhomogeneous background flow (Hu, 2005) and to the nonlinear Navier-Stokes equations (Hagstrom *et al.*, 2005) were developed subsequently. Yet, for nonlinear systems, the PML is not perfectly non-reflecting, but produces second-order errors (cf. Colonius, 2004).

2.3 Spectral non-reflecting boundary conditions

2.3.1 Frequency domain applications

There are two main causes that complicate or even inhibit the development of a universal, perfectly non-reflecting boundary condition. The first cause is that there is to date no nonlinear, multi-dimensional equivalent to the normal mode analysis outlined in Section 2.1. The second cause is that the existing theory is inherently non-local in time and space. While only some of the methods presented in Section 2.2 adress the nonlinearity issue, all of them, explicitly or implicitly, aim at resolving the difficulty of formulating a non-local boundary condition by introducing approximations that allow a local formulation (the only exceptions being Giles's exact, steady boundary condition for the reason mentioned earlier and Hedstrom's boundary condition when used in its original form for one-dimensional problems only).

For time domain, i.e. time marching, methods, the dilemma is primarily rooted in the temporally non-local nature of the existing mode analysis because the complete temporal history of the solution cannot be known until the simulation is terminated, not to mention the memory that would be required if this were possible. The spatial non-local nature, on the other hand, creates a certain amount of complexity compared to local methods and, thus, requires additional effort for developing and implementing spatially non-local boundary conditions. Yet, it is possible to do so as the solution is usually known for the entire computational domain at a given point in time.

Therefore, it is much easier to define non-reflecting boundary conditions for frequency domain methods, which consider periodically unsteady problems in terms of a limited number of temporal Fourier harmonics as these represent the entire time history of a periodic problem. For two-dimensional potential flow in oscillating cascades, non-reflecting boundary conditions are first presented by Verdon *et al.* (1975), Verdon & Caspar (1980) and Whitehead (1982).

A first application with two-dimensional, linearized Euler equations is demonstrated by Hall (1987) and Hall & Crawley (1989). This boundary condition is exact for the linearized Euler equations if certain requirements regarding the underlying mean flow are met (see Section 3.2.1).

Hall's boundary condition corresponds to the exact, two-dimensional, single frequency boundary condition in Giles's papers (Giles, 1988, 1990). This boundary condition is consistent with Giles's popular exact, steady boundary condition as it converges towards the steady boundary condition for vanishing frequency, apart from some modifications of the steady boundary condition in its implementation into the UNSFLO code (see Giles, 1991, and Section 3.3.3).

Giles (1988) suggests that the exact, single frequency boundary conditions should be cast in terms of characteristic variables rather primitive variables when a pseudo-time stepping technique is employed. Since it is well-known that a hyperbolic system is well-posed with vanishing, incoming characteristics, he presumes without own testing that the pseudo-time system will remain stable if the incoming characteristics, determined as functions of the outgoing ones by means of the exact two-dimensional boundary condition, are sufficiently relaxed. Many of the methods presented below follow this suggestion when employing a pseudo-time solution method. The characteristics-based formulation is also used for the implementation into a time domain dual time-stepping solver presented in this thesis and the author considers this an essential step

towards the achieved stability.

The two-dimensional boundary conditions can be applied to three-dimensional flows with a quasi-three-dimensional approach corresponding to the concept of Saxer & Giles (1993) for steady boundary conditions. This allows an analytical solution of the eigenvalue problem for the mode decomposition. Alternatively, Hall *et al.* (1993) introduce a numerical approach for a three-dimensional mode decomposition. Like in the quasi-three-dimensional approach, the solution is expressed in terms of circumferential Fourier modes at each radial position. Thus, one can obtain an eigenvalue problem for each circumferential mode for which the radial distribution of the Fourier modes needs to be discretized. This eigenvalue problem can then be solved numerically.

Moinier & Giles (2005) enhance the three-dimensional mode decomposition by adding radial components of viscous stress and heat flux to the eigenvalue problem, targeting a better representation of the radially varying mean flow in the presence of sidewall boundary layers. This mode decomposition is employed in a three-dimensional, viscous NRBC proposed by Moinier *et al.* (2007). Viscous or inviscid variants of such boundary conditions are today commonly used in time-linearized solvers (e.g. Kersken *et al.*, 2014; Sotillo & Gallardo, 2018).

Note that all the above methods assume the mean flow to be axially and circumferentially uniform. Petrie-Repar (2010) shows a method allowing for non-uniform mean flow, which however leads to a two-dimensional, discrete eigenvalue problem for the mode decomposition (in contrast to one-dimensional in radial direction for the aforementioned methods). Consequently, Petrie-Repar reports that the numerical effort to solve the eigenvalue problem is in the same order of magnitude as the solution of the linearized flow equations for the internal flow, even when a much coarser auxiliary mesh is used for the boundary condition. Without this auxiliary mesh, the eigenvalue problem alone is much more expensive than the actual flow solution. Interpolation from and onto the coarse, auxiliary mesh could, however, introduce an error, which is not significant in Petrie-Repar's test case, but might give rise to limitations for the application to flows with stronger circumferential gradients, such as transonic flows or blade row interactions.

A complication for the implementation of exact, non-reflecting boundary conditions is the phenomenon of acoustic resonance at the cut-on/cut-off transition. In this situation, the axial group velocity of acoustic modes is zero, which causes upstream and downstream modes to coincide and form a single standing wave, which is not able to propagate axially, but spins circumferentially. Hence, the modal decomposition matrix becomes singular and is therefore useless for the definition of a modal boundary condition. This issue is addressed by Kersken *et al.* (2014) and later in more detail by Frey & Kersken (2016). They propose an approach which is outlined in Section 3.2.2.

The two-dimensional (i.e. quasi-three-dimensional) variant of the exact boundary condition is also successfully employed in nonlinear frequency domain methods, such as harmonic balance (e.g. Lindblad *et al.*, 2019; Ekici & Hall, 2007; Frey *et al.*, 2014). The spectral mode decomposition is then applied at each resolved frequency. A similar boundary condition for the application in a HB solver with Discontinuous Galerkin spatial discretization is presented by Wukie *et al.* (2019).

An interesting advantage over local boundary conditions is that the boundary condition can be used to readily model the blade row coupling interface when studying blade row interactions with HB (see Ekici & Hall, 2007; Frey *et al.*, 2014; Lindblad, 2020). If a mode is resolved in the adjacent blade row (with respect to the correct

frequency shift due to relative motion of the respective frames of reference), then the non-reflecting boundary condition, i.e. zero amplitude of incoming waves, is replaced by prescribing the amplitude associated with the incoming portion of the mode from the adjacent blade row. Otherwise, the mode is treated like at an inflow or outflow boundary with vanishing incoming amplitude.

The primary reason for sticking to the two-dimensional mode decomposition instead of using the fully three-dimensional method is that the underlying mean flow is not fixed in case of the harmonic balance method. This would necessitate a repeated, numerically expensive solution of the eigenvalue problem, which is a function of the mean flow only, while for time-linearized methods it suffices to solve the eigenvalue problem as a preprocessing step. Recall that the two-dimensional approach uses an analytical solution based on Fourier modes and is therefore much cheaper.

Frey *et al.* (2020) reason that the error introduced by using a two-dimensional mode decomposition is in the same order of magnitude as errors caused e.g. by violating the underlying assumptions of linearizability and uniform background flow or by disregarding physical reflections from the surroundings when using a truncated domain. Thus, considering the remaining error due to unavoidable simplifications, it does not appear worthwhile to accept the significantly increased computational effort required to employ the theoretically superior, three-dimensional mode analysis.

Studies of LPT flutter demonstrate that the difference between solution obtained with three-dimensional and quasi-three-dimensional boundary conditions is relatively small compared to either the differences one obtains using a one-dimensional boundary condition (see Kersken *et al.*, 2014) or compared to the impact of considering interactions with neighbouring blade rows (see Sotillo & Gallardo, 2018).

Implications of using the quasi-three-dimensional approach are discussed by Frey *et al.* (2020) in the first part of a double paper and numerical experiments are presented by Wolfrum *et al.* (2020) in the second part. This approach raises the question how to define the rotational surface for the two-dimensional mode decomposition in case of inclined boundary surfaces (i.e. axisymmetrical, but not perpendicular to machine axis) or radially converging or diverging mean flow (e.g. due to non-cylindrical endwalls). The authors show that characteristic variables should always be defined with respect to the boundary normal direction for stability reasons. However, the boundary condition may become more accurate in simplified test cases when the modal decomposition, to determine target incoming characteristics, is performed with respect to the mean meridional velocity vector rather than with respect to the boundary normal direction. Yet, counter-examples could be constructed and in a forced response calculation, characterized by strong secondary flow structures and a diverging annulus, typical of an LPT, the accuracy improvement could not be confirmed so clearly.

2.3.2 Time domain adaption of spectral NRBC

Due to the inherent intricacy of implementing a temporally and spatially non-local boundary condition for time marching simulations, there are, to the author's knowledge, only few efforts in the literature to apply boundary conditions, which are exact with respect to spectral modal decomposition of the linearized Euler equations, in time domain CFD of turbomachinery.

Chassaing & Gerolymos (2007) present a time domain implementation of an exact, spectral boundary condition similar to the two-dimensional frequency domain bound-

ary conditions discussed in the previous section. To perform the temporal Fourier transformation, they apply an iterative moving-average technique from their implementation of the phase-lag method (Gerolymos *et al.*, 2002). The authors demonstrate considerably improved accuracy, i.e. reduction of artificial reflections, compared to a one-dimensional and to Giles's approximate, two-dimensional NRBC for a single acoustic mode in uniform, inviscid, two-dimensional flow (very similar to the test case presented in Section 4.2). However, stability issues are reported unless the algorithm is restricted to considering only the one circumferential Fourier mode corresponding to the imposed acoustic mode.

Chernysheva (2004) presents a similar study with similar findings based on another implementation of the exact, two-dimensional NRBC. While showcasing superior reflection properties over approximate boundary conditions for small perturbation levels, the boundary condition fails at yielding converged solutions when the amplitude is increased beyond 3 % of the mean flow pressure. She also shows a successful application to flutter calculations of a flat plate cascade with a torsional vibration mode, exhibiting very good reflection properties and agreement with reference results. Unfortunately, there is only little information on implementation details. In particular, no description is given about the temporal Fourier transformation except that only one, fundamental harmonic is considered.

Both of the above boundary conditions are implemented in primitive variables, not in terms of characteristic variables. Recalling Giles's proposal about using characteristic variables and successful examples from frequency domain methods with pseudo-time solvers in the previous section, it appears quite possible that the limited robustness of the implementations by Chassaing & Gerolymos (2004) and Chernysheva (2004) is at least partly due to this choice of variables.

The author of this thesis along with colleagues at DLR's Institute of Propulsion Technology have experience with an ad-hoc adoption of our harmonic balance implementation of the exact, two-dimensional boundary condition. Applications in two-dimensional, steady-state, transonic turbine cascade flow and unsteady computations of a compressor stage (Schlüß *et al.*, 2016) as well as LPT flutter computations (Kersken *et al.*, 2014) showed promising results regarding accuracy. Yet, we have observed similar robustness issues in other cases, severely limiting the general applicability of our implementation. If convergence could be reached, it was usually significantly delayed compared to other boundary conditions.

For the reasons discussed in Chapter 1.1 and based on the desirable accuracy observed with the previous ad-hoc implementation mentioned above, it was decided to further pursue the development of a time domain-specific implementation of the spectral NRBC. The result is presented in this work. To overcome the robustness shortcomings, a formulation in terms of boundary-normal, one-dimensional characteristic variables is chosen in combination with modifications for the dual time-stepping approach of the unsteady flow solver. This allows for an appropriate relaxation of incoming characteristics in pseudo-time while the propagation of different wave types can be realized correctly in physical time (for details see Sections 3.4.3 and following). To deal with the non-local nature of the spectral NRBC in time, an approach similar to the shape correction method, which is used to address the same issue in the context of phase-shifted, periodic boundaries, is employed (for details see Section 3.4.1).

3 Theory and implementation

3.1 Flow equations and discretization approach

Before non-reflecting boundary conditions are discussed in the subsequent sections, this section outlines some basics. These will either serve later as a starting point for the theoretical derivation of NRBC or familiarity with these basics will be required for the discussion of implementation details. However, this section is not supposed to provide a thorough introduction into CFD.

3.1.1 URANS equations

As mentioned in Chapter 1, the scope of this work is limited to URANS-based simulations of turbomachinery flows. The URANS equations represent the physical principles of mass, momentum and energy conservation, assuming that turbulent fluctuations occur on scales much smaller than the ones resolved by the temporally and spatially discretized flow field. The effect of turbulence is therefore considered in the form of a statistical model. Note that the compressible flow equations are actually Favre- and Reynolds-averaged, but the final set of equations is commonly referred to as the (U)RANS equations.

Using Boussinesq's eddy viscosity assumption (see e.g. Wilcox, 2006), the URANS equations for a stationary frame of reference in conservative form and Cartesian coordinates read

$$\frac{\partial}{\partial t}U + \frac{\partial}{\partial x}\left(F^E + F^D\right) + \frac{\partial}{\partial y}\left(G^E + G^D\right) + \frac{\partial}{\partial z}\left(H^E + H^D\right) = 0 \tag{3.1}$$

with the vector of conservative variables

$$U = \begin{pmatrix} \varrho \\ \varrho u \\ \varrho v \\ \varrho w \\ \varrho E \end{pmatrix} \tag{3.2}$$

and the inviscid, convective fluxes

$$F^E = \begin{pmatrix} \varrho u \\ \varrho u^2 + p \\ \varrho uv \\ \varrho uw \\ u\left(\varrho E + p\right) \end{pmatrix}, G^E = \begin{pmatrix} \varrho v \\ \varrho uv \\ \varrho v^2 + p \\ \varrho vw \\ v\left(\varrho E + p\right) \end{pmatrix}, H^E = \begin{pmatrix} \varrho w \\ \varrho uw \\ \varrho vw \\ \varrho w^2 + p \\ w\left(\varrho E + p\right) \end{pmatrix} \tag{3.3}$$

as well as the viscous, diffusive fluxes

$$F^D = \begin{pmatrix} 0 \\ \sigma_{xx} \\ \sigma_{xy} \\ \sigma_{xz} \\ u\sigma_{xx} + v\sigma_{xy} + w\sigma_{xz} - \lambda^* \frac{\partial T}{\partial x} \end{pmatrix}, G^D = \begin{pmatrix} 0 \\ \sigma_{xy} \\ \sigma_{yy} \\ \sigma_{yz} \\ u\sigma_{xy} + v\sigma_{yy} + w\sigma_{yz} - \lambda^* \frac{\partial T}{\partial y} \end{pmatrix},$$

$$H^D = \begin{pmatrix} 0 \\ \sigma_{xz} \\ \sigma_{yz} \\ \sigma_{zz} \\ u\sigma_{xz} + v\sigma_{yz} + w\sigma_{zz} - \lambda^* \frac{\partial T}{\partial z} \end{pmatrix}. \tag{3.4}$$

For brevity, we write the effective, viscous stress tensor in Einstein's summation notation

$$\sigma_{ij} = -\mu^* \left[\left(\frac{\partial u_j}{\partial x_i} + \frac{\partial u_i}{\partial x_j} \right) - \frac{2}{3} \frac{\partial u_k}{\partial x_k} \delta_{ij} \right] + \frac{2}{3} \varrho \kappa \delta_{ij} \tag{3.5}$$

with the Kronecker delta δ_{ij}, effective dynamic viscosity

$$\mu^* = \mu + \mu_t \tag{3.6}$$

and effective thermal conductivity

$$\lambda^* = c_p \left(\frac{\mu}{Pr} + \frac{\mu_t}{Pr_t} \right). \tag{3.7}$$

The so-called eddy viscosity μ_t and the turbulent kinetic energy κ are obtained from a corresponding turbulence model. In this work, the k-ω model by Wilcox (1988) is employed. The Prandtl number Pr is a property of the fluid, while the turbulent Prandtl number Pr_t needs to be modelled appropriately depending on the flow situation. Molecular diffusion and turbulent transport of turbulent kinetic energy are omitted in the energy equation. This approximation is quite common and valid for subsonic, transonic and supersonic (but not hypersonic) flows (see Blazek, 2001).

Further, we assume calorically perfect gas satisfying the following equations of state

$$p = \varrho R T, \quad E = c_v T + \frac{V^2}{2} = \frac{1}{\gamma - 1} \frac{p}{\varrho} + \frac{V^2}{2}, \quad \gamma = \frac{c_p}{c_v} = \frac{c_p}{c_p - R} = \text{const.} \tag{3.8}$$

with $V = (u, v, w)$.

3.1.2 Finite volume method and boundary ghost cells

This section describes some fundamentals of the finite volume method in order to explain the concept of ghost cells for imposing boundary conditions on a cell-centred finite volume scheme. Using Gauss's theorem, we can rewrite Equation (3.1) and obtain

$$\int_{V_c} \frac{\partial U}{\partial t} dV + \oint_{\partial V_c} (\mathcal{F} \cdot n) \, dA = 0 \tag{3.9}$$

with the three-dimensional flux vector

$$\mathcal{F} = \begin{pmatrix} F^E + F^D \\ G^E + G^D \\ H^E + H^D \end{pmatrix}. \tag{3.10}$$

V_c denotes a control volume with the outward pointing surface-normal unit vector n.

In order to solve, the system numerically, one divides the computational domain into many (usually convex) polyhedra, so-called cells. The state within each cell of volume V_c is assumed to be uniform and, accordingly, fluxes across interfaces between cells are also uniform. Therefore, a semi-discrete form of the above equation reads

$$V_c \frac{\partial U}{\partial t} + \sum_f^{N_{faces}} \left(\mathcal{F}_f \cdot n_f \right) A_f = 0. \tag{3.11}$$

Time is still a continuous coordinate and, hence, there is still a temporal derivative in the equation. In this work, only structured hexahedra meshes are used, i.e. $N_{faces} = 6$.
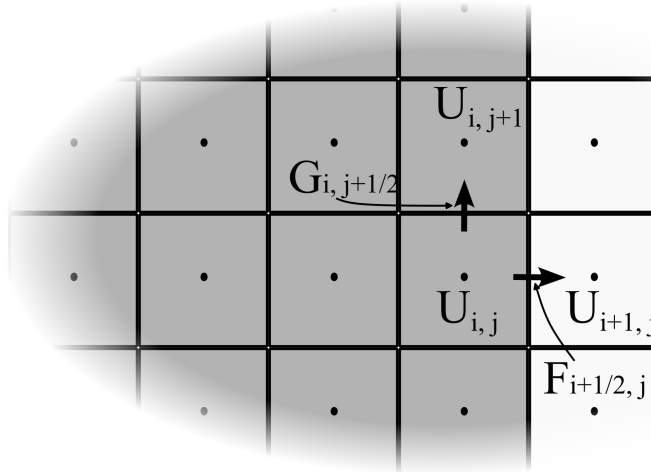

Figure 3.1: Detail of a Cartesian, cell-centred finite volume mesh at a boundary of a computational domain (grey) with a layer of ghost cells (white).

For the sake of simplicity, we consider a structured, two-dimensional, uniform, Cartesian mesh here for the introduction of the ghost cell concept. An extension to non-uniform, curvilinear, body-fitted meshes leads to additional metric terms representing an arbitrary mesh geometry (see e.g. LeVeque, 2002). Figure 3.1 depicts the boundary region of a computational domain.

The finite volume method requires the evaluation of fluxes at all cell faces. Within the computational domain, the fluxes are calculated as functions of neighbouring cell states, e.g. the flux $G_{i,j+1/2}$ in Figure 3.1. The stencil, i.e. the pattern of involved cells for the computation of a flux at a given cell interface, depends on the discretization scheme and may extend beyond directly adjacent cells.

In this work, convective fluxes are evaluated with Roe's flux-difference splitting method (Roe, 1981) extended to second-order accuracy by means of a MUSCL extrapolation scheme (van Leer, 1979) and a suitable slope limiter (van Albada *et al.*, 1982). Diffusive fluxes are computed with a second-order accurate central scheme.

In case of cell-centred approaches like in Figure 3.1, the boundary surface of the computational domain consists of faces of the outermost layer of (inner) cells. Accordingly, the formulation of boundary conditions for an (initial) boundary value problem corresponds to the prescription of an equivalent boundary flux across each boundary face for the finite volume method.

For this purpose, one or more layers of so-called ghost cells are added, depending on the scheme used to evaluate the flux functions at cell interfaces. With this approach, the finite volume algorithm can be applied to all inner cells including the outermost layer and all face fluxes are determined as functions of the neighbouring cells as illustrated by the flux $F_{i+1/2,j}$ in the sketch. Thus, the prescription of boundary fluxes requires the definition of corresponding ghost cell states. The specific procedure to define the ghost cell states depends on the physical boundary condition. For example, periodic boundary conditions can be realized by adding two layers of ghost cells (for the scheme described above) and copying the states of the corresponding cells from the respective opposite boundary of the computational domain. Then the same discretization scheme as in the interior is employed to evaluate the fluxes.

For inflow and outflow boundaries, a different technique can be used. First, one determines the ideal boundary face state using e.g. a non-reflecting boundary condition. In a second step, the face state is extrapolated to the ghost cell such that the extrapolation procedure is consistent with the subsequent flux evaluation method. The easiest way of doing this is by means of a linear extrapolation using the adjacent inner state U_i and the boundary face state U_f to obtain the state in the first ghost cell U_o:

$$U_o = 2U_f - U_i \tag{3.12}$$

Then,

$$\mathcal{F}_f = \mathcal{F}\left(\frac{1}{2}(U_i + U_o)\right) \tag{3.13}$$

provides an exact flux and a second layer of ghost cells is not needed.

In contrast to fluxes within the computational domain or e.g. at periodic boundaries, this central expression for convective fluxes does not lead to instabilities at inflow or outflow boundaries. Discretization schemes for nonlinear, convective fluxes as described above are usually comparatively complex in order to provide stability and accuracy at the same time because the scheme must reflect in a physically correct manner how information is spread in space (see e.g. Toro, 1999). However, if the boundary state at an inflow or outflow is determined with an appropriate boundary condition, this state and the corresponding flux already incorporate the physically correct propagation processes (see Sections 3.2 and 3.4).

The above approach appears more complex than just evaluating $\mathcal{F}(U_f)$ directly. However, by taking the detour via ghost cells, it is possible to implement a computationally efficient finite volume algorithm for all inner cells without exceptions for boundary cells.

3.1.3   Dual time-stepping

This section outlines the concept of pseudo-time integration and dual time-stepping as it will be crucial for the implementation of the unsteady boundary condition to properly distinguish physical time steps from pseudo-time steps. Before we consider

dual time-stepping, the pseudo-time stepping technique is introduced on the basis of the steady-state equations.

For this purpose, we replace the physical time t by an auxiliary time-like variable τ, called pseudo-time, and introduce a residual function $\mathcal{R}$, which represents the flux balance, i.e. the entire spatial discretization:

$$\mathcal{R}(U) = -\frac{1}{V_c} \sum_f^{N_{faces}} (\mathcal{F}_f \cdot n_f) A_f \tag{3.14}$$

To solve the steady RANS equations, we now seek the equilibrium flow state such that the pseudo-time derivative vanishes. From Equation (3.11) follows:

$$\frac{\partial U}{\partial \tau} = \mathcal{R}(U) \to 0 \tag{3.15}$$

With a suitable time-stepping algorithm, we can march from an initial solution in pseudo-time until a steady state is found (satisfying an acceptable convergence criterion). For efficiency reasons, we want to choose the pseudo-time step size as large as possible. Since explicit schemes are unstable for large time steps due to the CFL condition (see Courant *et al.*, 1928), an implicit algorithm is more advantageous. Therefore, we write the implicit system using a simple finite difference approach for the temporal discretization.

$$\frac{\Delta U^i}{\Delta \tau} = \frac{U^{i+1} - U^i}{\Delta \tau} = \mathcal{R}(U^{i+1}) \tag{3.16}$$

where i denotes the pseudo-time step. The system is called implicit because the right-hand side is a function of the unknown state at time step $i + 1$. Therefore, $\mathcal{R}(U^{i+1})$ is approximated with a Taylor series expansion:

$$\mathcal{R}(U^{i+1}) = \mathcal{R}(U^i) + \left.\frac{\partial \mathcal{R}}{\partial U}\right|^i \Delta U^i + \mathcal{O}\left(\Delta U^2\right) \tag{3.17}$$

Inserting Equation (3.17) into Equation (3.16) and rearranging gives

$$\left(\frac{1}{\Delta \tau} I - \left.\frac{\partial \mathcal{R}}{\partial U}\right|^i\right) \Delta U^i = \mathcal{R}(U^i). \tag{3.18}$$

This is a linear system of equations that can be solved numerically.

The pseudo-time method can also be applied to implicit time integration for unsteady flows. In this case, we reintroduce the physical time derivative and obtain

$$\frac{\Delta U^i}{\Delta \tau} = \mathcal{R}(U^{i+1}) - \left.\frac{\partial U}{\partial t}\right|^{i+1} \to 0 \tag{3.19}$$

The time derivative is approximated with a finite difference stencil, e.g. using the popular two-step backward differentiation formula (BDF2, see e.g. Dahmen & Reusken, 2008):

$$\left.\frac{\partial U}{\partial t}\right|^{n+1} \approx \frac{1}{2\Delta t}\left(3U^{n+1} - 4U^n + U^{n-1}\right) \tag{3.20}$$

Note that index n designates physical time levels here while in the equation above i is associated with pseudo-time levels. Since the pseudo-time approach serves as an iteration technique to solve the implicit system for each physical time step, U^{i+1} is the best approximation of U^{n+1} and, thus, U^{i+1} replaces U^{n+1}. Substituting again $\mathcal{R}(U^{i+1})$ by its Taylor approximation (Eq. (3.17)) in Equation (3.19) and using Equation (3.20), yields

$$\left(\frac{1}{\Delta\tau}I + \frac{3}{2\Delta t}I - \left.\frac{\partial\mathcal{R}}{\partial U}\right|^{i} \right) \Delta U^{i} = \mathcal{R}(U^{i}) - \frac{1}{2\Delta t}\left(3U^{i} - 4U^{n} + U^{n-1} \right) \tag{3.21}$$

As in the steady case, this linear system can be solved numerically. It provides an update for the pseudo-time iteration loop until the solution is converged. At the beginning of each physical time step, the final solution of the previous physical time step is used as a starting point for the pseudo-time iteration loop ($U^{i=0} = U^{n}$).

In both the steady and the unsteady algorithm, the residual Jacobian matrix $\frac{\partial\mathcal{R}}{\partial U}$ contains the Jacobians matrices of the numerical flux functions and can therefore become relatively complicated depending on the underlying spatial discretization. However, if the system converges and ΔU vanishes, the accuracy of the final solution depends on the right-hand sides of Equations (3.18) and (3.21) only. Therefore, the residual Jacobian matrix does not need to be exact and can be simplified in order to reduce the computational effort needed for the solution of the linear system or to increase the stability of the iteration algorithm (see Nürnberger, 2004).

3.2   Fundamentals of spectral NRBC

3.2.1   From URANS equations to the dispersion relation

The concept of the NRBC presented in this paper is to consider the boundary flow field in the spectral domain, i.e. in the wavenumber and frequency domain. Here, the flow can be decomposed into waves with known propagation properties. To attain non-reflecting behaviour of artificial open boundaries, incoming waves can easily be suppressed by setting their amplitude to zero and reconstructing the flow in the physical domain, i.e. in time and space, allowing only outward travelling disturbances from the mean flow.

To derive such NRBC for three-dimensional flows, we need to introduce some assumptions and thereby simplify the underlying equations. Thus, the NRBC presented in this work are only perfectly non-reflecting if these assumptions apply. In general, these prerequisites are not strictly fulfilled when dealing with realistic turbomachinery applications and the accuracy, viz. the suppression of undesired numerical reflections, depends on how well our assumptions are met. Yet, we will see in Chapters 4 and 5 that the NRBC presented in this work still reduce these reflections at least significantly, often even so that artificial reflections are no longer a factor to the analysis of numerical results.

Although we use the NRBC to solve the URANS equations, we assume that the boundary flow field can be considered inviscid to a sufficient approximation. That means viscous effects may play a crucial role within the computational domain, but not at its open boundaries (in contrast to solid walls). For example, the wake of a blade, secondary flow vortices or hot streaks originate somewhere in the interior and grow due

to diffusion while they are convected to the open boundary. At the boundary, however, we assume that diffusion can be disregarded locally and the predominant transport mechanism is convection. We will see later that such effects represent entropy and vorticity distortions in this context and they are convected along streamlines. If we locally disregard viscosity and heat conductivity, the boundary flow field is described by the time-dependent Euler equations instead by the URANS equations. The former are mathematically characterized as purely hyperbolic which facilitates the following approach to decompose the boundary flow field into distortions of known direction of propagation.

Moreover, the flow is required to be subsonic in boundary-normal direction and not completely at rest. This does not present a real restriction as supersonic inflow and outflow boundary conditions are trivial and not subject to artificial reflections. Their definition can be found in many basic CFD textbooks e.g. Hirsch (1990). When running CFD simulations, it must be known beforehand if the boundary flow conditions are supersonic in boundary-normal direction because, in that case, one additional quantity needs to be specified at the inlet and no boundary value can be specified at the outflow.

We further assume that effects in blade-to-blade surfaces dominate variations in spanwise direction. The resulting two-dimensional boundary condition can then be applied at arc segments of constant radial and axial position along the boundary surface in a quasi-three-dimensional fashion according to the extension Saxer & Giles (1993) have proposed to extend Giles's originally two-dimensional NRBCs to three spatial dimensions. By applying the two-dimensional NRBC at arcs of constant radius, it is assumed that the corresponding stream surfaces are decoupled (see Section 3.4.2 and the illustration there). The theory of spectral NRBC is not per se limited to two-dimensions. In fact, three-dimensional mode decomposition techniques have successfully been utilized for NRBC in frequency domain methods (see Section 2.3 and references therein). However, with a given frequency a two-dimensional problem has to be solved at the boundary and the associated computational effort can be significant (cf. Petrie-Repar, 2010). In a time domain simulation, the modal analysis needs to be conducted at every discrete frequency of the spectrum yielding an additional, temporal dimension. Therefore the boundary condition will become a three-dimensional problem itself (in two spatial and one temporal dimension) and the expected computational effort might prohibit the use of such a boundary condition in large time domain simulations that are costly anyway. Beyond, three-dimensional NRBCs are, as well as their two-dimensional counterpart, subject to restrictions regarding the underlying mean flow and duct geometry. If the flow is not uniform in axial and circumferential direction, the modal analysis is much more intricate (see e.g. Rienstra, 1999). Hence, three-dimensional NRBCs are not as universal as their label might suggest. Kersken *et al.* (2014) show that, starting from simple one-dimensional boundary conditions, one gains the most significant improvement by incorporating the circumference as second spatial dimension and the impact of adding the third spatial dimension is much less substantial in a LPT flutter study.

For those reasons, in this work the quasi-three-dimensional approach is pursued. This approach, however, requires the definition of rotational surfaces in which the two-dimensional Euler equations are considered. Employing the quasi-three-dimensional approach to realistic turbomachinery configurations is not straightforward as there is no natural choice to define such rotational surfaces. In general, the computational domain is not always bounded by planes of constant axial position, e.g. when dealing with modern three-dimensional blade designs and small axial gaps between blade

rows. Moreover, the annulus geometry might deviate from purely cylindrical endwalls causing the flow to deviate from simplified, purely axial or axially constant mean flow conditions as well (e.g. see Chapter 5.1). In these situations, the question arises how the above mentioned surfaces should be defined appropriately. The first degree of freedom for such a rotational surface is obviously given by the circumferential direction. However, there are two options that seem to be plausible choices for the second coordinate. One is the mean meridional velocity vector. With this choice, the mean out-of-plane velocity component vanishes and the reference surface is a genuine (temporally and circumferentially averaged) stream surface. This definition is in particular motivated by considering the 2D Euler equations and the subsequent wave propagation analysis in such a stream surface. On the other hand, in case of non-cylindrical stream surfaces, the prerequisite of the flow being homogenous in axial direction is violated anyway. Moreover, we will formulate the spectral NRBC in terms of one-dimensional characteristics because for hyperbolic systems, well-posed initial-boundary value problems can be formulated using boundary conditions based on bounded, boundary-normal, incoming characteristics (see Kreiss (1970) or Higdon (1986*b*)). Hence, the boundary-normal direction appears to be the suitable choice with regard to well-posedness.

A detailed description and analysis based on the pseudo-time harmonic balance solver in TRACE is given by Frey *et al.* (2020) and Wolfrum *et al.* (2020). It has been found that the formulation based on the mean meridional velocity vector may yield superior reflection behaviour in elementary duct flows with strongly inclined interfaces. However, the analysis of unsteady blade forces induced by the wake of a TMTF on a subsequent LPT rotor did not support this clear advantage of the meridional velocity-based formulation. Both options are implemented and available for the time domain spectral NRBC presented in this work. Yet, the default definition is chosen to be the option using the boundary-normal vector as, from the author's experience, the meridional velocity vector-based formulation sometimes impairs the convergence of time domain simulations. This can be explained by the fact, that the boundary normal is constant whereas the meridional velocity vector might vary, in particular during transient phases at the beginning of a simulation before the flow reaches periodic convergence. It is therefore no surprise that a coordinate system being itself a function of the solution is not helpful to the stability and fast convergence of numerical simulations. Accordingly, computations of both three-dimensional test cases in Chapter 5 are conducted using the boundary-normal to define the rotational surface.

Note that in this chapter, the coordinate system for the two-dimensional approach is based on either of the surface definitions discussed above. Coordinates x and y with their respective velocity components u and v are defined locally at the boundary. While coordinate y denotes the circumferential direction, coordinate x is perpendicular to y, but either parallel to the mean meridional velocity vector or to the boundary-normal vector at that radial position. In case of the boundary-normal option, the reference vector points into the computational domain at inflow boundaries and out of the domain at outflow boundaries, such that the corresponding velocity component u always takes positive values. Coordinate z and the corresponding velocity component w are associated with the out-of-plane direction.

With the above assumptions of axially and circumferentially uniform, inviscid flow along stream surfaces of constant or slowly varying radii, we can apply the governing set of equations in stationary or rotating frames of reference, neglecting centrifugal and Coriolis forces. Equations (3.1)-(3.3) reduce to the two-dimensional or better quasi-

three-dimensional Euler equations in conservative variables

$$\frac{\partial}{\partial t}U + \frac{\partial}{\partial x}F^E(U) + \frac{\partial}{\partial y}G^E(U) = 0 \tag{3.22}$$

We can expand the spatial derivatives of the Euler fluxes in Equation (3.22) using their Jacobians with respect to the vector of conservative variables and obtain

$$\frac{\partial}{\partial t}U + \frac{\partial F^E}{\partial U}\frac{\partial U}{\partial x} + \frac{\partial G^E}{\partial U}\frac{\partial U}{\partial y} = 0. \tag{3.23}$$

Moreover, we introduce the vector of primitive variables $q = (\varrho, u, v, w, p)$, the associated variable transformation $\frac{\partial U}{\partial q}$ and its inverse $\frac{\partial q}{\partial U}$. Rearranging Equation (3.23) in terms of primitive variables yields

$$\frac{\partial}{\partial t}q + \frac{\partial q}{\partial U}\frac{\partial F^E}{\partial U}\frac{\partial U}{\partial q}\frac{\partial q}{\partial x} + \frac{\partial q}{\partial U}\frac{\partial G^E}{\partial U}\frac{\partial U}{\partial q}\frac{\partial q}{\partial y} = 0. \tag{3.24}$$

For brevity, we write this equation in a so-called quasi-linear form

$$\frac{\partial}{\partial t}q + A^*(q)\frac{\partial q}{\partial x} + B^*(q)\frac{\partial q}{\partial y} = 0 \tag{3.25}$$

with

$$A^*(q) = \frac{\partial q}{\partial U}\frac{\partial F^E}{\partial U}\frac{\partial U}{\partial q} \quad \text{and } B^*(q) = \frac{\partial q}{\partial U}\frac{\partial G^E}{\partial U}\frac{\partial U}{\partial q}. \tag{3.26}$$

The next crucial step is to write the local flow state along the boundary, at constant radial and axial position, as the sum of a local perturbation q' and a circumferentially and temporally area-averaged mean state $\overline{q}$

$$q = \overline{q} + q' \tag{3.27}$$

with

$$\overline{q} = \frac{1}{TA}\int_T\int_A dA\,dt \tag{3.28}$$

and assume the perturbations are sufficiently small. If we then freeze A and B at the mean state, they read:

$$A := A^*(\overline{q}) = \begin{pmatrix} \overline{u} & \overline{\varrho} & 0 & 0 & 0 \\ 0 & \overline{u} & 0 & 0 & 1/\overline{\varrho} \\ 0 & 0 & \overline{u} & 0 & 0 \\ 0 & 0 & 0 & \overline{u} & 0 \\ 0 & \gamma\overline{p} & 0 & 0 & \overline{u} \end{pmatrix}, \quad B := B^*(\overline{q}) = \begin{pmatrix} \overline{v} & 0 & \overline{\varrho} & 0 & 0 \\ 0 & \overline{v} & 0 & 0 & 0 \\ 0 & 0 & \overline{v} & 0 & 1/\overline{\varrho} \\ 0 & 0 & 0 & \overline{v} & 0 \\ 0 & 0 & \gamma\overline{p} & 0 & \overline{v} \end{pmatrix} \tag{3.29}$$

With constant matrices A and B, the system is now indeed linear. As mentioned earlier, we postulate that the mean flow is approximately constant in axial direction. Hence, the mean state alone is a trivial solution and, due to linearity, the perturbation is also a solution to the linear system

$$\frac{\partial q'}{\partial t} + A\frac{\partial q'}{\partial x} + B\frac{\partial q'}{\partial y} = 0. \tag{3.30}$$

Again owing to the linear nature of Equation (3.30), we can without loss of generality assemble an arbitrary, spatially and temporally periodic boundary field by superposition of Fourier modes of the following form:

$$q' = \text{Re}\left(\hat{q}\, e^{\text{i}(kx+ly+\omega t)}\right) \tag{3.31}$$

Substituting Equation (3.31) into Equation (3.30), we obtain

$$(\omega I + kA + lB)\,\hat{q} = 0. \tag{3.32}$$

With non-trivial solution $\hat{q}$, this yields

$$\det(\omega I + kA + lB) = 0. \tag{3.33}$$

As this equation relates the wavenumber components k and l to the angular frequency ω, it helps determine how waves associated with such Fourier modes propagate. Equation (3.33) is called dispersion relation and it is a polynomial equation of degree five in k, l and ω for A and B are 5×5 matrices.

3.2.2   Modal decomposition and wave propagation

We can interpret the dispersion relation (3.33) as the characteristic polynomial to an eigenvalue problem

$$(kA + lB)r_i = -\omega_i r_i \tag{3.34}$$

with eigenvalues $-\omega_i$ and eigenvectors r_i. When developing boundary conditions, however, we can express the boundary flow field in its spectral representation, i.e. we can conduct Fourier transforms in time and in circumferential direction. Details on implementing this step and its implications, in particular for time marching computations, are addressed in Section 3.4. With known circumferential wavenumbers l and angular frequencies ω, it is beneficial to multiply Equation (3.32) from the left by A^{-1} and obtain

$$\left(\omega A^{-1} + kI + lA^{-1}B\right) r_i = 0. \tag{3.35}$$

Equation (3.35) is an eigenvalue problem with the same eigenvectors r_i, but eigenvalues $-k_i$. This means, with given circumferential wavenumber l and frequency ω, we can calculate the boundary-normal wavenumber k_i and thereby identify whether a wave enters or leaves the computational domain as we will discuss later in this section. In fact, it is not necessary to compute A^{-1} explicitly because the characteristic polynomial to Equation (3.35)

$$\det\left(A^{-1}\left(\omega I + kA + lB\right)\right) = \det\left(A^{-1}\right)\det\left(\omega I + kA + lB\right) = 0 \tag{3.36}$$

is equivalent to Equation (3.33) since A is neither a function of k, l or ω nor singular for non-vanishing $\overline{u}$. Thus, we can instead solve Equation (3.33) for its five roots k_i. Here, it is convenient to introduce an auxiliary variable

$$\widetilde{\omega} = \omega + \overline{v}l \tag{3.37}$$

which can be understood as the Doppler-shifted angular frequency one detects in a virtual reference frame that rotates with circumferential velocity $\overline{v}$ so that in this virtual reference frame the mean flow is purely axial. Expanding Equation (3.33) then yields

$$(\widetilde{\omega} + \overline{u}k)^3 \left((\widetilde{\omega} + \overline{u}k)^2 - \overline{a}^2\left(l^2 + k^2\right)\right) = 0 \tag{3.38}$$

with speed of sound $\bar{a} = \sqrt{\gamma\frac{\bar{p}}{\bar{\varrho}}}$. From Equation (3.38), we can easily identify a triple eigenvalue

$$k_{1,2,3} = -\frac{\tilde{\omega}}{\bar{u}}. \tag{3.39}$$

Since the algebraic multiplicity of this vector is three, the construction of the corresponding eigenvectors is not unique. We will use the following definition for two reasons. Firstly, it is easy to see that $r_{1,2,3}$ are mutually orthogonal and hence the geometric multiplicity of $k_{1,2,3}$ equals its algebraic multiplicity. This is crucial to our approach to use the eigenvectors as a new basis for the decomposition of the flow field into waves with known propagation properties. Secondly, this choice offers a rather simple physical interpretation.

$$r_1 = \begin{pmatrix} -\bar{\varrho} \\ 0 \\ 0 \\ 0 \\ 0 \end{pmatrix}, \quad r_2 = \begin{pmatrix} 0 \\ \bar{a}rl \\ -\bar{a}rk_2 \\ 0 \\ 0 \end{pmatrix}, \quad r_3 = \begin{pmatrix} 0 \\ 0 \\ 0 \\ \bar{a} \\ 0 \end{pmatrix} \tag{3.40}$$

By only affecting density, r_1 expresses the change in primitive variables induced by an entropy wave. While r_2 induces a velocity perturbation along the wavefront and can therefore be understood as a vorticity or shear wave in the x-y-streamsurface, r_3 induces out-of-plane velocity fluctuations.

To determine the waves' direction of propagation with respect to the boundary, the group velocity $u_g = -\frac{\partial\omega}{\partial k}$ rather than the phase velocity $u_\varphi = -\frac{\omega}{k}$ is of interest since only the former describes energy transport. If the boundary-normal wavenumber is proportional to the frequency, group and phase velocity are equal. This is, for example, true for one-dimensional acoustic waves. Yet, for multi-dimensional problems, dispersion relations provide in general nonlinear relationships between wavenumbers and frequencies and therefore the phase velocity is not meaningful for our purpose. The interested reader is referred to Whitham (1974) for a comprehensive deep dive or to Higdon (1986b) to learn more about this in the context of boundary condition theory. The boundary-normal group velocity component associated to the first three eigenvectors is

$$u_g(k_{1,2,3}) = -\frac{\partial\omega}{\partial k_{1,2,3}} = -\left(\frac{\partial k_{1,2,3}}{\partial\omega}\right)^{-1} = \bar{u}. \tag{3.41}$$

This means the entropy and vorticity waves are simply convected with the mean flow without any change in shape or magnitude. Thus, they are incoming perturbations at an inflow boundary and outgoing ones at an outflow boundary.

From the remaining quadratic part of the characteristic polynomial (Eq. (3.38)), we can calculate the fourth and fifth eigenvalues

$$k_4 = \frac{\tilde{\omega}\left(\bar{u} - \bar{a}\chi\right)}{\bar{a}^2 - \bar{u}^2} \quad \text{and} \quad k_5 = \frac{\tilde{\omega}\left(\bar{u} + \bar{a}\chi\right)}{\bar{a}^2 - \bar{u}^2} \tag{3.42}$$

with

$$\chi = \begin{cases} \sqrt{1 - \xi^2} & \text{if } \xi \leq 1 \\ -i\,\mathrm{sign}\,(\tilde{\omega})\,\sqrt{\xi^2 - 1} & \text{if } \xi > 1 \end{cases} \tag{3.43}$$

and the definition of the cut-off ratio

$$\xi = \left| \frac{l\sqrt{\overline{a}^2 - \overline{u}^2}}{\widetilde{\omega}} \right| = \frac{\omega_c}{\omega}. \tag{3.44}$$

Here, ω_c denotes the critical frequency and the significance of the cut-off ratio and the critical frequency will be discussed below. It should be noted here that some authors refer to the quadratic frequency ratio as the cut-off ratio and others prefer its reciprocal. However, in the author's view, the latter should rather be named normalized frequency or cut-on ratio as large values (> 1) describe cut-on modes.

The corresponding eigenvectors read:

$$r_{4,5} = \begin{pmatrix} \overline{\varrho} \\ \frac{-\overline{a}^2 k_{4,5}}{\widetilde{\omega} + u k_{4,5}} \\ \frac{-\overline{a}^2 l}{\widetilde{\omega} + u k_{4,5}} \\ 0 \\ \gamma p \end{pmatrix} \tag{3.45}$$

As they constitute isentropic changes of state and irrotational velocity perturbations, they describe acoustic waves. Again, their propagation properties can be derived from their eigenvalues r_4 and r_5.

For sufficiently large frequencies, viz. cut-off ratios $\xi < 1$, we obtain real values for χ and thus the eigenvalues are real-valued as well. From Equation (3.31), we find that in this case the wave propagates without attenuation, i.e. with constant amplitude. Such a mode is called cut-on. To discern their direction of propagation with respect to the boundary, we examine the group velocity. After some lines of pen and paper work (Others may call it straightforward algebra, but that seems a little presumptuous for an engineering PhD candidate.), we obtain:

$$u_g(k_4) = -\frac{\partial \omega}{\partial k_4} = \left(-\frac{\partial k_4}{\partial \omega} \right)^{-1} = \frac{\overline{a}^2 - \overline{u}^2}{\frac{\overline{a}}{\chi} - \overline{u}} \tag{3.46}$$

With $\xi < 1$ and therefore $0 < \chi \leq 1$ and $0 < \overline{u} < \overline{a}$, we see that $u_g(k_4) > 0$ and hence the wave associated with r_4 is a downstream travelling, acoustic wave. Likewise we calculate

$$u_g(k_5) = -\frac{\partial \omega}{\partial k_5} = \left(-\frac{\partial k_5}{\partial \omega} \right)^{-1} = -\frac{\overline{a}^2 - \overline{u}^2}{\overline{u} + \frac{\overline{a}}{\chi}} \tag{3.47}$$

which reveals that the wave associated with r_5 is an upstream travelling wave, i.e. $u_g(k_5) < 0$.

On the other hand, from Equations (3.42) and (3.43) it becomes evident that with cut-off ratio $\xi > 1$ the acoustic modes become complex-valued. In that case, the definition of Fourier modes (Eq. (3.31)) can be revisited in order to study the propagation characteristics. It can be rearranged to

$$q' = \text{Re} \left(\hat{q} \, e^{-\text{Im}(k)x} \, e^{\text{i}(\text{Re}(k)x + ly + \omega t)} \right) \tag{3.48}$$

where $\hat{q} \, e^{-\text{Im}(k)x}$ can be understood as an amplitude that decays or grows in axial direction depending on the sign of the imaginary part of k_4 and k_5 respectively Thus, when taking the square root of the negative radicand $1 - \xi^2$, we must choose the correct

branch by defining the sign of the root such that the wave associated with k_4 travels downstream while the wave associated with k_5 travels upstream. With the definition in Equation (3.43), we make sure that k_4 has a positive imaginary part and therefore decays in positive x-direction. As the amplitude of a single wave cannot increase while propagating in uniform flow, this is equivalent to the wave associated with k_4 travelling downstream. Analogously, this definition guarantees $\mathrm{Im}(k_5) < 0$ and with the same reasoning the corresponding acoustic wave must travel upstream. The important feature is that these propagation directions are consistent to the cut-on case $\xi < 1$. As with $\xi > 1$ the acoustic waves decay in their respective direction of propagation, they are called cut-off.

Note that the singularity of $k_{4,5}$ at $\widetilde{\omega} = 0$ is removable. Equations (3.42) and the following can easily be rewritten such that the $\widetilde{\omega}$ in the denominator of the definition of ξ is extracted and eventually cancelled out. Yet, the above notation is chosen to explicitly keep the cut-off ratio in the equation and thereby point out more clearly the significance of the cut-off ratio to the nature of acoustic modes. For the sake of completeness, we define

$$k_4\big|_{\widetilde{\omega}=0} := \frac{\mathrm{i}\,|l|\,\overline{a}}{\sqrt{\overline{a}^2 - \overline{u}^2}} \qquad \text{and} \qquad k_5\big|_{\widetilde{\omega}=0} := \frac{-\mathrm{i}\,|l|\,\overline{a}}{\sqrt{\overline{a}^2 - \overline{u}^2}}. \tag{3.49}$$

The phenomenon at $\xi = 1$ is referred to as acoustic resonance. From Equations (3.42) and (3.43), it is evident that k_4 and k_5 become equal and therefore also the corresponding eigenvectors r_4 and r_5 coincide. The mode decomposition approach, we are about to introduce, will collapse in that case since the eigenvectors no longer form a suitable basis. This implies that upstream and downstream travelling modes can no longer be discerned which poses a challenge to the construction of well-posed boundary conditions. In fact, the boundary-normal group velocity component vanishes (cf. Eqs. (3.46) and (3.47)), which means that the acoustic waves spin around the circumference and their energy is neither dissipated nor carried away. In the context of boundary conditions, we can circumvent this phenomenon by adding a small imaginary part to the otherwise real-valued angular frequency (only within the boundary condition formulation). This regularizes the modal decomposition because as a result the resonant modes become virtually cut-off. In other words, the imaginary part of the angular frequency is equivalent to artificial damping. The associated eigenvalues are then complex conjugates to each other which allows differentiating their direction of propagation or decay by means of their imaginary part. A thorough discussion of this technique is given by Frey & Kersken (2016). Their work deals with a frequency domain implementation of this regularization approach, but the physical and mathematical principle is identical. The authors show that the the impact of this regularization approach is limited to stabilizing the boundary condition under conditions close to acoustic resonance, but does not affect accuracy if the damping parameter is chosen sufficiently small. To not overcomplicate this chapter, we stick to the original formulation based on real-valued frequencies here keeping in mind that acoustic resonance and its mathematical implications are taken care of in the actual implementation.

The pivotal benefit of the presented eigenvector analysis is that we have found five linearly independent eigenvectors to form a basis in which our five-dimensional vector of primitive perturbation variables can be expressed as a linear combination of five types of waves, i.e. eigenvectors, with known propagation directions. Let α_i be the

amplitude of these fundamental waves, so we can write

$$q' = \text{Re}\left(\left[\sum_{i=1}^{5} \alpha_i r_i e^{ik_i x}\right] e^{i(ly+\omega t)}\right) \tag{3.50}$$

at each position of our spectrum in time and space, i.e. for each combination of known ω and l. Note that it is not necessary to calculate the group velocities in the actual implementation of the NRBC since we know that, for flows that are subsonic in boundary-normal direction, the first four eigenvectors are associated with downstream travelling waves and only the fifth mode runs upstream.

To determine the coefficients α_i of a given modal perturbation $\hat{q}$, Giles (1988) also introduces a set of left eigenvectors. We have utilized that the set of right eigenvectors is independent of left multiplying A^{-1} to Equation (3.32) in order to obtain an eigenvalue problem with eigenvalues $-k$. Yet, this is not true for left eigenvectors. Therefore, Giles proposes a way to analytically derive the left eigenvectors to the modified characteristic polynomial (Eq. (3.35)) without computing A^{-1}. Instead, the fact is exploited in this work that inverting the matrix of column-wise right eigenvectors

$$R = (r_1 \ r_2 \ r_3 \ r_4 \ r_5) \tag{3.51}$$

produces a matrix of row-wise left eigenvectors

$$L = \begin{pmatrix} l_1 \\ l_2 \\ l_3 \\ l_4 \\ l_5 \end{pmatrix}. \tag{3.52}$$

This can be verified easily as follows. If we define the diagonal matrix Λ containing the eigenvalues of an arbitrary, quadratic, regular matrix M whose right eigenvector matrix R^* has full rank, we can write:

$$MR^* = R^*\Lambda \Leftrightarrow R^{*-1}MR^* = \Lambda$$

Then defining $L^* = R^{*-1}$ shows that L^* constitutes a matrix of (row-wise) left eigenvectors:

$$L^*ML^{*-1} = \Lambda \Leftrightarrow L^*M = \Lambda L^*$$

Therefore, it is more convenient for us to compute L numerically. The key for constructing NRBC is that, with $LR = I$, we can use L to measure the portion of each fundamental wave type r_i in a given flow state $\hat{q}$. We define the modal decomposition

$$\hat{\alpha} = R^{-1}\hat{q} = L\hat{q} \tag{3.53}$$

with $\hat{\alpha}$ denoting the vector of amplitudes.

3.2.3   Specification of spectral non-reflecting boundary condition

The condition to avoid spurious reflections at artificial boundaries in the spectral domain is simply to suppress all waves that are identified as incoming by means of the modal decomposition introduced above. Accordingly, the boundary flow field then

contains only outwards travelling perturbations and no reflection can come back into the computational domain. Hence, we require for any discrete Fourier mode of the two-dimensional spectrum in space and time, viz. with given angular frequency ω and circumferential wavenumber l,

$$L^{in}_{(\omega,l)}\hat{q}_{(\omega,l)} = 0 \tag{3.54}$$

where $L^{in}_{(\omega,l)}$ only includes the rows of L that correspond to incoming waves. This means $L^{in}_{(\omega,l)} = (l_1, l_2, l_3, l_4)$ at inflow boundaries and $L^{in}_{(\omega,l)} = (l_5)$ at exists. The remaining rows belong to the matrix of left eigenvectors associated with outgoing waves $L^{out}_{(\omega,l)}$. In the same way, we distinguish right eigenvector matrices $R^{in}_{(\omega,l)}$ and $R^{out}_{(\omega,l)}$ with column-wise separation.

The zeroth harmonic in space and time $\hat{q}_{0,0}$ must be excluded from this condition as it represents the mean flow instead of perturbations. We will specify a different condition for this mode in Section 3.4 in order to meet the specified mean boundary values.

3.2.4 Imposing incoming modes

The modal decomposition can also be utilized to combine the prescription of unsteady, incoming disturbances with non-reflecting boundary conditions. Usually, when inhomogeneous, two-dimensional boundary value distributions are specified, e.g. to mimic incoming wakes of upstream components, the boundary becomes reflective to outgoing waves because of the local nature of the boundary condition. However, instead of removing all incoming modes at an interface when employing spectral NRBCs, we can also allow incoming disturbances by means of the modal decomposition if we can specify these disturbances in the spectral domain. For that, Equation (3.54) is extended by adding a right-hand side:

$$L^{in}_{(\omega,l)}\hat{q}_{(\omega,l)} = \hat{\alpha}^{in}_{(\omega,l)} \tag{3.55}$$

An example of this technique is demonstrated in Section 4.2 where we prescribe single, two-dimensional, acoustic modes at an inlet of an annular duct with axial mean flow. However, by providing a distribution with several modes to be superposed at each radial position, it is also possible to reconstruct more complex and more realistic inlet distortions such as, for example, the above mentioned wake of an upstream blade row.

3.3 Related NRBC formulations

In the following subsection, we will outline three types of boundary conditions that can be derived from the spectral NRBCs presented in the preceding part of this chapter. Those boundary conditions have been introduced by Giles (1988) and gained popularity in numerous turbomachinery CFD tools. Therefore, they are also studied in the validation and application part of this work in order to compare the spectral NRBC against them.

3.3.1 Characteristic, one-dimensional NRBC

A very common class of unsteady boundary conditions is based on one-dimensional, characteristic variables. These boundary conditions can be formulated local in space

and time and they are relatively simple to implement. Thus and due to their robustness, they are widely used although they provide, in general, only very limited suppression of artificial reflections.

Characteristics based, one-dimensional NRBC can be regarded as a special case of the more generally valid, two-dimensional NRBC. For one-dimensional flows, i.e. if all waves enter or leave the domain perpendicularly to the boundary, the circumferential wavenumber vanishes and the eigenvectors can be scaled such that they do no longer depend on ω:

$$
L_{1D} = \begin{pmatrix} \frac{-1}{\bar{\varrho}} & 0 & 0 & 0 & \frac{1}{\bar{\varrho}\bar{a}^2} \\ 0 & 0 & \frac{1}{\bar{a}} & 0 & 0 \\ 0 & 0 & 0 & \frac{1}{\bar{a}} & 0 \\ 0 & \frac{1}{\bar{a}} & 0 & 0 & \frac{1}{\bar{\varrho}\bar{a}^2} \\ 0 & \frac{-1}{\bar{a}} & 0 & 0 & \frac{1}{\bar{\varrho}\bar{a}^2} \end{pmatrix}, \quad R_{1D} = \begin{pmatrix} -\bar{\varrho} & 0 & 0 & \frac{\bar{\varrho}}{2} & \frac{\bar{\varrho}}{2} \\ 0 & 0 & 0 & \frac{\bar{a}}{2} & \frac{-\bar{a}}{2} \\ 0 & \bar{a} & 0 & 0 & 0 \\ 0 & 0 & \bar{a} & 0 & 0 \\ 0 & 0 & 0 & \frac{\bar{\varrho}\bar{a}^2}{2} & \frac{\bar{\varrho}\bar{a}^2}{2} \end{pmatrix} \tag{3.56}
$$

The characteristic variables (or short: characteristics) are then defined as

$$
c' = L_{1D}\, q'. \tag{3.57}
$$

As they solely depend on mean flow quantities, the one-dimensional boundary condition

$$
L_{1D}^{in}\, q' = c'^{\,in} = 0 \tag{3.58}
$$

can be applied locally without any prior Fourier transform in time and/or space. However, this is only true for the perturbation part. We still want to meet given boundary values in terms of temporally and circumferentially averaged, hence non-local, quantities. Therefore, we additionally prescribe a change in mean characteristics. This procedure is identical to the spectral NRBCs and covered in Section 3.4.

3.3.2 Approximate, unsteady, two-dimensional NRBC

To overcome the complication of implementing the spatially and temporally non-local, spectral NRBC in a time marching scheme, Giles (1988) proposes a local, approximate, two-dimensional, unsteady boundary condition. The central concept is to circumvent the dependence of the modal decomposition on the spectral representation of the boundary by approximating the modal decomposition matrix L in Equation (3.53) by means of a Taylor series expansion about the unsteady, one-dimensional condition. With an auxiliary variable $\lambda = \frac{l}{\omega}$, the second-order approximation of the left eigenvector matrix L reads

$$
L_a = L|_{\lambda=0} + \lambda \left.\frac{\partial L}{\partial \lambda}\right|_{\lambda=0} = L_{1d} + \frac{l}{\omega} \left.\frac{\partial L}{\partial \lambda}\right|_{\lambda=0}. \tag{3.59}
$$

Now the boundary condition $L_a^{in}\, q' = 0$ can be multiplied by ω. From Equations (3.31) and (3.32), we infer that the backward transform into the time and space domain is achieved by replacing ω by $i\frac{\partial}{\partial t}$ and l by $i\frac{\partial}{\partial y}$ yielding

$$
L_{1d}^{in}\frac{\partial q'}{\partial t} + \left.\frac{\partial L^{in}}{\partial \lambda}\right|_{\lambda=0}\frac{\partial q'}{\partial y} = f\left(L_{1D}^{out}\frac{\partial q'}{\partial y}\right). \tag{3.60}
$$

This differential equation can be solved along the boundary surface with an appropriate numerical scheme and the outgoing characteristics on the right-hand side need to be extrapolated from the interior. The detailed right hand side term and the solution algorithm applied in TRACE are presented by Ashcroft & Schulz (2004). The adherence of averaged boundary quantities to user specified values is again accomplished in a manner consistent with the spectral, two-dimensional and the characteristic, one-dimensional NRBC.

Giles shows that his original formulation may become ill-posed at inflows and, hence, he proposes giving up the condition for perfect decoupling of acoustic modes and thereby accepting a certain amount of reflections. The coupling term is minimized under the constraint of the boundary condition being well-posed.

Due to the approach of expressing the left eigenvector matrix by a Taylor series expansion in λ, this boundary conditions is only perfectly non-reflecting to planar waves passing orthogonally through the boundary. In general, the boundary condition becomes more reflective with increasing λ. Accordingly, flows with large circumferential wavenumbers and flows that are dominated by low frequency waves can induce spurious reflections at the boundary.

3.3.3 Steady, two-dimensional NRBC

Giles also introduces a derivative of the spectral NRBC for steady state computations. In fact, the modal decomposition for the time-averaged flow with arbitrary wavenumbers $L_{(0,l)}$ can be used in a straightforward fashion as a steady boundary condition if the modal decomposition is applied to the steady state solution of the latest pseudo-time step instead of to the zeroth harmonic of the unsteady boundary flow field. Therefore, the spectral NRBC presented in this work, when used in steady state simulations, is inherently consistent with the steady NRBC presented by Giles (1988) in terms of physics. However, Giles (1991) proposes two aspects that simplify the implementation of the NRBC for steady state computations.

Firstly, an alternative inflow boundary condition is presented to reduce the number of non-local operations and possible second-order non-uniformities in inflow stagnation enthalpy and entropy which both are assumed to be uniform in pitch-wise direction. Rather than performing the necessary Fourier transform based on primitive variables, Giles considers characteristic variables according to Equation (3.57). Note that we will also rewrite the boundary condition (Eq. (3.54)) in terms of characteristic variables in the implementation of the spectral, unsteady NRBC (as detailed in Section 3.4), but for other reasons. One simplification of Giles' steady NRBC is that the incoming modes can be written as functions of the characteristic variable associated with upstream acoustic waves c_4 only and therefore only one scalar quantity needs to be Fourier transformed at inlet boundaries.

Furthermore, the non-local conditions for entropy and for the downstream acoustic wave are replaced by a local condition that is not subject to possible second-order effects, which come with the linearization and modal decomposition approach. Instead of setting the associated modal amplitudes to zero, Giles directly suppresses any deviation from the circumferentially averaged entropy and stagnation enthalpy at every position along the boundary rather than in the wavenumber space. This guarantees uniform distributions while the modal approach may produce second-order effects. However, the author of this thesis has observed such uniformities so far only

in the presence of shocks that impinge on the inflow boundary. Hence, second-order non-uniformities appear acceptable regarding that the assumption of uniform entropy across an impinging shock is physically not sound. In lack of a better, substitute condition, this assumption is still maintained, but it appears debatable if mild deviations from it are detrimental in any way.

Secondly, Giles utilizes the fact that in steady flows, the acoustic modes are cut-on if and only if the flow is supersonic (but still subsonic in boundary-normal direction). In that case, the acoustic modes constitute Mach waves with strictly confined regions of influence. Shocks are usually presented by superposition of a number of such modes. On the other hand, in subsonic flows, acoustic modes describe the (much smoother) steady state potential flow field with an infinite region of influence due to the elliptic nature of subsonic steady state flows.

For this reason, the modal decomposition in steady, supersonic flows can be formulated in a purely local fashion while a non-local condition is needed for subsonic flows. This implies that the spatial Fourier transform is not necessary for supersonic, steady flows.

The control of mean boundary values is similar to the unsteady NRBC variants apart from the fact that temporal averaging is not meaningful in steady state simulations and, thus, only pitch-wise mean quantities are driven towards user specified values (cf. Section 3.4.4).

3.4 Implementation into time domain solver

This section deals with the implementation of spectral NRBC, as presented in Section 3.2, into a finite volume, unsteady, time domain URANS solver with dual time stepping. It addresses the topics arising from the temporally and spatially non-local nature of the spectral NRBC when applied to time marching simulations, which requires a proper specification of boundary states at any position of the boundary surface at any discrete time step. Several aspects greatly improve the robustness and convergence behaviour of the presented implementation as opposed to a former ad-hoc incorporation of spectral NRBCs from DLR's harmonic balance solver (cf. Kersken *et al.* (2014); Schlüß *et al.* (2016)). Together, these details yield an implementation, that provides true utility of the spectral NRBC in time domain simulations for real world research and design tasks.

We will discuss the implications of dual time stepping for a robust and efficient NRBC implementation. While the boundary condition must of course be applied at each pseudo-time iteration, some of its steps must be carried out only once per physical time step and with respect to the temporal dynamics of the system at hand.

Secondly, a simple one-dimensional, characteristic boundary condition (see Section 3.3.1) is used as a basic framework since these boundary conditions are well-posed and known to be very robust (cf. Giles (1988)). This is described in Sections 3.4.3 and 3.4.6.

Thirdly, we will discriminate between time-local, i.e. instantaneous, circumferential averages and quantities that are averaged in both space and time. We will take advantage of the fact that the difference between those is equivalent to the superposition of each boundary-normal wave ($l = 0$) (see Section 3.4.5).

In this work, the spectral NRBCs have been implemented into DLR's in-house turbomachinery CFD tool TRACE. TRACE offers a wide range of modelling approaches as well as numerical methods for both structured and unstructured grids (see Becker *et al.*, 2010, and references therein). Conventional steady state RANS and time marching URANS methods (see e.g. Ashcroft *et al.*, 2012; Geiser *et al.*, 2019) are available as well as reduced-order frequency domain approaches such as a time-linearized (see e.g. Kersken *et al.*, 2012; Frey *et al.*, 2012) or a nonlinear harmonic balance solver (see e.g. Frey *et al.*, 2014, 2015). To close the (U)RANS equations, TRACE covers a variety of turbulence (see e.g. Franke *et al.*, 2010; Morsbach, 2016) and transition models (see e.g. Kozulovic, 2007; Marciniak, 2016; Kügeler *et al.*, 2018). Beyond (U)RANS, recent developments also strive for turbulence resolving simulations of turbomachinery flows based on either conventional second order finite volume (see e.g Morsbach & Bergmann, 2020) or discontinuous Galerkin methods (see e.g. Bergmann *et al.*, 2018, 2020). However, turbulence resolving simulations are outside the intended scope of applications of the spectral NRBCs presented in this work.

In the context of boundary condition methods, we seek the *correct* state at faces of exposed boundary cells. This state can be regarded as the output of a particular boundary condition method, e.g. a simple reflective boundary condition, a characteristic NRBC or, in this case, the spectral, two-dimensional NRBC. The following subsections describe the calculation of this local face state. To feed the finite volume solver with a consistent flux across the boundary cell face, this face state needs to be extrapolated to the ghost cell(s) appropriately, but independently of the actual boundary condition method, as discussed in Section 3.1. That means, while the definition of a boundary condition is a piece of physical modelling, the subsequent extrapolation is a purely

numerical tool needed to provide the underlying finite volume method with suitable boundary fluxes.

3.4.1 Transient calculation of temporal Fourier coefficients

One fundamental difference between unsteady, time domain methods and frequency domain methods, where spectral NRBCs can be regarded as established state-of-the-art turbomachinery boundary conditions, is that the latter are per se non-local in time. Here, the unsteady flow field is considered in terms of Fourier coefficients of one or numerous predominant harmonics. This inherently spectral representation of the flow serves as direct input for the modal decomposition (Eq. (3.54)) and, hence, for the suppression of waves entering the computational domain. In contrast, in time marching simulations, we have to determine the temporal Fourier coefficients of the unsteady flow in a transient manner.

For this purpose, it is useful to revisit a concept which has been proposed in the context of unsteady simulations of periodic turbomachinery flows using computational domains that include only one blade passage (or a heavily reduced number of blades). If the unsteady flow is characterized by temporally and circumferentially periodic phenomena, the periodicity condition at pitch-wise boundaries can be extended such that it allows for given inter-blade phase angles. The idea is to not couple the periodic boundaries directly by exchanging their instantaneous flow states, but rather describe the boundary flows in terms of harmonic modes. The periodic boundary condition then ensures, that the flow states at either side of the domain are constructed using the same Fourier coefficients but with respect to a given phase shift. Such phase-shifted (or often referred to as phase-lagged) periodic boundary conditions have been introduced by Erdos *et al.* (1977), who store the time history at periodic boundaries to exchange phase-shifted states. However, this procedure is quite memory intensive and, thus, He (1990, 1992) suggests to describe the boundary flow with a limited number of Fourier harmonics. He describes an algorithm to update these Fourier coefficients at every time step so that storing the entire time history of the last period is not necessary. This method is called shape correction in contrast to Erdos' direct store method. In the present work, a very similar algorithm proposed by Gerolymos *et al.* (2002) (and then implemented in TRACE by Schnell, 2004) is applied.

If the sought solution is periodic in time, the Fourier coefficient of the k-th harmonic $\hat{q}_k$ must converge to a constant value. This means, the discrete integral over one period, corresponding to the fundamental frequency ω, using N sampling points, i.e. time steps, is independent of the starting point. For example, the Fourier coefficient $\hat{q}_k^n$, evaluated at time step n and with $t_n = \frac{n\,2\pi}{\omega N}$, reads

$$\hat{q}_k^n = \frac{1}{N} \sum_{i=n-N+1}^{n} q^i e^{-ik\omega t_i}.$$
(3.61)

Likewise, we write $\hat{q}_k^{n-1}$, evaluated at time step $n-1$,

$$\hat{q}_k^{n-1} = \frac{1}{N} \sum_{i=n-N}^{n-1} q^i e^{-ik\omega t_i}.$$
(3.62)

With period N, and hence

$$e^{-ik\omega t_n} = e^{-ik\omega t_{n-N}},$$
(3.63)

we expect:

$$\hat{q}_k^n - \hat{q}_k^{n-1} = \frac{1}{N} \left(q^n - q^{n-N} \right) e^{-ik\omega t_n} \to 0. \tag{3.64}$$

Since we would like to avoid storing the history of q, we approximate q^{n-N} by reconstructing it from the latest set of Fourier coefficients using again Equation (3.63):

$$q^{n-N} \approx q^* = \mathrm{Re} \sum_k \hat{q}_k^{n-1} e^{ik\omega t_n} \tag{3.65}$$

So, we can understand the right-hand side of Equation (3.64) as a residual to an iteration scheme for $\hat{q}_k$ and write:

$$\hat{q}_k^n = \hat{q}_k^{n-1} + \frac{1}{N} \left(q^n - q^* \right) e^{-ik\omega t_n} \tag{3.66}$$

Note that in a dual time-stepping solver, time levels n refer to physical time and not to pseudo-time. Therefore, the update of temporal Fourier coefficients (Eq. (3.66)) should be performed once at the end of any pseudo-time iteration loop.

In order to stabilize the phase-lag method, Schnell (2004) reports that this iteration scheme needs to be relaxed. Additionally, the temporal development of Fourier coefficients requires filtering out numerical, long-wave oscillations to achieve reasonable robustness. However, in the context of spectral NRBC, Equation (3.66) is applied directly without further modification. In fact, such long wave oscillations or other robustness issues have not been observed by the author of the present work. The reason for that might be twofold.

On the one hand, in the context of spectral NRBCs, the Fourier coefficients are used as an input to the modal decomposition yielding ideal boundary states, towards which the actual, current boundary state is driven with appropriate relaxation (as discussed later). In contrast, the phase-corrected state is directly imposed at phase-lagged periodic boundaries.

On the other hand, the spectral boundary condition suppresses incoming perturbations by prescribing bounded incoming characteristics (also discussed later in this section) whereas phase-lagged periodic boundaries transmit any kind of physical and numerical oscillations by coupling two boundaries of the computational domain, which could generate some sort of feedback mechanism.

The spectral NRBCs are implemented such that either the full spectrum from the base frequency to the highest possible harmonics according to the Nyquist criterion is considered or only a predefined set of relevant harmonics if these can be estimated a priori. The former option requires no further user input, but might become expensive in terms of computational effort and memory for very large simulations such as full wheel simulations of realistic turbomachinery components with adverse blade counts. If relevant frequencies can be identified beforehand (e.g. all blade interaction and scatter frequencies and some of their higher harmonics), the computational costs of the spectral NRBC is comparable to other (local) boundary conditions and, thus, the impact on overall computational costs is negligible even for large setups. This is investigated in detail in a master's thesis by Sivel (2018), supervised by the author of this work. In contrast to frequency domain simulations, where one tries to strongly limit the set of considered frequencies in order to fully exploit the efficiency of the frequency domain method, the selection of harmonics to be considered in the spectral NRBC can be comparatively generous. In the author's experience, the spectral NRBCs do not significantly increase

the computational effort per time step compared to simpler boundary conditions if any possible blade interaction frequency and up to ten harmonics thereof are taken into account. In single passage simulations with phase-lagged periodic boundaries, the base frequency is usually resolved with fewer time steps compared to large multi passage simulations. Therefore, an a priori selection of harmonics is not necessary in terms of computational costs. If not stated otherwise, in this work, ten harmonics of every blade interaction frequency are taken into account in multi passage simulations with truly periodic boundaries and the full spectrum up to the Nyquist frequency is used whenever phase-lagged boundaries are applied.

3.4.2   Band concept and circumferential Fourier transform

Recall from Chapter 3.2 that the spectral NRBCs presented in this work are not only non-local in time but also in space as they are derived from the two-dimensional Euler equations applied to virtual, rotationally symmetrical stream surfaces. The intersection curve with the boundary surface is a segment of a circle along which the boundary condition is applied, disregarding coupling of such stream surfaces. To obtain modal amplitudes for the application of the spectral boundary condition (Eq. (3.54)), the spatial Fourier transform of the space-local, temporal Fourier coefficients is performed in circumferential direction.
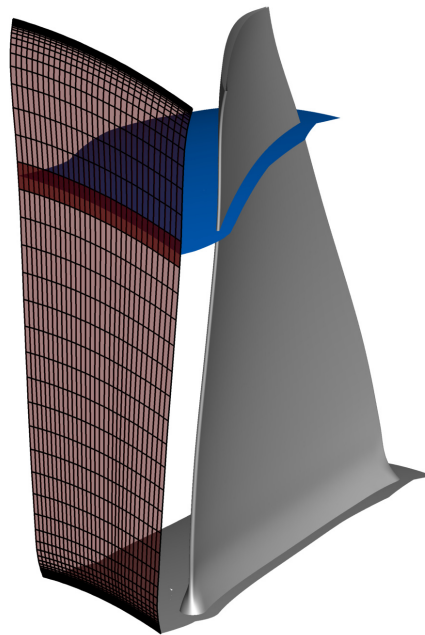
Figure 3.2: Illustration of the two-dimensional NRBC applied to three-dimensional flow. One band (dark red) is depicted as the intersection of the boundary mesh (light red) and a virtual stream surface (blue).

Therefore, it is necessary that the computational mesh is designed such that all boundary cell faces can be grouped according to their radial position into so-called bands as depicted in Figure 3.2. If the centres of faces along such a band are aligned at constant radial position, a Fourier transform along this band will yield modal amplitudes with associated circumferential wavenumbers. In the present work, only structured meshes are considered as these usually fulfil this condition for rotationally symmetrical configurations which are typically considered when dealing with turbomachinery flows.

However, unstructured meshes can also be used if inflow and outflow boundaries are discretized accordingly.

The circumferential Fourier transform and its inverse is performed employing an external library (see Keiner *et al.*, 2009). In contrast to a common DFT or FFT, this library supports non-equidistant sampling points which is important to allow for variable boundary cell sizes of the computational mesh. The library still offers computational costs that are element of $\mathcal{O}(n \log(n))$, which is also true for an FFT, instead of $\mathcal{O}(n^2)$, which is the case for a DFT.

The wavenumber spectrum is given by

$$l_j = \frac{N_\vartheta}{r} \left(j + \frac{k\sigma}{2\pi} \right) \text{ with } j \in \mathbb{Z} \tag{3.67}$$

where N_ϑ is the number of blades in single passage simulations or, more generally for arbitrary duct segments or multi passage domains of angular pitch $\Delta\vartheta$, $N_\vartheta = \frac{2\pi}{\Delta\vartheta}$. Note that the inter-blade phase angle (or more generally, the inter-segment phase angle) σ is scaled with the temporal harmonic index k. The limits of the wavenumber spectrum are determined using the Nyquist criterion based on the largest circumferential spacing of two neighbouring face centres

To implement non-local boundary conditions into a contemporary CFD solver, that exploits distributed memory parallelization based on multi block topologies, further steps must be taken. In TRACE (and many other CFD tools), this concept is realized by means of the MPI standard and respective libraries (see Message Passing Interface Forum, 2005). In very brief, the (simplified) concept works as follows: The computational domain is divided into subdomains, so-called blocks, and the system of conservation equations is solved in each of these blocks separately. The blocks with their respective data are distributed among several or many processes. Adjacent blocks need to exchange flow states at their interfaces. However, one boundary surface, in general, covers several blocks which may reside on different processes.

Thus, additional communication between processes is required for the implementation of non-local NRBCs. The local boundary states are gathered and redistributed to a subset of processes such that each participating process receives the data it needs to perform the non-local operations of the boundary condition for one or more bands. The bands (with the associated collected data and workload) are distributed among the participating processes as evenly as possible. Subsequently, the face-local boundary states are sent back to the processes, that own the respective, original block data, and the ghost cell extrapolation is performed on block level.

Also, the calculation of spatially averaged quantities involves further communication. Here, MPI provides so-called reduce operations that facilitate the calculation of integrals over split domains.

3.4.3 Characteristics-based approach and one-dimensional boundary condition

The aim of the approach presented in this section, is to capitalize on the fact that well-posed initial-boundary value problems can be formulated using bounded, incoming, boundary-normal characteristics (see Kreiss (1970); Higdon (1986*b*)). Hence, it appears promising that we can preserve the well-known robustness of the one-dimensional, characteristics-based NRBC by modifying this boundary condition appropriately Let

us recall the definition of one-dimensional characteristics c' (Eq. (3.57)) and the respective forward and backward transform L_{1D} and R_{1D} (Eq. (3.56)). Rather than prescribing vanishing incoming characteristics ($c'^{in} = L_{1D}^{in} q' = 0$), a right-hand side is sought such that the spectral, two-dimensional boundary condition (Eq. (3.54)) is fulfilled.

For this purpose, the local boundary flow state can be decomposed into its mean state $\overline{q}$ and a perturbation q' where the perturbation part is constructed in terms of outgoing and incoming characteristics:

$$q = \overline{q} + q' = \overline{q} + \left(R_{1D}^{in} c'^{in} + R_{1D}^{out} c'^{out} \right) \tag{3.68}$$

The outgoing characteristics can be extrapolated from the interior of the computational domain, i.e. the boundary-adjacent cells of the computational mesh.

Recalling Section 3.3.1, we see that with vanishing incoming part we obtain the local, characteristic, one-dimensional NRBC directly.

However, we can instead determine finite target values for these incoming characteristics from the spectral, two-dimensional NRBC theory. Note that the characteristic transformation matrices R_{1D} and L_{1D} depend purely on the mean state, but not on local or spectral quantities, in particular not on angular frequency ω and wavenumbers k and l. Therefore, we can also apply the characteristic transformation in the spectral domain.

$$\hat{c}_{(\omega,l)} = L_{1D} \, \hat{q}_{(\omega,l)} \tag{3.69}$$

Thus, we formulate a boundary state according to Equation (3.68) with incoming and outgoing characteristic variables also in the spectral domain and rewrite the non-reflecting boundary condition (Eq. (3.54)):

$$L_{(\omega,l)}^{in}\hat{q}_{(\omega,l)} = L_{(\omega,l)}^{in} \left(R_{1D}^{in} \, \hat{c}_{(\omega,l),target}^{in} + R_{1D}^{out} \, \hat{c}_{(\omega,l)}^{out} \right) = 0. \tag{3.70}$$

Extrapolating the outgoing characteristics $\hat{c}_{(\omega,l)}^{out}$ and solving Eq. (3.70) for the incoming target characteristics $\hat{c}_{(\omega,l),target}^{in}$ yields

$$\hat{c}_{target,(\omega,l)}^{in} = - \left(L_{(\omega,l)}^{in} R_{1D}^{in} \right)^{-1} L_{(\omega,l)}^{in} R_{1D}^{out} \, \hat{c}_{(\omega,l)}^{out}. \tag{3.71}$$

The above equation provides the ideal incoming characteristics of each mode in the discrete, two-dimensional spectrum of frequencies and circumferential wavenumbers. In order to determine the ideal flow state to avoid incoming perturbations, we need to reconstruct the time- and space-local incoming target characteristics from these modal contributions. This will be discussed in Section 3.4.6.

Note, however, that modes that are not resolved with Fourier modes (see Section 3.4.1) are interpreted as modes with vanishing contribution in terms of modal target characteristics. Hence, possibly neglected modes are still captured in a one-dimensional-NRBC-like fashion by the approach at hand, i.e. the reconstruction of local, incoming target characteristics from ideal, modal contributions, because vanishing incoming characteristics satisfy the one-dimensional NRBC, see Equation (3.58).

3.4.4   Mean boundary values and compliance with specified operating conditions

The mode $\hat{q}_{(0,0)}$ is disregarded when calculating the incoming target characteristics since this mode describes the temporal and circumferential mean flow. Instead, we

are looking for the shift of mean, incoming characteristics, $\delta \overline{c^{in}}$, needed in order to meet user-specified boundary values, denoted by subscript bd. For this purpose, we introduce the residuum:

$$
\mathfrak{R} =
\begin{cases}
\begin{pmatrix}
\frac{\overline{p}}{c_v}\left(s^F - s_{bd}\right) \\
\overline{\varrho}\,\overline{a}\left(\nu_1 \cdot V^F\right) \\
\overline{\varrho}\,\overline{a}\left(\nu_2 \cdot V^F\right) \\
\overline{\varrho}(h_t^F - h_{t,bd})
\end{pmatrix}
& \text{for inflow boundaries} \\[4em]
\left(p^F - p_{bd}\right) & \text{for outflow boundaries}
\end{cases}
\tag{3.72}
$$

This residuum is driven to zero by means of one Newton-Raphson step per time step to determine $\delta \overline{c^{in}}$:

$$
\mathfrak{R} + \frac{\partial \mathfrak{R}}{\partial q^F} R_{1D}^{in} \delta \overline{c^{in}} = 0
\tag{3.73}
$$

with

$$
\frac{\partial \mathfrak{R}}{\partial q^F} =
\begin{cases}
\begin{pmatrix}
-\overline{a}^2 & 0 & 0 & 0 & 1 \\
0 & \overline{\varrho}\,\overline{a}\,\nu_{x,1} & \overline{\varrho}\,\overline{a}\,\nu_{y,1} & \overline{\varrho}\,\overline{a}\,\nu_{z,1} & 0 \\
0 & \overline{\varrho}\,\overline{a}\,\nu_{x,2} & \overline{\varrho}\,\overline{a}\,\nu_{y,2} & \overline{\varrho}\,\overline{a}\,\nu_{z,2} & 0 \\
-\frac{\gamma}{\gamma-1}\frac{\overline{p}}{\overline{\varrho}} & \overline{\varrho}\,\overline{u} & \overline{\varrho}\,\overline{v} & \overline{\varrho}\,\overline{w} & \frac{\gamma}{\gamma-1}
\end{pmatrix}
& \text{for inflow boundaries} \\[4em]
\begin{pmatrix} 0 & 0 & 0 & 0 & 1 \end{pmatrix} & \text{for outflow boundaries}
\end{cases}
\tag{3.74}
$$

The vectors $\nu_{1,2}$ are constructed as orthonormal vectors to the target flow direction using the Gram-Schmidt process. In TRACE, the target inflow direction can be specified by the user in several formats, either directly as a vector in cylindrical coordinates or based on various flow angle definitions commonly used in the turbomachinery community.

Superscript F denotes flux-averaged quantities. This averaging technique and why it is used will be discussed later in this section.

The definition of the residual is not unique and many other formulations are possible. The present residual is very similar to the one proposed by Giles (1991) apart from the more general criterion to specify the inflow direction and a different scaling by (area-averaged) mean quantities.

In turbomachinery analysis, inlet conditions are typically specified in terms of stagnation temperature and stagnation pressure. Since the state of an ideal gas has two degrees of freedom (at macroscopic level), it is straightforward to determine the target boundary values of entropy and stagnation enthalpy

$$
s = c_p \ln\left(\frac{T_t}{T_{ref}}\right) - R \ln\left(\frac{p_t}{p_{ref}}\right)
\tag{3.75}
$$

$$
h_t = c_p T_t
\tag{3.76}
$$

with reference pressure p_{ref} and temperature T_{ref}. These reference values can be chosen arbitrarily as they result in a constant entropy shift and thus cancel out in the

entropy residual condition. In a non-dimensionalized implementation of a flow solver, they can be omitted, but in this notation they are necessary just because the argument of the logarithm needs to be dimensionless.

The mix of area-averaged and flux-averaged quantities in the definition of the residual may seem odd at first glance. The reason is that the actual criteria, i.e. vanishing entropy and enthalpy deviations as well as the alignment of the velocity vector with the given flow direction, are based on flux-averaged values and have the respective dimension while area-averaged quantities are used to scale every component of the residual vector such that they have dimension pressure. Thus, the Newton-Raphson step is performed with respect to the flux-averaged quantities only and the Jacobian consists of area-averaged quantities alone.

At inflow and outflow boundaries, the boundary values can either be specified by spanwise distributions or by global parameters. In the latter case, the inflow boundary values are imposed at each band independently (see Section 3.4.2) rather than on average. If a single value for static pressure is used at an outlet instead of a spanwise distribution, the pressure at each band is adjusted based on the flow solution with respect to the radial equilibrium condition

$$\frac{\partial p}{\partial r} = \overline{\varrho}\frac{\overline{v}_{abs}^2}{r} \tag{3.77}$$

with $\overline{v}_{abs}$ being the mean circumferential velocity in the absolute frame of reference. The user-defined reference pressure is then imposed at a spanwise position of choice. This can be either at the hub or at the tip or at midspan.

The spectral NRBC presented in this work can also be used as a NRBC for steady flow simulations, equivalent to the steady NRBC described in Section 3.3.3. An application to the mixing plane approach (see Giles, 1991) is readily available if the above residual is replaced by the difference of flux-averaged states (expressed in primitive variables). Then, the 5x5 residual Jacobian is simply the identity matrix I and the outgoing components of the five-dimensional, characteristic solution vector are subsequently removed, yielding $\delta\overline{c^{in}}$. Thus, the correct propagation direction of information is inherently ensured.

Closely linked to the issue of specifying boundary values and imposing them on the boundary flow field is the question how a temporally and spatially varying flow field can be adequately represented by an equivalent and somehow averaged flow state. Although it is often presumed in turbomachinery design that the latter is always guaranteed, there is no trivial answer to this question. For the interested reader, Cumpsty & Horlock (2006) provide a highly recommendable overview. They conclude that there is no such thing as a universal averaging method and choosing a suitable method is not a matter of preference, but the correct method depends on the underlying engineering problem or design task.

In the context of boundary conditions, the so-called flux-averaging method (also known as mixed-out averaging) is used in this work due to consistency and conservation requirements. This concept traces back to the work of Amecke (1967) with respect to two-dimensional cascade flows and shortly afterwards Dzung (1971) for three-dimensional turbomachinery flows (both in German language). A comprehensive English-language introduction and review is presented in a report by Pianko & Wazelt (1983). It should be noted, that for swirling, three-dimensional flows in annular ducts, as they are typically found in turbomachinery, further consideration is needed as shown by Prasad (2005). However, the averaging process is performed in a quasi-two-dimensional fash-

ion along individual bands for the boundary condition (see Section 3.4.2) which permits the use of the original flux averaging method.

Unlike simple weighted averaging techniques, such as area or mass flow weighted averaging, the flux averaging process seeks a homogeneous flow state that yields flux integrals for mass, (angular) momentum and energy on a given surface, in our case the band at the respective radius, that are equal to the fluxes integral of the inhomogeneous and time-varying flow field. With the prerequisites from Chapter 3.2 (i.e. $0 < \overline{u} < \overline{a}$), we can define the flux-averaged state of a band as the inverse of the boundary-normal flux function applied to the time-mean, area-averaged flux density on a band:

$$q^F = F^{-1} \left(\frac{1}{T \, |A_{band}|} \int\limits_{T} \int\limits_{A_{band}} F(q) \, dA \, dt \right) \tag{3.78}$$

In periodic turbomachinery flows, the time interval T refers to the period of the fundamental frequency that is also used in the temporal Fourier analysis.

As flux-averaging is the only method that conserves mass, momentum and energy across an interface, it is mandatory for mixing planes. At inlets and outlets, the correct choice is not necessarily so strict (although the subsequent analysis of results from a simulation demands more rigour with respect to the nature of the analysis as elaborated by Cumpsty & Horlock (2006)). For instance, consistency to reference data from experiments or other (pre)design tools, where flux-averaged data are not available, may be important. Thus, the formulation of the residual vector in TRACE is not rigidly limited to controlling the mean flow with respect to flux-averaged boundary values and also area or mass flow averaging can be chosen by the user. Otherwise, one should stick to flux-averaging for the following reasons.

Firstly, the ideal NRBC represents an artificial boundary and therefore mimics the interaction of the computational domain with the infinite surroundings. Thus, when applying NRBC, the flow solution is independent of the exact position of the boundary (neglecting increased or decreased end wall losses when shifting the inlet and outlet boundary as well as aerodynamic and aeroacoustic interactions with potentially converging or diverging annular ducts). For this purpose, a mixed-out average is the correct reference state.

Secondly, unsteady flow simulations, particularly in the context of aeroelasticity, are often performed on subdomains of more extended steady state computations. For example, in the flutter or forced response analysis of single blade rows or stages, these rows, together with the corresponding radial distributions of boundary values, are usually extracted from steady state simulations of the entire component at a given operating point. Hence, former mixing planes become inlet and outlet boundaries and, for consistency, flux-averaged boundary values should also be used in the unsteady simulation.

3.4.5 Time-local procedure for quasi-1D waves

Whenever truly periodic boundaries are used, e.g. in multi-passage simulations in contrast to single passage simulations using the phase lag approach and non-zero IBPA, the circumferential wavenumber $l = 0$ exists in the discrete wavenumber spectrum (see Section 3.4.2). In such cases, we can exploit the following simplification.

All modes with zero circumferential wavenumber are excluded from the spectral approach disregarding their temporal harmonic index. The reason is that modes of circumferential wavenumber zero, i.e. plane waves propagating normal to the boundary surface, lead to temporal fluctuations in instantaneous, circumferential averages. This can interfere with the update of mean characteristics to meet given boundary values as long as the temporal Fourier coefficients and temporal averages are not fully converged. Instead of regarding those modes within the spectral NRBC approach, we extrapolate the instantaneous, circumferentially averaged outgoing characteristics

$$\widetilde{c_i^{out}} = L_{1D}^{out} \left(\widetilde{q_i} - \overline{q_i} \right) \tag{3.79}$$

with $\widetilde{q}$ being the instantaneous, area-averaged state and subscript i denoting states in the boundary adjacent, inner cell layer.

Thus, $\widetilde{c_i^{out}}$, too, represents plane waves running orthogonally to the boundary. Their respective contribution to target incoming characteristics is zero. For periodically converged flows, $\widetilde{c_i^{out}}$ is equivalent to the outward propagating wave reconstructed from all modes $\hat{q}_{(\omega,0)}$. However, the above procedure does not depend on temporal Fourier coefficients. Therefore, the extrapolation of circumferentially symmetric, outgoing waves can be carried out locally in time allowing this strategy to properly capture transient plane wave perturbations at early stages of the simulation, thereby facilitating convergence.

3.4.6 Reconstruction of the local, instantaneous boundary flow field

The final step of the non-reflecting boundary condition is to construct the local face states at the current time step of the time marching simulation. For this purpose, the individual terms from Sections 3.4.3-3.4.5 are compiled along with the mean state.

The instantaneous, face-wise, incoming target characteristics need to be determined from the spectral target incoming characteristics (Eq. (3.71)) by means of a spatial and temporal inverse Fourier transform.

$$c_{target}^{in}(t,y) = \sum_k \sum_j \mathrm{Re} \left(\hat{c}_{target,(\omega_k,l_j)}^{in} \, e^{i(l_j y + \omega_k t)} \right) \text{ with } \omega_k = k\omega \tag{3.80}$$

Since the temporal Fourier coefficients of the boundary flow field are updated only once per physical time step, the target characteristics also need to be evaluated only once per time step. However, in order to ensure that the target values are met at the end of a pseudo-time iteration loop, the local, incoming characteristics at a face must be updated at each pseudo-time step i of a physical time step n:

$$\left(c_f^{in} \right)^{n,i} = (1 - \varphi) \left(c_f^{in} \right)^{n,i-1} + \varphi \left(c_{target}^{in} \right)^n \tag{3.81}$$

Some relaxation is helpful in order to preserve the good robustness of the underlying characteristics-based boundary condition formulation in a pseudo-time solver as suggested by Giles (1988). On the other hand, the relaxation factor φ must be sufficiently large to achieve convergence in pseudo-time within a limited number of iterations. In this work, the relaxation factor $\varphi = 0.85$ is chosen.

On the other hand, the mean characteristics update (Eq. (3.73)) must be imposed with particular deliberation regarding physical time and suitable relaxation. The resulting

shift should be applied only once per physical time step for two reasons. First, convergence of the inner iteration loop would otherwise be impossible because the controlled boundary value, due to its nature as a time-averaged quantity, cannot reach a given value in a single physical time step. Second, stability and convergence properties of the control problem of the dynamic system should not depend on the number of inner iterations per time step as the latter is just a numerical solution method while only physical time stepping determines the temporal evolution of the flow field.

Since the temporal development of time-averaged quantities is lagged depending on the fundamental frequency, and thus the period (see Eq. (3.78)), the dynamic properties, e.g. the stability limit for the control of boundary values, is also governed by the underlying fundamental frequency. Therefore, the prescribed rate of change of the boundary flow per time step must be scaled with respect to the number of time steps per period, so that the system behaviour is tuned to the fundamental frequency rather than to the individual time step.

Hence, a prefactor of $\frac{\psi \mathcal{N}}{N}$ is introduced for the control of mean, incoming characteristics $\delta \overline{c^{in}}$. The free parameter ψ can be increased by the user in order to expedite convergence at the expense of robustness or vice versa. Although faster convergence is often possible with larger values, a value of $\psi = 5$ provides reliable convergence in the author's experience. This value is therefore the default value in TRACE and is used throughout this thesis.

To accelerate multi-passage simulations, where the dominant blade interaction frequencies are much greater than the underlying base frequency, e.g. the frequency associated with the shaft's rotational speed in full wheel simulations, the number of modelled blades in the mesh of the neighbouring blade row is also included in the scaling factor. For full wheel simulations, the factor $\mathcal{N}$ is equal to the number of blades in the neighbouring blade row of the real world machine, while for less-than-360° models $\mathcal{N}$ is scaled according to the circumferential extent of the numerical domain. For example, $\mathcal{N}$ equals one in single passage computations.

From the author's point of view, a more sophisticated control law for the boundary values, rather than a simple correction proportional to the time-averaged deviation, could potentially provide a significant speed-up in the future, in particular for large multi-passage simulations with small base frequencies and therefore big lag in the evolution of averaged quantities.

When constructing local face states by means of incoming and outgoing characteristics, the outgoing characteristics are extrapolated from the interior layer of cells. Therefore, unlike incoming characteristics, outgoing characteristics must not undergo numerical relaxation in order to correctly capture their physical propagation.

As the extrapolation of mean, outgoing characteristics (see Section 3.4.5) is only applicable when using non-phase-shifted periodic boundary conditions, two cases need to be considered for the extrapolation of local outgoing characteristics from the interior:

$$c_i^{out} = \begin{cases} \widetilde{c_i^{out}} + L_{1D}^{out} (q_i - \widetilde{q_i}) & \text{for truly periodic boundaries} \\ L_{1D}^{out} (q_i - \overline{q_i}) & \text{for phase-shifted periodic boundaries} \end{cases} \tag{3.82}$$

Finally, the instantaneous face state reads

$$q_f = \overline{q_f} + \left[R_{1D}^{in} \left(c_f^{in} + \frac{\psi \mathcal{N}}{N} \delta \overline{c^{in}} \right) + R_{1D}^{out} c^{out} \right]. \tag{3.83}$$

4 Academic validation test cases

4.1 VKI LS89 cascade

4.1.1 Test case design and numerical setup

The first validation test case is a two-dimensional, linear turbine cascade designed and investigated at von Karman Institute for Fluid Dynamics (VKI) (see Arts *et al.*, 1990; Arts & Lambert de Rouvroit, 1992). A preliminary, reduced study of this test case has been presented as a conference contribution before (see Schlüß *et al.*, 2016). However, that earlier work is based on different operating conditions which are not covered in the VKI measurement series. Furthermore, the study uses the aforementioned ad-hoc adaption of the spectral NRBC harmonic balance implementation in TRACE. This prototype showed very similar results for this test case, but for many others it suffered from convergence and robustness issues.

The test case is intended to showcase three things. First, unnatural reflections from boundaries with reflecting or partially reflecting boundary conditions are not only detrimental when studying unsteady flows, for example in aeroelasticity, but can also impair the prediction of mean flow features. Second, the different representations of the interaction of a suction-sided shock with the outlet boundary serve as a lucid visualization of physically implausible boundary conditions. Third, we observe that the flow solution is independent of the position of an artificial boundary if a non-reflecting boundary condition is employed.

The LS89 airfoil is typical of highly loaded nozzle guide vanes and a detailed description of the geometry, the test facility and the operating conditions can be found in the references above. Blade pressure and heat transfer measurements are available for a variety of Reynolds numbers, exit Mach numbers and inflow free-stream turbulence intensities. Therefore, the cascade is frequently used for code validation purposes, especially with respect to heat transfer modelling (see e.g. Gourdain *et al.*, 2010; Collado Morata *et al.*, 2012), RANS-based turbulence and transition modelling (see e.g. Langtry & Menter, 2009; Steelant & Dick, 2000) as well as the development of turbulence resolving methods and associated higher-order discretization schemes (see e.g. Segui *et al.*, 2017; Klose *et al.*, 2022).

With regards to boundary conditions, the cascade is of particular interest as a shock extends from the aft part of the suction side almost perpendicularly to the outlet boundary under transonic flow conditions and due to the large outflow angle of the airfoil. Therefore, Cosmo & Salvadori (2019) and Henninger (2019) use this test case to validate their implementations of Giles's steady NRBC and Hagstrom's higher-order approximate NRBC (see Chapter 2) respectively.

Like in the latter works, a transonic flow is considered in this study with conditions

53

designated as MUR47 by Arts and subsequent authors. A synopsis of its characteristic parameters is given in Table 4.1. With the low inflow turbulence intensity and the strong stream-wise acceleration under these conditions, Arts *et al.* (1990) observe attached, laminar flow until laminar-to-turbulent transition onset is triggered by the shock on the suction side close to the trailing edge. Accordingly, the prediction of blade pressure distributions is, in contrast to other operating conditions, primarily governed by potential flow phenomena and the boundary conditions' different reflection properties rather than turbulence and transition modelling. Therefore, this is a suitable operating point to study boundary conditions.

Table 4.1: LS89 characteristics and MUR47 operating conditions.

P/c	0.85	-
γ_{geom}	55°	-
σ_0/P	0.2597	-
$p_{t,Inlet}$	159.6	kPa
$T_{t,Inlet}$	420	K
$Ma_{is,Outlet}$	1.02	(see Eq. (4.2))
Re_{Outlet}	10^6	-
α_{circ}	0°	(axial flow)
Tu_{Inlet}	1 %	-

For this purpose three different computational domains are considered with varying axial spacing d between the in- and outflow boundary and the blade's leading and trailing edge respectively. The smallest domain is most challenging for the boundary conditions with $d/c_{ax} = 0.5$. Besides, a medium large domain ($d/c_{ax} = 1$) and a large domain ($d/c_{ax} = 3$) are examined. All computations are carried out on single blade meshes with periodic boundary conditions in pitch-wise direction. The meshes are quasi-two-dimensional with a single layer of cells and inviscid walls at the span-wise boundaries. Figure 4.1 depicts the mesh coarsened by factor two in both dimensions. The structured mesh comprises 21,016 cells in the short case and up to 36,668 cells with the longest domain. The blade wall boundary layer is discretized such that the wall-adjacent cells have a fairly fine, average wall-normal size of $y^+ = 0.3$. A grid convergence study has shown that a mesh refinement by factor 2 (i.e. about 84,000 cells in the small domain) leads to identical blade pressure distributions (not shown here).

Steady-state simulations are conducted using the spectral 2D NRBC, Giles's steady 2D NRBC and a simple, local Riemann boundary conditions (see Chapter 2.2.2) at the inflow and outflow boundary. Additionally, time-resolving simulations are performed to analyse unsteady boundary conditions, that is Giles's approximate 2D NRBC, a characteristic 1D NRBC and again the spectral 2D NRBC. As there is no external source of unsteadiness in this cascade flow, a reasonable time step size needs to be estimated. Here, this estimation is based on the outflow conditions of the steady-state flow. It is assumed that a virtual, downstream blade row of identical pitch has a pitch-wise relative velocity such that it faces axial inflow conditions in its moving frame of reference. Then, we can determine a base frequency of

$$f = \frac{\overline{v}_{Outlet}}{P} = 6,261 \text{Hz}. \tag{4.1}$$

The corresponding period is resolved with 64 time steps using an implicit, dual time-
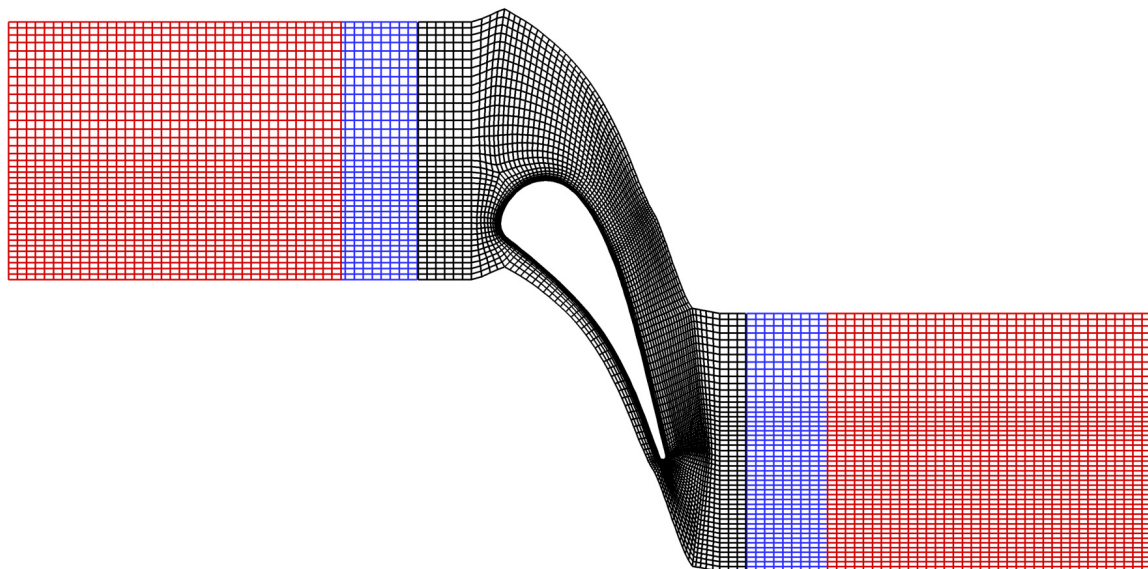
Figure 4.1: Computational mesh of VKI LS89 turbine cascade, every second mesh line depicted. Colours illustrate different axial length of the computational domain (black: $d/c_{ax} = 0.5$, blue: $d/c_{ax} = 1$, red: $d/c_{ax} = 3$).

stepping, third-order Runge-Kutta scheme (see Ashcroft *et al.*, 2013) and 20 pseudo-time iterations. Time integration is carried out over 100 periods.

However, no unsteadiness is observed in any of the time-resolving simulations and the flow converges to a stable, steady-state solution. While Segui *et al.* (2017) and Klose *et al.* (2022) find macroscopic unsteady effects in their LES (such as trailing edge vortex shedding and shock-boundary layer interaction apart from purely stochastic turbulence), it should be noted that they consider operating points with smaller pressure ratios and in some cases considerably higher inflow turbulence levels, resulting in more complex boundary layer flows (i.e. either laminar separation bubbles or bypass transition upstream of the shock).

Given that the pre-shock Mach number is moderate and no detached flow is found in the experiment under the MUR47 flow conditions, the prediction of steady-state flow appears plausible in the context of URANS-based simulations. Hence, in the absence of unsteady effects, the boundary condition analysis is focused on the prediction of steady-state flow features. Reflection properties with regard to unsteady waves are investigated in Chapters 4.2, 4.3 and 5.

All computations are performed applying Roe's upwind scheme (see Roe, 1981) extended to second-order accuracy through van Leer's MUSCL extrapolation (see van Leer, 1979) and an appropriate limiter function for convective fluxes. Viscous fluxes are computed based on gradients obtained by a central finite difference scheme in combination with Wilcox's k-ω turbulence model (see Wilcox, 1988). If not stated otherwise, these spatial discretization methods are also applied to subsequent test cases of this work.

4.1.2 Pseudo-schlieren images

In Figures 4.2 and 4.3, the magnitude of the density gradient is plotted for all computations with the short and long domain in order to mimic schlieren photography for
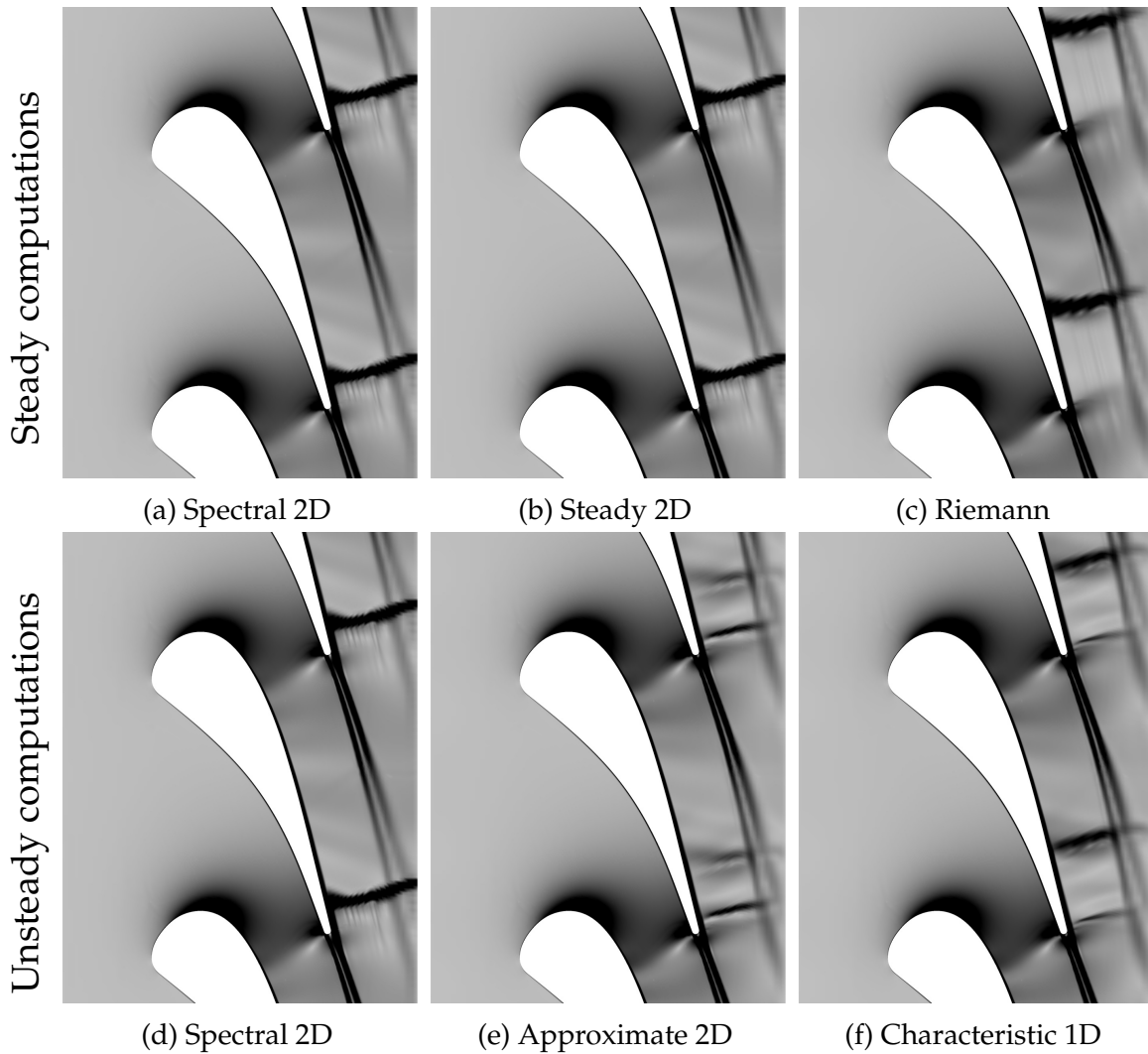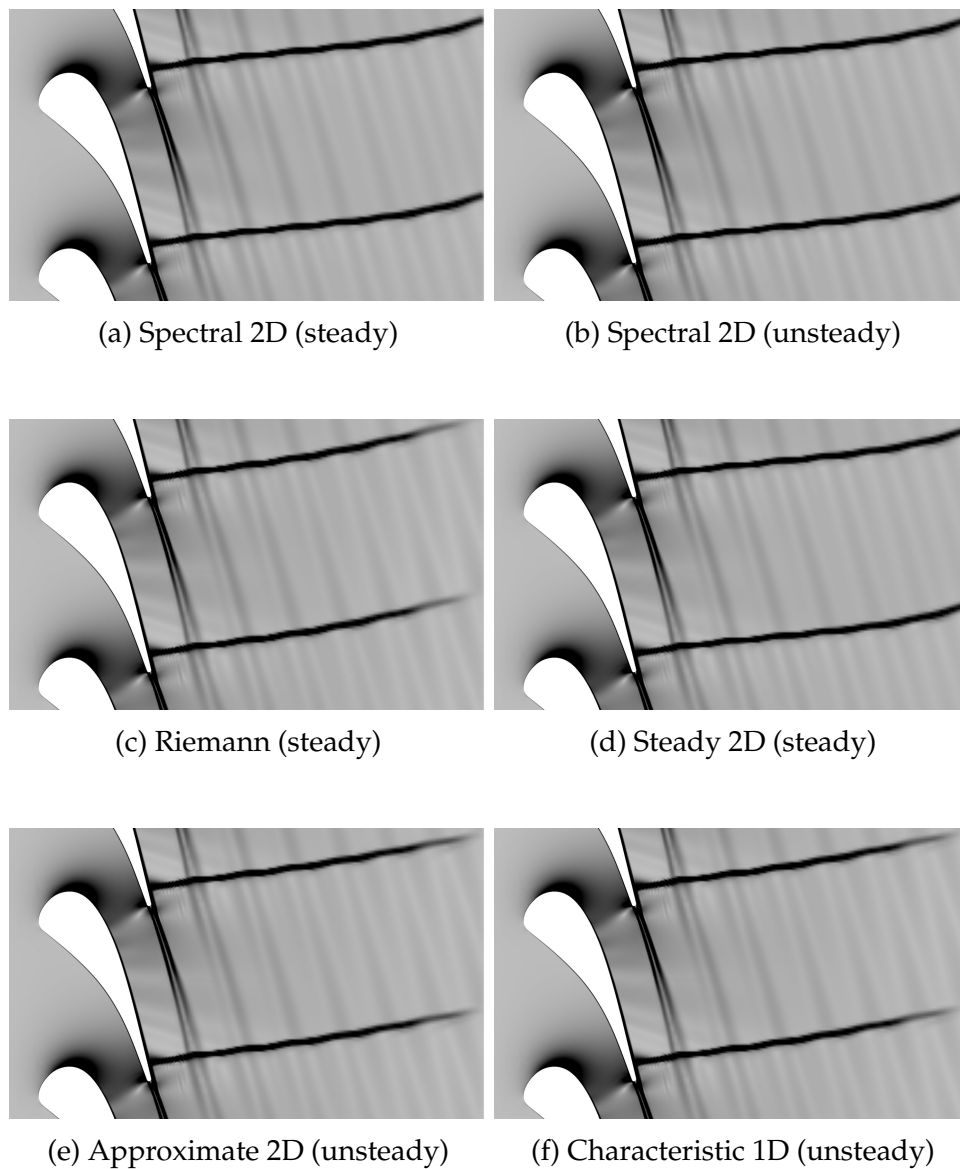
Figure 4.2: Pseudo-schlieren images obtained by plotting density gradient magnitude (black corresponds to large gradients), $d/c_{ax} = 0.5$, flow solution is duplicated in pitch-wise direction for visualization.

flow visualization. For a better overview, the mesh and flow solution is duplicated in pitch-wise direction in the depiction. The flow around the airfoil is supercritical, characterized by a shock close to suction side trailing edge that extends to the exit boundary plane. Depending on the boundary condition method in use and the distance between the exit boundary and the trailing edge, the shock representation differs significantly.

The results using the shortest computational domain ($d/c_{ax} = 0.5$) are depicted in Fig. 4.2. On the one hand, the steady computations employing the steady, two-dimensional NRBC (Fig.4.2b) coincide with both the steady-state computation using the spectral, two-dimensional NRBC (Fig.4.2a) and the unsteady computation using the spectral, two-dimensional NRBC (Fig.4.2d). These results exhibit the shock going right through the exit plane.

On the other hand, the other boundary conditions predict flow fields that differ from those mentioned above as well as among each other. While we still observe a distinct shock with the Riemann boundary conditions (Fig.4.2c), the shock is predicted further upstream. Moreover, the shock appears to be truncated in the vicinity of the boundary owing to the physically not justified constant pressure field along the boundary

imposed by the Riemann boundary condition.

Despite their ability to allow for pressure variations along the boundary surface, the approximate, two-dimensional (Fig.4.2e) and the characteristic, one-dimensional NRBC (Fig.4.2f) produce flow fields in the region in question which do not feature a distinct, single shock. Instead, increased density gradients occur in a wider area of the suction-sided trailing edge region. Two confined lines might resemble shocks, yet weaker compared to the shocks in Figs. 4.2a-4.2d. However, the analysis of blade pressure distributions in Section 4.1.3 will support that these lines of increased density gradients do not represent two definite shocks. The solutions predicted by the approximate and the characteristic NRBCs are qualitatively similar, yet not identical.

(a) Spectral 2D (steady) (b) Spectral 2D (unsteady)

(c) Riemann (steady) (d) Steady 2D (steady)

(e) Approximate 2D (unsteady) (f) Characteristic 1D (unsteady)

Figure 4.3: Pseudo-schlieren images obtained by plotting density gradient magnitude (black corresponds to large gradients), $d/c_{ax} = 3$, inflow region truncated in depiction, flow solution is duplicated in pitch-wise direction for visualization

Figure 4.3 shows corresponding flow solutions obtained from the computations with the longest computational domain ($d/c_{ax} = 3$). Here, all boundary conditions methods consistently produce a shock, coincident in shape and position with the shock predicted by the steady and the spectral two-dimensional NRBCs with the short domain.

Note that those boundary conditions which exhibit a different shock representation with the short domain still interact with the shock in close proximity to the boundary, that is, they fail to render the shock passing the boundary. However, the region of influence is limited and does not affect the flow close to the blade.

4.1.3 Blade pressure distribution
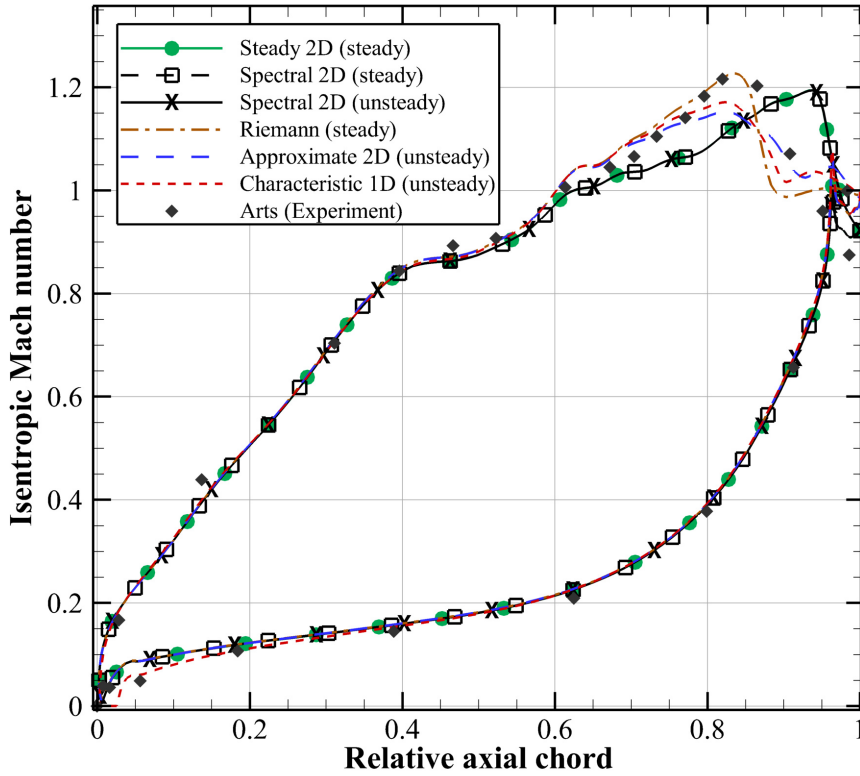
Figure 4.4: Comparison of isentropic Mach number distributions with different boundary condition methods and small axial spacing ($d/c_{ax} = 0.5$).

In the following, blade pressure distributions are analysed in order to quantitatively support the findings from the previous chapter. A common way to present blade pressure distributions is by means of the isentropic Mach number:

$$Ma_{is} = \sqrt{\frac{2}{\gamma - 1} \left[\left(\frac{p_{t,Inlet}}{p} \right)^{\frac{\gamma - 1}{\gamma}} - 1 \right]} \tag{4.2}$$

In Fig. 4.4 the isentropic Mach number distributions obtained with the short domain and different boundary conditions are compared. Additionally, experimental results from Arts *et al.* (1990) are included. The isentropic Mach number distributions of all computations show excellent agreement with each other and with the VKI measurements along the pressure side and in the front half of the suction side.

Beyond this and consistent with our observations in the previous section, the steady, two-dimensional and the spectral, two-dimensional NRBC also coincide in the rear

(a) Spectral 2D (steady)

(b) Spectral 2D (unsteady)

(c) Riemann (steady)

(d) Steady 2D (steady)

(e) Approximate 2D (unsteady)

(f) Characteristic 1D (unsteady)
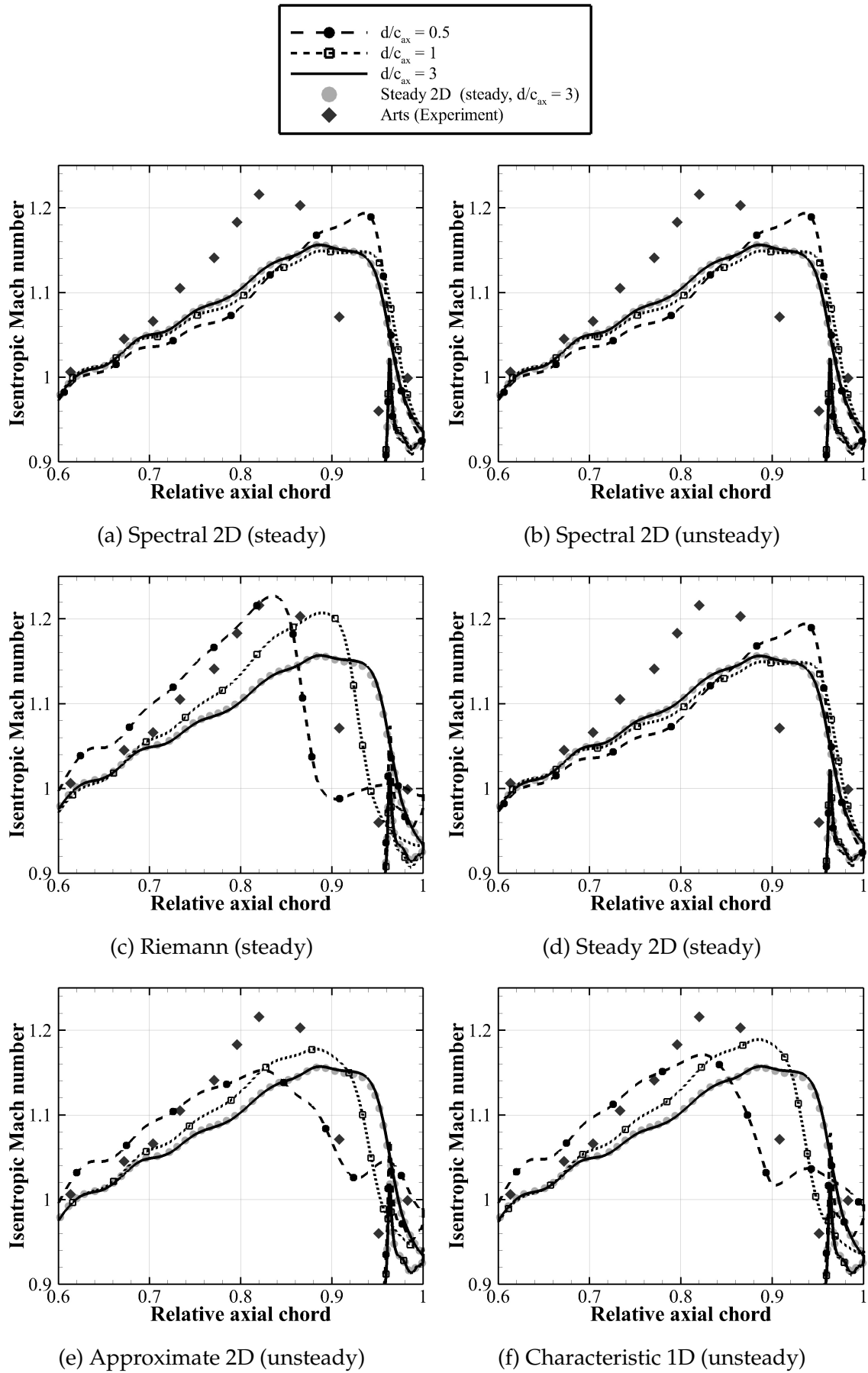
Figure 4.5: Close-up of isentropic Mach number distributions with different boundary condition methods and domains, rear part of suction side.

part of the suction side, where the shock is predicted at about 95 % relative axial span with a pre-shock Mach number of 1.2.

The Riemann boundary condition predicts the shock at about 85-90 %, just slightly in front of the position found in the experiment by Arts. The predicted pre-shock Mach number matches the the experiment ($Ma_{is} \approx 1.22$).

While the approximate, two-dimensional NRBC and the characteristic, one-dimensional NRBC exhibit the transition from supersonic to subsonic flow at roughly the same position, they do not feature a distinct shock. Instead, the flow decelerates continuously through a segment with a length of about 10 % relative axial chord. Given the fact that the flow solution is not time-averaged but constant in time, this smooth supersonic to subsonic transition is considered physically incorrect. The local Mach number maximum of the solutions using the approximate and the characteristic NRBC is about 1.7 and 1.8 respectively. However, these solutions as well as the solution obtained with the Riemann boundary condition correspond more closely to the experimental isentropic Mach number distribution in the supersonic region (from about 50 % to about 90 % relative axial chord) compared to the solutions obtained with the steady or spectral boundary conditions, which have weaker supersonic acceleration in this region.

Based on the above observations, the Riemann, the characteristic one-dimensional and the approximate two-dimensional boundary conditions seem to better reflect the flow as measured at VKI than the spectral or steady two-dimensional NRBCs do. However, the inconsistency of schlieren plots with regards to axial spacing of the former boundary conditions and the implausible drop in isentropic Mach number, from supersonic to subsonic flow, of the characteristic and approximate boundary conditions, contradict a conclusion that the results with the Riemann, characteristic or approximate boundary conditions are more accurate than the ones using the spectral or steady NRBCs.

To have a closer look at the boundary conditions' impact on the flow in the region in question, Figure 4.5 depicts the isentropic Mach number in the suction-sided rear part of the blade in more detail. It shows the variation of the isentropic Mach number distribution of each boundary condition method with different axial spacings between the blade and the boundary surface. For easier comparison among the different boundary condition methods, the results from the largest domain using the two-dimensional spectral NRBC are included in every subfigure as well as the VKI test results.

The crucial finding at this point is that the solutions obtained with all boundary condition methods converge to the same solution with increasing axial spacing. This is in line with the observations from Fig. 4.3 and indicates that this common solution is, due to minimal influence of the artificial boundary, the most accurate solution to the two-dimensional, periodic flow problem based on the (U)RANS-equations with given turbulence and transition modelling and numerical discretization.

Yet, the different boundary condition methods differ in how quickly they reach this solution. The steady and unsteady computations with the spectral, two-dimensional NRBC (Figs. 4.5a and 4.5b) and the computation with the steady, two-dimensional NRBC (Fig. 4.5d) exhibit only small deviations when the shortest domain is used. With this short domain, they overestimate the pre-shock acceleration in the very vicinity of the shock ($\sim$5 % relative axial chord) by about 0.05, but agree very closely with the solution from the large domain in all other parts of the suction side apart from the immediate pre-shock region. Already with an axial spacing of $d/c_{ax} = 1$, the solutions almost coincide with the solutions from the $d/c_{ax} = 3$ domain.

In contrast, the remaining boundary condition methods, applied to the short domain, deviate significantly from the common solutions obtained with the long domain as discussed in the first part of this section. Moreover, with the $d/c_{ax} = 1$ domain, they produce intermediate solutions which, on the one hand, also incorporate a shock when using the characteristic (Fig. 4.5f) and the approximate NRBCs (Fig. 4.5e). On the other hand, the shock position is still located upstream of the shock position found when using the long domain.

This supports the above statement, that the (partially) reflecting boundary conditions (i.e. Riemann, characteristic one-dimensional and approximate, two-dimensional) do not provide a better prediction of the cascade flow with the short mesh under these conditions. The dependence of the flow solution on the axial spacing between the blade and the boundary indicates unphysical interaction of the artificial boundary and the blade flow. The good agreement of especially the solution based on the Riemann boundary condition is coincidental and due to cancellation of errors, either from modelling and numerics or from uncertainties in the measurements.
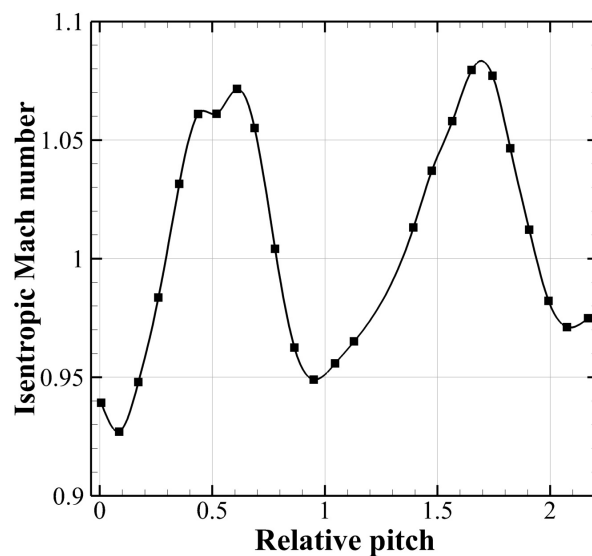
Figure 4.6: Isentropic Mach number from side wall pressure at $d/c_{ax} = 0.43$ by Arts & Lambert de Rouvroit (1992), $Ma_{is,Outlet} = 1.02$, $Re_{Outlet} = 10^6$.

In fact, other authors note similar divergence from the VKI MUR47 measurements regarding the prediction of the shock employing various types of NRBCs or sufficiently large domains. Henninger (2019), using Hagstrom's higher-order approximate NRBC implemented in TRACE, Cosmo & Salvadori (2019), with an implementation of Giles's steady two-dimensional NRBC in an unstructured solver, and Vagnoli (2016), using Numeca's Fine/Turbo as well as an OpenFOAM derivative, report predicted shock positions downstream of the VKI measurements and in good agreement with the data presented in this work.

Henninger suspects insufficient periodicity of the original cascade as a potential reason for the mismatch of idealized, two-dimensional, periodic, computational results on the one hand and the experiment (with only five blades in pitch-wise direction for instrumentation reasons) on the other hand. This assumption is based on wall pressure measurements presented by Arts & Lambert de Rouvroit (1992), taken at 43 % axial chord downstream of the trailing edge. These data showcase only approximately periodic outflow conditions (see Fig. 4.6). Since the outflow state is close to critical (sonic)

conditions ($Ma_{is} = 1.02$), one must expect large sensitivity of the flow solution even to small uncertainties or errors. Fransson *et al.* (1999) underline that such sensitivities of transonic cascade flow to small uncertainties in the boundary conditions is challenging for CFD validation purposes.

Cosmo & Salvadori (2019) achieve a remarkably precise reproduction of the experimental shock position by imposing the corresponding period of the pitch-wise exit pressure distribution from the experiment by means of a reflecting, but local boundary condition. This procedure is of course not a viable alternative to NRBCs in most turbomachinery CFD scenarios. But in this case, it strongly promotes the assumption that the the shock position discrepancy between the VKI measurements and CFD results, that are deemed to be accurate solutions to the idealized flow problem, emerge primarily from the insufficient periodicity in the experiment.

To conclude, this test demonstrates that not only the prediction of unsteady flow phenomena can be impaired by the use of reflecting boundary conditions in combination with boundary surfaces that are positioned too close to the flow field of interest. In this case, the shock strength and position of a transonic turbine blade is affected when a boundary condition interferes with the interior flow field. This effect vanishes if the boundary is located sufficiently far away or a non-reflecting boundary condition is applied. In steady-state flow, the spectral, two-dimensional NRBC presented in this work proves to be equivalent to the popular, steady, two-dimensional NRBC by Giles. Both NRBCs render accurate flow predictions even with limited spacing of the boundary surface. However, as they are derived from the linearized Euler equations, they are not perfectly non-reflecting under highly demanding conditions. Here, a (nonlinear) shock together with very little axial spacing leads to locally confined and minor, but evident variations in the shock region implying that the flow field is not perfectly independent of the boundary location and, therefore, the boundary condition method is regarded to be almost, yet not perfectly non-reflecting.

4.2 Two-dimensional acoustic mode in an annular duct

4.2.1 Test case design and numerical setup

In this section, the propagation of a single acoustic mode through a thin, annular duct in purely axial, subsonic, inviscid flow is investigated. The resulting flow problem is quasi two-dimensional and, hence, chosen to examine the spectral NRBC in conditions compliant to the assumptions made for the derivation of this kind of NRBC from the linearized two-dimensional Euler equations.

The aim of this test case is not only to visualize numerical reflections that are not as striking and obvious as, for example, disturbed shocks. But due to its simplicity, this test case is well suited to quantify and compare the reflection properties of different boundary condition methods. Moreover, this test case demonstrates the ability of spectral NRBC, that are based on a wave splitting approach, to not only prescribe homogenous inflow conditions, but to impose specific incoming perturbations (see Section 3.2.4).

We consider an annular duct of radius $r = 1\,\mathrm{m}$ and thickness $\Delta r = 0.3\,\mathrm{mm}$. The flow is inviscid and the background flow is homogeneous and purely axial ($Ma = 0.6$, $\bar{p} = 10^5\,\mathrm{Pa}$). Therefore, there is no radial pressure gradient and the test case can be regarded as two-dimensional, such that the computational mesh comprises only one layer of cells in the radial direction and inviscid sidewalls. An acoustic, spinning mode of constant nodal diameter $m = 400$ is imposed at the inflow boundary using the spectral boundary conditions presented in this work. As the solution is periodic, the computational domain is truncated in pitch ($P = \frac{2\pi r}{m} \approx 0.01572\,\mathrm{m}$) and periodic boundary conditions are applied in the circumferential direction. The axial extent of the computational domain is chosen to $\Delta x = 0.0125\,\mathrm{m}$. At the outlet boundary the spectral boundary condition is compared to Giles' steady 2D and Giles' approximate 2D boundary conditions and a characteristic, 1D boundary condition (see Chapter 2 or Section 3.2). The cut-off ratio ξ (see Eq. (3.44)) is varied from 0.05 to 2 by modifying the frequency of the spinning mode at a constant inlet pressure amplitude of $|\hat{p}_0| = 200\,\mathrm{Pa}$ (0.2 % relative pressure). Furthermore, the pressure amplitude of the acoustic mode is varied from 20 Pa to 20,000 Pa (0.02 - 20 % relative pressure) using the spectral NRBC at a constant cut-off ratio of $\xi = 0.5$ in order to investigate the impact of the linearization used to derive this type of boundary condition.

Unless otherwise stated, the numerical setup is kept constant across all parameter and boundary condition variations. The mesh comprises 53 rectangular cells in pitch-wise direction and 50 cells in axial direction, resulting in 2,650 cells in total. As the nodal diameter of the acoustic mode is constant and matches the computational domain, a rather high spatial resolution of 53 cells per wavelength in circumferential direction is guaranteed for all cut-off ratios. As the axial wavelength varies depending on the cut-off ratio and even becomes a complex-valued number for cut-off modes, the axial resolution varies accordingly. Therefore, at $\xi = 0.05$ the mesh is refined in axial direction by a factor of four yielding a resolution of still 25 cells per wavelength. The minimal axial resolution using the original mesh is about 34 cells per wavelength at $\xi = 0.25$. Time integration is performed using the second-order accurate scheme by Crank & Nicolson (1947) as it offers a small dissipation error for small computational costs when used with sufficient temporal resolution (see Ashcroft *et al.*, 2013). In this study, the acoustic mode is resolved with 256 time steps and 50 pseudo-time iterations per time step. Although the frequency and therefore the time step size vary depending
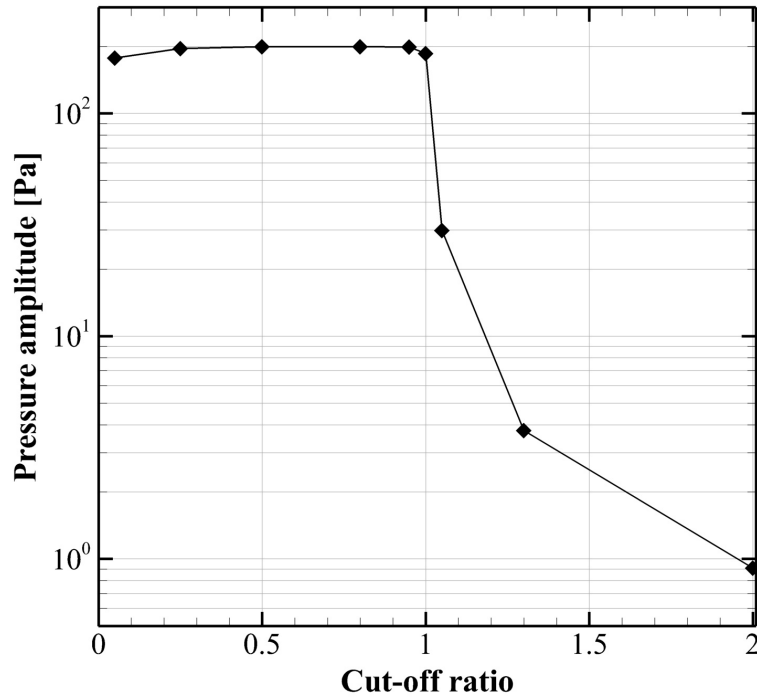
Figure 4.7: Amplitude of downstream propagating mode when reaching the outflow boundary.

on the cut-off ratio, the rate of change per time step is constant yielding a comparable temporal discretization error. Since the unsteadiness is represented by just one harmonic oscillation and hence smooth, this time integration is quite accurate compared to most setups of turbomachinery applications. Nonetheless, an implicit third-order accurate Runge-Kutta scheme (Ashcroft *et al.*, 2013) is employed to the numerically more demanding cases of $\xi = 0.05$ and $\xi = 1$. The latter describes the phenomenon of acoustic resonance where the upstream and downstream running acoustic waves coincide and form a spinning mode with no transport of energy in axial direction. As the solution is still a plane wave and not a local singularity at the inflow boundary, the wave must (in theory) travel around the circumference infinitely until it reaches the outlet boundary. To attenuate numerical dissipation, 512 time steps per period are used in this case. Furthermore, the regularization of the modal decomposition , i.e. the identification of upstream and downstream travelling waves, is crucial for this situation (see Section 3.2.2). Every computation runs for 100 cycles to ensure that the original wave and possible reflections can spread and the solution becomes perfectly periodic. For the reasons described above, the acoustic resonance case requires more cycles to reach a periodic state. Hence, the simulation time is increased to 400 cycles.

The amplitude of the acoustic mode with an original amplitude of $200\,\mathrm{Pa}$ after transmission through the computational domain and possible numerical and physical attenuation is depicted in Figure 4.7 for different cut-off ratios and their respective numerical setups. Under cut-off conditions, the expected decay when reaching the outlet can be determined by means of the axial wavenumber as a function of nodal diameter and frequency/ cut-off ratio. The imaginary part of the axial wavenumber along with the domain length yield the remaining amplitude of the analytical solution. The results at $\xi > 1$ agree very well with the analytical solution. Thus, the numerical dissipation is considered negligible.

Cut-on modes are not affected by any physical decay and deviations from the original amplitude are due to numerical dissipation. At those conditions that do not require additional numerical effort ($0.25 \leq \xi \leq 0.95$), the artificial damping is indeed negligible, too. The numerical damping at $\xi = 0.05$ is about 10 % or 1 dB, which is in accordance to the dissipation found in Wolfrum *et al.* (2020) and Schnell (2004) for this mesh resolution and solver. For acoustic resonance conditions, an estimation of numerical losses based on propagation distance and mesh resolution is not meaningful. However, the effective loss from the inlet to the outlet boundary is less than 10 %. As Section 4.2.2 will demonstrate, the precise amplitude has only very small impact on the reflection characteristics. Hence, the numerical losses observed in Fig. 4.7 are acceptable.

4.2.2 Results and discussion

Snapshots of the normalized unsteady pressure fields $\frac{p(t)-\overline{p}}{|\hat{p}_0|}$ at $t = n\frac{2\pi}{\omega}$ with $n \in \mathbb{N}$ are depicted in Figure 4.8 at cut-on conditions and in Figure 4.9 at acoustic resonance and the cut-off conditions. In the limit of $\xi \to 0$, the flow is purely one-dimensional and the wave fronts pass the boundary perpendicularly. With increasing cut-off ratio ($0.05 \leq \xi \leq 0.8$), the wave fronts become more and more inclined such that the circumferential component of their direction of propagation grows. Note that the wave fronts align with the axial direction when the mode is purely spinning without any propagation in axial direction in a reference system that is convected along with the background flow with $\overline{u} = a\,Ma$. For the given Mach number, this is approximately the case at $\xi = 0.8$. However, this situation is, in general, not identical to the acoustic resonance condition as the resulting mode still has a non-vanishing, positive axial component of the effective group velocity in the absolute frame of reference due to convection by the background flow. Only in the limit of zero background velocity, this case corresponds to acoustic resonance. Therefore, the angle between the mean flow direction and the the wave front normal grows beyond 90° until the negative, axial component of the wave propagation in the convected frame of reference and the convection velocity cancel out each other yielding a vanishing axial component of the group velocity vector, i.e. no axial transport of energy, and thus acoustic resonance ($\xi = 1$). With cut-off ratios $\xi > 1$, the mode and axial wavenumber become complex-valued (see Section 3.2.2). Accordingly, the wave decays along its path and the pressure pattern is no longer described by straight wave fronts. The rate of decay increases with increasing cut-off ratio (see also Fig. 4.7).

The steady NRBC does not allow for temporal fluctuations at the boundary which contradicts the proper representation of an acoustic mode. Therefore, the steady NRBC is not an appropriate tool for unsteady flow problems and leads to strong artificial reflections independently of the cut-off ratio. For cut-on modes, the original mode and its reflected counterpart form interference patterns. This interference is less obvious under cut-off conditions as the remaining pressure fluctuations are small close to the outlet. However, the unnatural bending of the isobars in this region indicates that the flow field is distorted by an unsuitable boundary condition.

The characteristic 1D NRBC produces only very small reflections if the flow is almost one-dimensional ($\xi = 0.05$). However, with growing incidence angles, i.e. growing cut-off ratios, reflections quickly become stronger. The same observation is true for Giles' approximate 2D NRBC albeit the error is smaller in the whole cut-on regime. This behaviour is plausible as the approximate 2D NRBC can be regarded as a one-dimensional approach extended by an approximate correction accounting for circum-
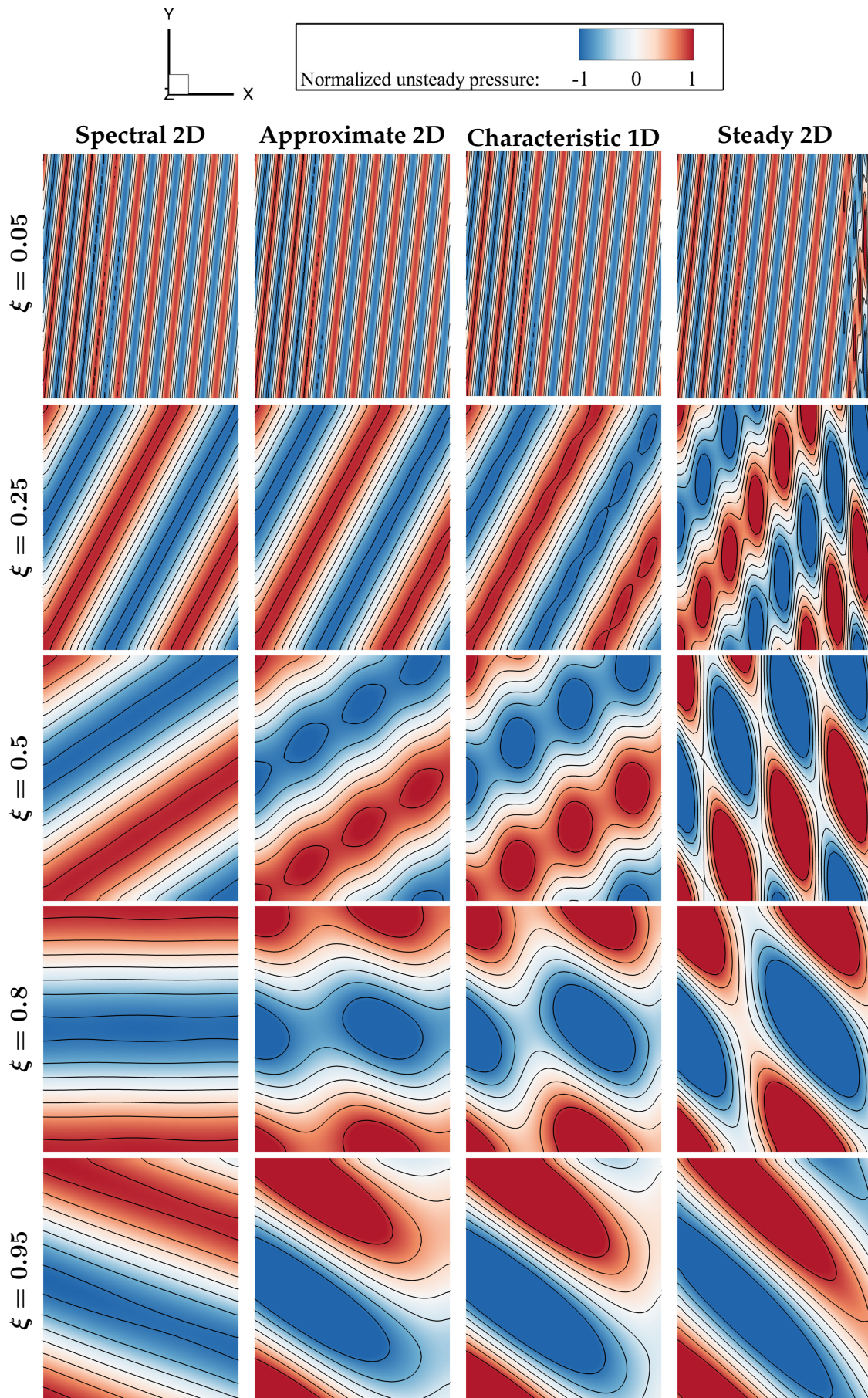
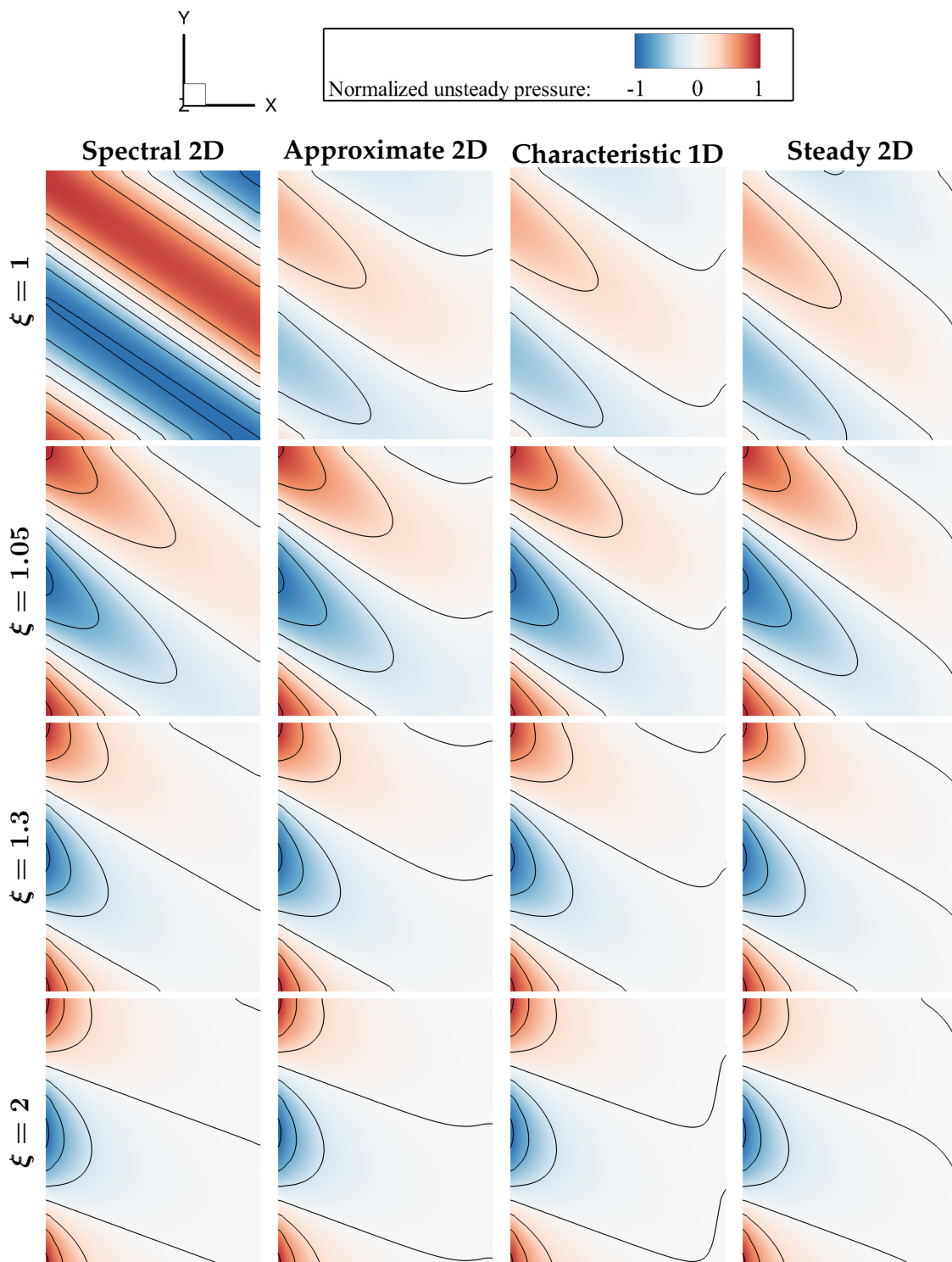Figure 4.8: Snapshots of unsteady pressure field at cut-on conditions ($\xi < 1$).

Figure 4.9: Snapshots of unsteady pressure field at acoustic resonance and cut-off conditions ($\xi \geq 1$).

ferential variations (cf. Section 3.3). For acoustic resonance and at cut-off conditions, both the characteristic 1D and the approximate 2D NRBC do not show satisfactory results. Yet, the impact of reflected cut-off modes for practical applications in turbomachinery design is limited as the reflected wave is also cut-off and therefore the effective error in the region of interest is small as long as the computational domain is not extremely truncated or the boundary flow field itself is not part of the subsequent analysis (e.g. in acoustics).

The pressure field predicted with the spectral 2D NRBC corresponds qualitatively to the expected analytical solution exhibiting almost no visible interference pattern. Only at the most demanding cases $0.8 \leq \xi \leq 1$ the isobars are slightly curved instead of perfectly straight. Under cut-off conditions the isobars are not unphysically crooked at the outlet. The spectral 2D NRBC is the only boundary condition in the present study that is capable of predicting a plausible flow solution under numerically very challenging acoustic resonance conditions.
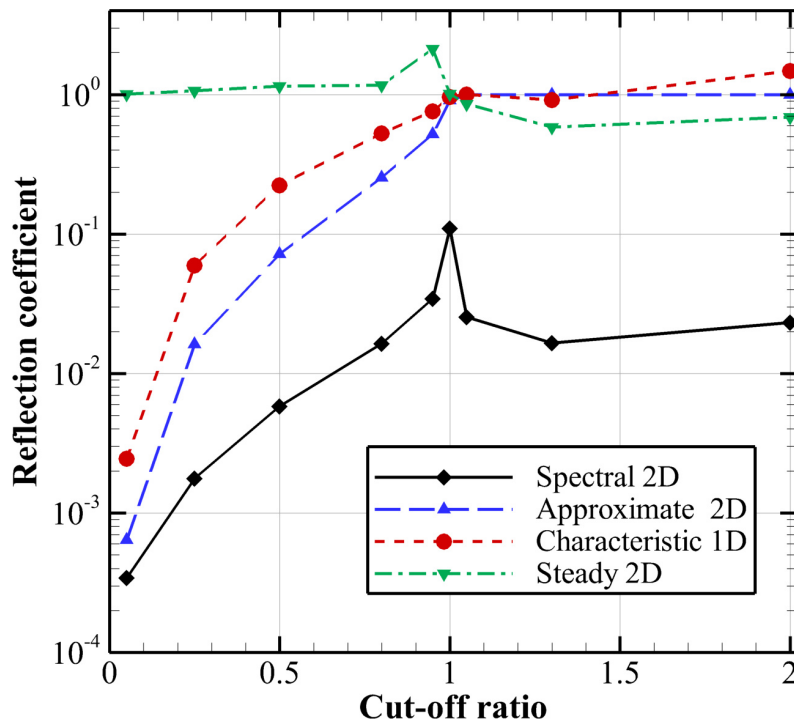
Figure 4.10: Reflection coefficient as a function of cut-off ratio using different boundary conditions.

Figure 4.10 supports the qualitative conclusions drawn from Fig. 4.8 and Fig. 4.9 quantitatively. The reflection coefficient Γ, evaluated at the outlet boundary, is defined as the ratio of the amplitude of an incoming, i.e. reflected, mode to the amplitude of the outgoing, i.e. original, mode. These amplitudes are determined by means of the modal decomposition of the temporally and spatially Fourier-transformed boundary flow field (see Equation (3.53)).

The inability of the steady boundary condition to allow for temporal fluctuations causes any pressure perturbation to be reflected entirely. Therefore, the reflection coefficient is close to unity in the complete range of cut-off ratios. The characteristic 1D and the approximate 2D NRBC achieve significant damping under cut-on conditions, but their reflectivity strongly depends on the wave incident angle as a function of the cut-off ratio. As expected, the approximate 2D boundary condition produces weaker reflec-

tions in the cut-on regime. While the characteristic 1D NRBC provides damping of at least one order of magnitude for cut-off ratios smaller than 0.25, the approximate 2D NRBC yields reflection coefficients smaller than 0.1 for cut-off ratios smaller than 0.5. In the cut-off regime both boundary conditions do not offer a significant reduction of numerical reflections.

On the contrary, using the spectral 2D NRBC cuts down the amplitude of artificial reflections by a factor of 50 or more except for conditions close to acoustic resonance. Note that the modal decomposition matrix is singular at acoustic resonance and therefore needs regularization (cf. Chapter 3.2.2 or Frey & Kersken (2016)). Hence, the analysis is inaccurate for $\xi \to 1$ and care needs to be taken for the interpretation of reflection coefficients in this region. Figures 4.8 and 4.9 suggest that the actual reflection using the spectral 2D NRBC is less than indicated by the reflection coefficient. Altogether, the spectral 2D NRBC exhibit a further reduction of spurious reflections compared to the state-of-the-art, approximate 2D NRBC by at least one order of magnitude in the whole cut-off ratio range except at small cut-off ratios, where even less advanced 1D boundary conditions yield acceptable results.

Chassaing & Gerolymos (2007) report comparably advantageous reflection properties of their implementation of spectral 2D NRBC in a similar study of plane waves in a two-dimensional, circular duct. In fact, they observe even smaller reflection coefficients close to acoustic resonance and under cut-off conditions. However, their simulations employ a fifth order accurate spatial scheme with a very high mesh resolution. Furthermore, they observe very slow convergence (requiring up to 1000 cycles) and stability issues if the spectrum of circumferential harmonics included by the boundary condition is not limited to large scale modes. This strongly limits the applicability of their implementation to turbomachinery flow problems that might involve strong gradients or shocks. It is not clear whether the smaller reflection coefficients observed by Chassaing and Gerolymos are due to their enhanced numerical setup or to differences in the implementation of the boundary condition.

However, Henninger *et al.* (2015) conduct a similar study with an implementation of an NRBC by Hagstrom & Goodrich (2003) in the TRACE solver. A more detailed (German-language) analysis of the same test case can be found in the PhD thesis of the first author (Henninger, 2019). He observes that the damping coefficient, evaluated within the domain, does not drop below the level observed in the present work even in numerical experiments conducted on an elongated domain that are terminated before a possible reflection can travel back to the region of interest. Hence, Henninger concludes that the residual damping might be due to residual noise in the numerical solution itself or the iterative temporal Fourier transform, which is required for the modal decomposition and calculation of the reflection coefficient, rather than due to spurious reflections from the boundary.

Another effect that possibly causes the residual reflection coefficient is that, even if the numerical solution and its Fourier representation perfectly converge and the error in the numerical solution of the discretized system of equations is negligible, the discretization in space and time itself introduces a certain amount of artificial dissipation and dispersion. Hence, the propagation of waves in the numerical system does not perfectly match the wave propagation described by the purely physics-based dispersion relation. Thus, the analysis based on a wave-splitting approach is subject to a small error due to this discrepancy between numerical and analytical wave propagation (cf. Rowley & Colonius, 2000). However, this error is in the same order of magnitude as the error of any particular discretization scheme and therefore it is acceptable within

Table 4.2: Sensitivity of the reflection coefficient Γ to amplitude variations using the spectral 2D NRBC at $\xi = 0.5$.

$|\hat{p}_0|$ [Pa]	$|\hat{p}_0|/\overline{p}$	Γ	$\frac{\Gamma - \Gamma_{\hat{p}_{0,min}}}{\Gamma_{\hat{p}_{0,min}}}$
20	$2 \cdot 10^{-4}$	$5.821882 \cdot 10^{-3}$	-
200	$2 \cdot 10^{-3}$	$5.821866 \cdot 10^{-3}$	$-2.75 \cdot 10^{-6}$
2,000	$2 \cdot 10^{-2}$	$5.820282 \cdot 10^{-3}$	$-2.75 \cdot 10^{-4}$
20,000	$2 \cdot 10^{-1}$	$5.670000 \cdot 10^{-3}$	$-2.61 \cdot 10^{-2}$

the expected accuracy of any given numerical setup.

Although the residual reflection coefficients in the present study are larger compared to the study of Chassaing and Gerolymos, the numerical setup used here is more comparable to setups that are typically used in turbomachinery CFD and the resulting reflection properties constitute a substantial advancement in comparison to prevalent approximate or 1D boundary conditions. The residual level of reflection is deemed negligible for very most applications in the analysis of turbomachinery flows and related disciplines.

In Table 4.2, the impact of the modal amplitude on the reflectivity of the spectral 2D boundary condition is examined. Albeit the boundary condition is based on a linearization approach assuming sufficiently small variations about a constant mean state, the resulting reflection coefficient is constant over a wide range of amplitudes. Even when the acoustic mode induces fluctuations of 20 % relative pressure (or 40 % peak to peak variation), the reflection coefficient changes only by about 3 % with respect to the reflection coefficient observed at 0.02 % relative pressure amplitude ($\Gamma_{\hat{p}_{0,min}}$). This variation is very small in comparison to the range of reflection coefficients when varying the boundary condition method or cut-off ratio. In turbomachinery flows, in particular in transonic and supersonic conditions, even larger pressure fluctuations might occur in total. Yet, a steep gradient in the flow field will, in general, not be represented by a single harmonic in the spectral domain, but it will be formed by superposition of a substantial number of harmonics, each of moderate magnitude. This explains why the spectral boundary condition provides satisfying reflection properties in the presence of shocks (cf. sections 4.1 and 5.1) even though it is based on the linearized Euler equations.

4.3 Tenth standard configuration

This section is a revised version of a study of the tenth standard configuration presented at the ISABE conference (see Schlüß & Frey, 2019).

4.3.1 Test case design and numerical setup

The academic flutter case standard configuration number ten is a well-established numerical flutter experiment for code validation purposes. The two-dimensional flow through an oscillating cascade of modified, i.e. 5% cambered, NACA0006 airfoils with pitch-to-chord ratio of unity and 45° stagger angle is investigated. For details on the geometry, flow conditions and blade modes and a comprehensive overview of reference results obtained by different authors using a variety of methods see the report by Fransson & Verdon (1992). This test case is known for being sensitive to artificial reflections from the boundaries, in particular in the vicinity of conditions where acoustic resonance occurs. Hence, in this work, it serves to validate the spectral NRBC and to demonstrate their superior reflection properties. We consider subsonic flow conditions ($Ma = 0.7$) with a blade pitching motion at reduced frequency $\omega^* = \frac{c\omega}{2\|V\|} = 0.5$ based on the half chord length $c/2$, the angular frequency of the pitching motion ω and the mean inflow velocity V. These conditions are referred to as cases 3 (σ=0°) and 4 (σ=90°) in the literature. The pitching motion imposed onto the blade has an amplitude of one degree. The inlet and outlet boundaries are located roughly one chord length away from the leading and trailing edges.
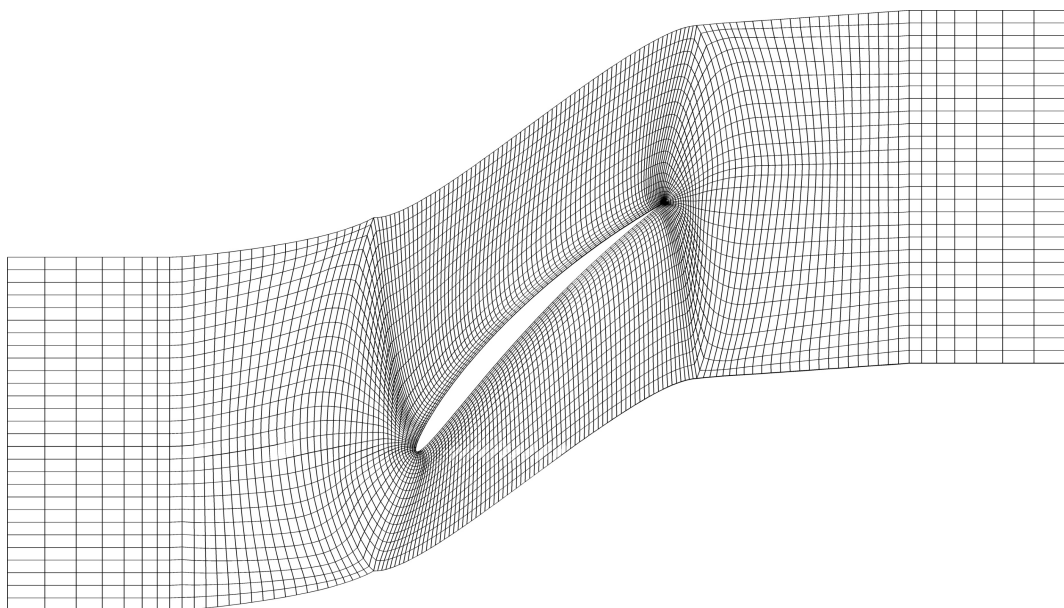
Figure 4.11: Single passage mesh of the tenth standard configuration.

The results of the present study are compared to reference results by Verdon & Usab (1986) and Hall & Clark (1991), both are available in Fransson and Verdon's overview report. Verdon's method solves the time-linearized, compressible potential flow equations. A finite-difference approximation of the governing equations is directly solved using Gaussian elimination. Hall solves the time-linearized Euler equations by means of a finite-volume approach and pseudo-time stepping. Subsequent to Fransson and

(a) Spectral 2D NRBC   (b) Approximate 2D NRBC   (c) Characteristic 1D NRBC
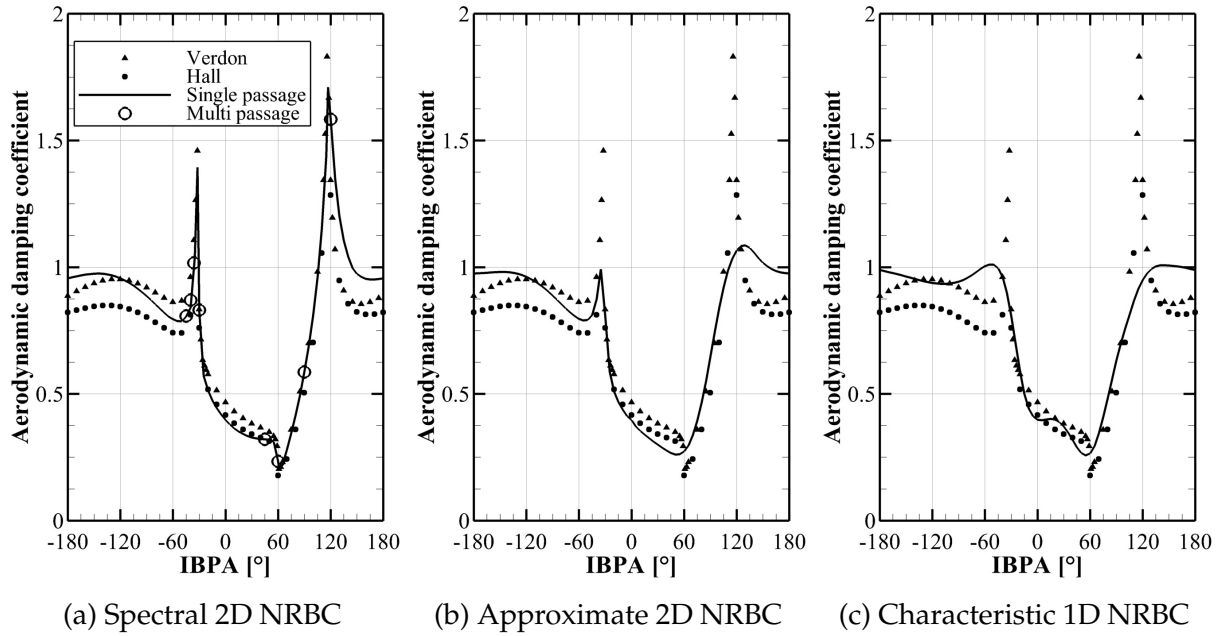
Figure 4.12: Aerodynamic damping versus inter-blade phase angle.

Verdon's report, numerous authors have used this test case to validate their methods (see e.g. Petrie-Repar *et al.*, 2006; Huang, 2013; Henninger, 2019; Chuang & Verdon, 1999; Kahl & Klose, 1993; Kersken *et al.*, 2012). The good mutual agreement of methods of different levels of abstraction and fidelity supports the validity and common acceptance of the references provided by Verdon and Hall.

Single passage time marching simulations are conducted using the phase lag approach (see Section 3.4.1 and references therein) for the complete range of IBPAs with the presented spectral two-dimensional NRBC as well as with one-dimensional characteristic boundary conditions and Giles's approximate two-dimensional NRBC for comparison. Further, multi-passage computations are performed with truly periodic boundaries and spectral NRBC for some IBPAs, that can be computed using integer blade counts. The flow is assumed to be inviscid and two-dimensional. An implicit dual time-stepping BDF2 scheme with 64 time steps per cycle is employed. The mesh comprises 5824 cells and is depicted in Figure 4.11.

4.3.2   Results and discussion

Figure 4.12 shows that using the spectral two-dimensional NRBC, the predicted aerodynamic damping coefficient

$$\Xi = \frac{-\operatorname{Re} W_{\text{aero}}}{\pi \alpha^2 c^2 b p_{dyn}} \tag{4.3}$$

agrees well with reference results. Here

$$W_{\text{aero}} = -\mathrm{i}\pi \int_A \Psi^H \widehat{(pn)}_\omega dS \tag{4.4}$$

represents the aerodynamic work per cycle of a structural eigenmode Ψ with blade surface A and surface normal unit vector n. The pitching angle (radian measure) is
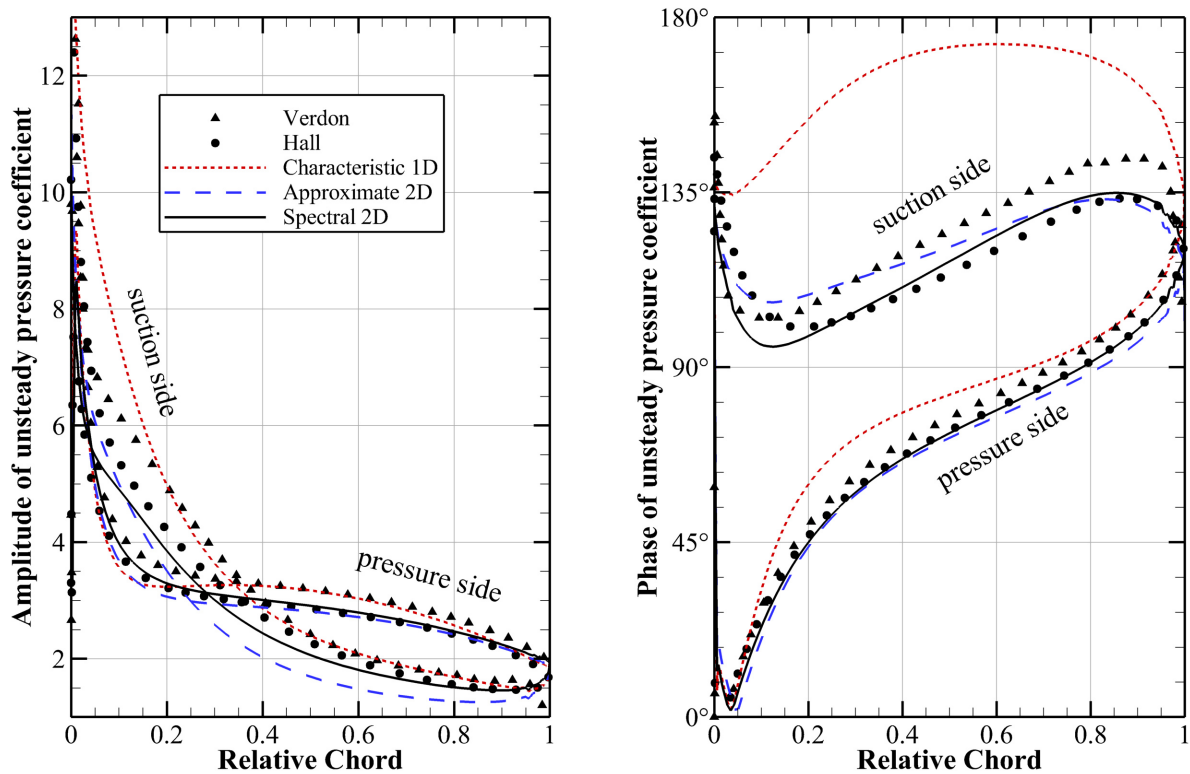
Figure 4.13: Amplitude and phase angle of unsteady pressure coefficient along the blade surface (case 4: $\sigma = 90°$).

denoted by α and b is the blade span, i.e. in this quasi 2D case the thickness of the S1 plane. Note that the dynamic pressure p_{dyn} in this work and Hall's reference results refers to the (more eligible) compressible dynamic pressure definition ($p_{dyn} = p_t - p$) whereas Verdon uses the incompressible dynamic pressure. The results obtained from the multi-passage simulations agree perfectly with the results from the phase lag computations. This indicates that the special treatment of spatial harmonics with wavenumber zero, as described in Section 3.4.3, does not affect the final solution. In contrast, using the characteristic one-dimensional NRBC yields a qualitatively different damping curve. The distinct peaks at acoustic resonance conditions are not captured correctly. The minimal damping at about 60° is overestimated. Giles's approximate NRBC provides better results than simple characteristic NRBC. They exhibit weak peaks at the correct IBPAs, but in the vicinity of acoustic resonance, the agreement with the references is poor. The accuracy of the approximate NRBCs decreases with increasing absolute value of the circumferential wavenumber, i.e. increasing absolute value of the IBPA, because Giles's approach is based on a Taylor series expansion about $l/\omega = 0 \frac{s}{m}$. This becomes evident as the peak at $\sigma \approx$ -30° is better reflected than the peak at $\sigma \approx 120°$. Also, Giles' approximate NRBC lead to an overestimated minimal damping coefficient.

Although the characteristic 1D and Giles' approximate 2D NRBC yield damping coefficients that significantly differ from the reference results for a wide range of IBPAs, the predicted damping coefficients at case 3 and case 4 conditions agree relatively well with the spectral NRBC and the references by Verdon and Hall. At $\sigma = 0°$ (case 3), the dominant waves leave the domain perpendicularly to the boundary. In this case, the predicted damping values of all three NRBCs coincide. Here, Giles's approximate 2D NRBC and the characteristic 1D NRBC can correctly describe the outgoing mode with-

(a) Spectral 2D NRBC   (b) Approximate 2D NRBC (c) Characteristic 1D NRBC
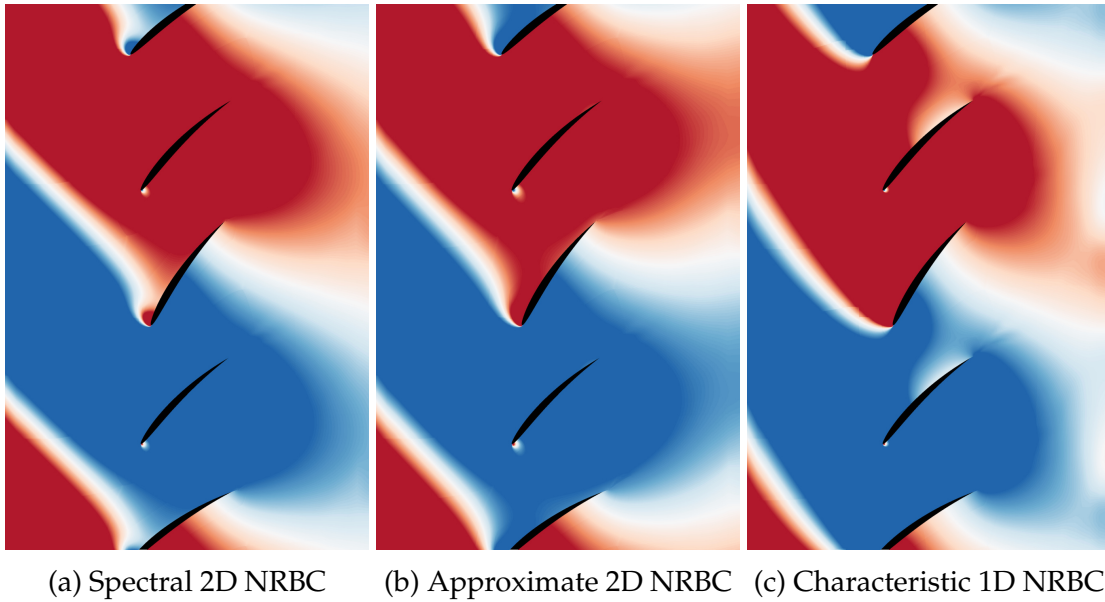
Figure 4.14: Snapshot of unsteady pressure fluctuations, positive values red, negative values blue (case 4: $\sigma = 90°$).

out any conceptual limitation.

Yet, a more detailed analysis of case 4 ($\sigma = 90°$) reveals that the local unsteady blade pressure, i.e. the source of aerodynamic damping or excitation, may vary notwithstanding that the disparity in the integral damping among the different NRBCs and reference results is only about 10 %. For this purpose, we examine the blade surface distribution of the amplitude-scaled, unsteady pressure coefficient

$$\hat{c}_p = \frac{\hat{p}}{\alpha \, p_{dyn}} \tag{4.5}$$

in Figure 4.13. The unsteady blade pressure computed with the spectral 2D NRBC corresponds satisfactorily to the reference results, in particular to Hall's data. While the aft portion of the suction-sided and the entire pressure-sided $\hat{c}_p$ distribution matches Hall's distribution, the amplitude in the leading edge region of the suction side deviates to an amount comparable to the discrepancy among the reference results themselves. In contrast, the unsteady pressure predicted by the characteristic 1D NRBC differs considerably in phase, especially on the suction side. Moreover, the amplitude is overestimated in the front section of the suction side. The solution obtained using the approximate 2D NRBC exhibits a smaller unsteady pressure amplitude on the entire suction side compared to the references and the solution with the spectral NRBC. The pressure-sided amplitude as well as the phase along the entire blade surface agree well between the 2D NRBCs and the reference results.

The pressure fluctuation arising from the blade pitching motion at the moment of maximum displacement of the central blade is depicted in Figure 4.14 in order to visualize non-physical reflections at artificial boundaries. Note that the actual blade movement is amplified by a factor of ten in this figure for visualisation purposes. Additionally, the computational domain and flow solution is extended in circumferential direction by copying and rotating the flow solution of the single passage computations with respect to the correct phase shift. As, for the given IBPA of $\sigma = 90°$, the upstream prop-

agating perturbation upstream of the blade row is a single cut-on mode, we can expect straight wave fronts. However, when employing one-dimensional boundary conditions, the resulting wave fronts are curved revealing that the upstream travelling acoustic wave does not undistortedly pass through the inflow boundary. The reflection of the cut-off mode occurring at the outlet with the one-dimensional boundary condition is even more obvious. Analogously to Section 4.2.2, we observe that the approximate 2D NRBC also struggle to correctly absorb the cut-off mode at the outlet while the upstream propagating cut-on mode seems to be better captured at the inlet boundary. However, the unsteady pressure differs in the leading edge section of the suction side between the spectral and the approximate NRBC when the blade is fully deflected. The pressure pattern of the solution obtained with the spectral NRBC does not display any effects of artificial reflections. Supported by the findings from the global aerodynamic damping (cf. Fig. 4.12) and the analysis of the local unsteady blade pressure distribution (cf. Fig. 4.13) and the agreement with the references therein, the pressure field predicted by the spectral NRBC is regarded as plausible and most accurate among the boundary conditions investigated here.
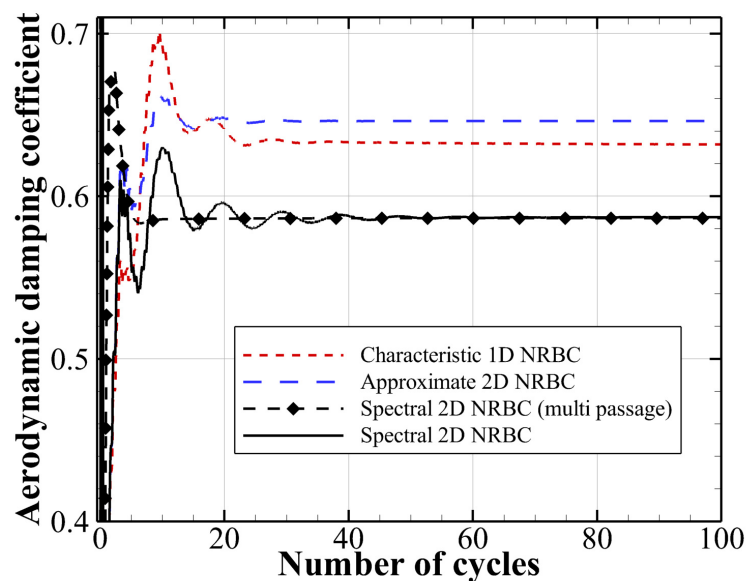
Figure 4.15: Development of damping coefficient (case 4: $\sigma = 90°$).

Figure 4.15 depicts the convergence of the damping coefficient at $\sigma = 90°$. Two things can be observed here: The spectral two-dimensional boundary conditions need more time steps to reach a converged value compared to the one-dimensional and the approximate boundary conditions. However, the multi-passage simulations converge much faster and exhibit no oscillations whereas the curves of phase lag simulations, and in particular the one using spectral NRBC, are less smooth. There are two effects that contribute to this observation. The phase lag approach is per se prone to such oscillations. When additionally the inflow and outflow boundaries depend on slowly converging temporal Fourier coefficients, the harmonic convergence is further lagged. Moreover, in single passage simulations with non-zero IBPA, the mode with circumferential wavenumber equal to zero is not part of the expected spectrum. As this mode is not accounted for in the spectral analysis, the aforementioned transient extrapolation of waves that propagate perpendicularly to the boundary is not applicable here.

5 Applications

5.1 Steam turbine flutter

The following section is a revised version of a study of this test case presented at the ISUAAAT conference by the author (see Schlüß & Frey, 2018). It is supplemented by summarized conclusions from a subsequent article based on the same test case (Frey *et al.*, 2019) in Section 5.1.5. The author of the thesis at hand has contributed to that article as a co-author.

5.1.1 Test case design and numerical setup

To assess the reflection properties, efficiency and stability of the boundary conditions presented in this work in a real, three-dimensional turbomachinery test case, the flutter stability of a transonic steam turbine stage is studied. The configuration has originally been established at Durham University (see Burton, 2014) and later been proposed as an open, numerical test case for flutter in steam turbines by the KTH turbomachinery group. The geometry, the mode shape and further information on the flutter configuration can be found in Qi *et al.* (2017) and on the corresponding KTH Website (2021). The results will be compared to references by Sun *et al.* (2017) obtained with the time-linearized flow solver LUFT (see Petrie-Repar *et al.*, 2007) , which utilizes three-dimensional NRBC (see Petrie-Repar, 2010), and with the commercial, nonlinear time domain solver Ansys CFX.

Table 5.1: Overview of operating conditions and blade parameters.

$p_{t,Inlet}$	27	kPa
$T_{t,Inlet}$	340	K
p_{Outlet}	8.8	kPa
Ω	3000	1/min
b	920	mm
$c_{mid-span}$	163.2	mm

Figure 5.1 shows a sketch of the configuration consisting of a stator row with 60 blades, a rotor row with 65 blades and a downstream diffuser. A simplified, linear distribution of relative span in accordance to the original test case description is used for analysis. It is outlined in Fig. 5.1 and its definition can be found on the KTH website. The operating conditions are taken from the same sources and summarized in Table 5.1. The inflow is roughly axial. In contrast to the references produced with LUFT, this study incorporates the original tip gap (cf. Burton, 2014) of 4.2 mm or about 0.5 % relative span. The CFX results are available either without the tip gap (like the LUFT results)
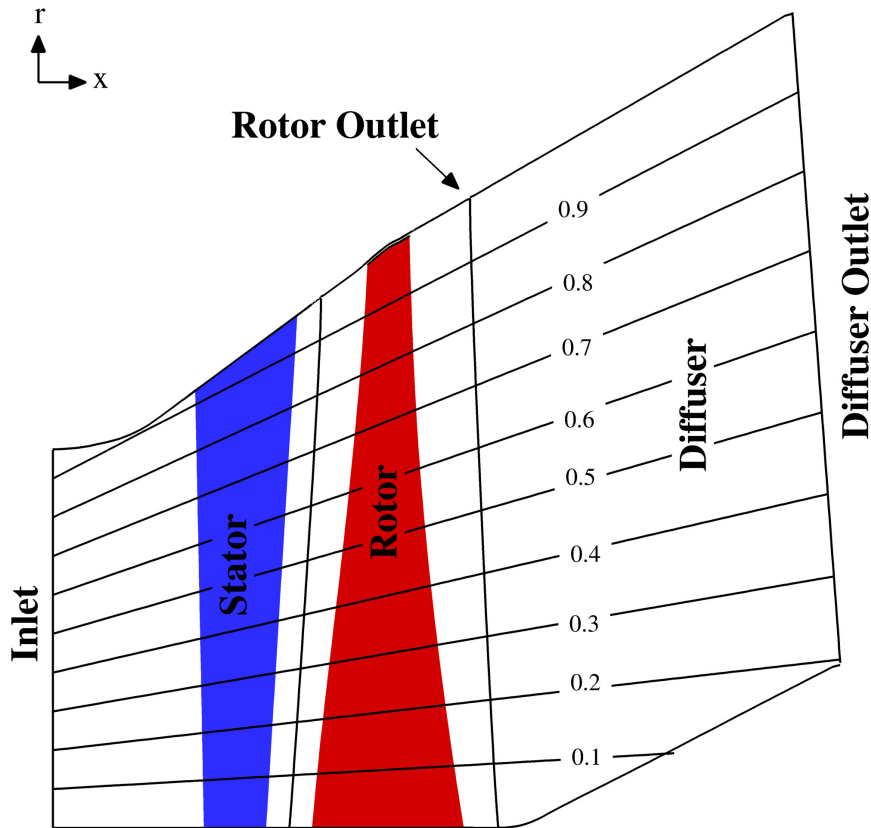
Figure 5.1: Schematic of the steam turbine stage depicting the computational domain and the definition of relative span.

or with a reduced tip gap (2.1 mm or 0.25 % relative span).

The flutter analysis is based on the energy method and focuses on the first bending mode of the rotor. A travelling wave mode is assumed and the normalized mode shape is provided for download on the KTH website. In the present study, the amplitude is scaled such that the maximum displacement d_{max} at the tip trailing edge is 3 mm, which is in the order of the trailing edge thickness. In Section 5.1.5 we will see that at this amplitude the aerodynamic response can be regarded as linear and, hence, the non-dimensional aeroelastic properties are independent of the amplitude. The bending mode magnified by a factor of twenty is depicted in Figure 5.2. An artificial modal frequency of 132.08 Hz is adopted from the test case authors. The numerically determined natural frequency of the bending mode is smaller. But for this purely numerical analysis, the modal frequency is modified such that it is equivalent to a reduced frequency of $\omega^* = \frac{\omega\,c}{2\|V_{Exit}\|} = 0.15$, which is within the typical range of a real steam turbines (cf. Sun *et al.*, 2017).

Table 5.2: Ideal gas parameters.

R	461.52	$\mathrm{J \cdot kg^{-1} \cdot K^{-1}}$
γ	1.12	-
μ	$1.032 \cdot 10^{-5}$	$\mathrm{N \cdot s \cdot m^{-2}}$

The underlying mean flow is calculated in a steady simulation beforehand. Here, the
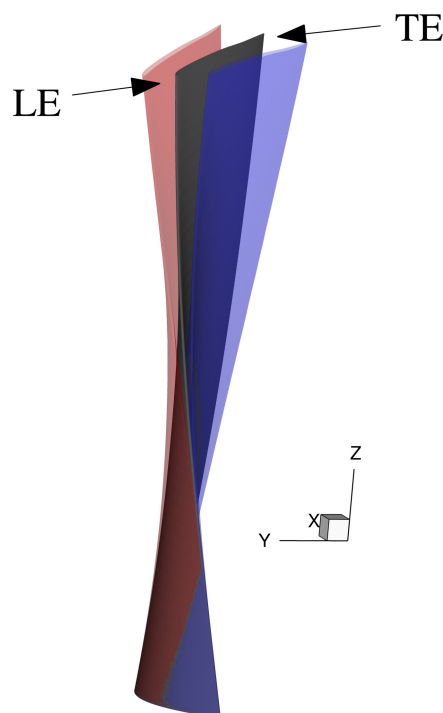
Figure 5.2: Illustration of bending mode magnified by factor twenty.

exit pressure is imposed at mid-span of the diffuser outlet along with a radial equilibrium condition. The diffuser domain is included in the rotor system without an additional interface. In order to assess the reflection properties of the boundary conditions, flutter simulations are also conducted with a shorter computational domain without the diffuser (see Figure 5.1). The short configuration is a demanding test case for boundary conditions as the oscillating trailing edge shock impinges on the outflow boundary. Computations are carried out using both spectral 2D and characteristic 1D boundary conditions for comparison. The circumferentially averaged pressure profile is extracted from the steady simulation at the rotor exit plane and the diffuser exit plane. These profiles are then prescribed in the unsteady simulation at their respective position. To ensure comparability between simulations using the long and the short domain, it has been verified that the mass flow as well as the time-mean radial pressure distribution at the rotor outlet remain constant.

The computational mesh is generated by means of DLR's in-house tool PyMesh (see Weber *et al.*, 2016) and comprises about four million cells in total, about 2.1 million cells thereof in the rotor domain and another 0.7 million in the diffuser domain. Note that this is a considerably finer resolution compared to the mesh used to produce the reference solutions. Blade wall boundary layers are resolved with $y^+ \approx 1$ whereas wall functions are employed at hub and casing walls with $30 < y^+ < 80$. Details of the mesh are depicted in Figure 5.3.

For all computations the Wilcox's k-ω turbulence model (see Wilcox, 1988) is employed and ideal gas with constant molecular viscosity and the parameters given in Table 5.2 is assumed. This assumption is justified for the flutter analysis of a steam turbine's last stage as shown by Petrie-Repar *et al.* (2014). To conduct single passage simulations for arbitrary IBPAs, the phase lag method is employed (see Section 3.4.1). All computations are run with an implicit, dual time-stepping algorithm using the BDF2 scheme with 128 physical time steps per cycle and 50 pseudo-time iterations per physical time
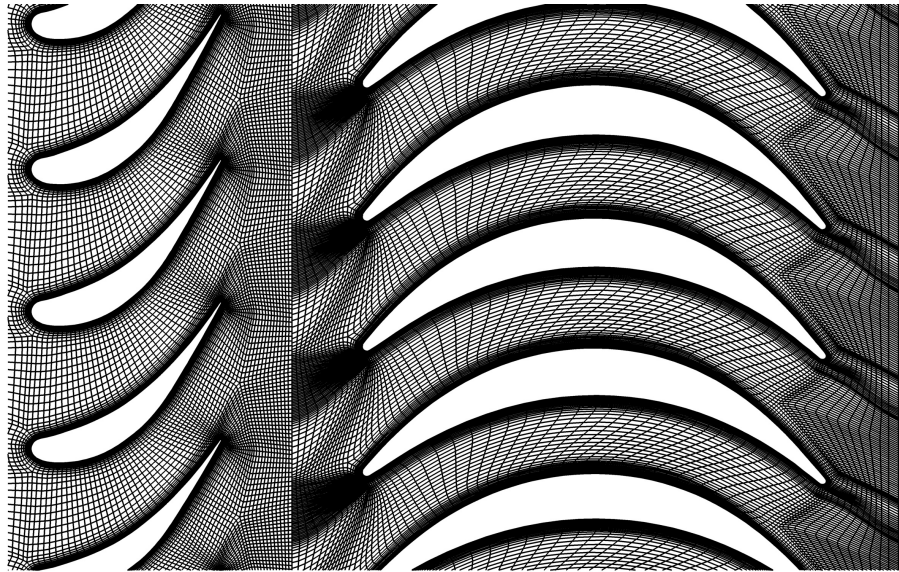
(a) Hub
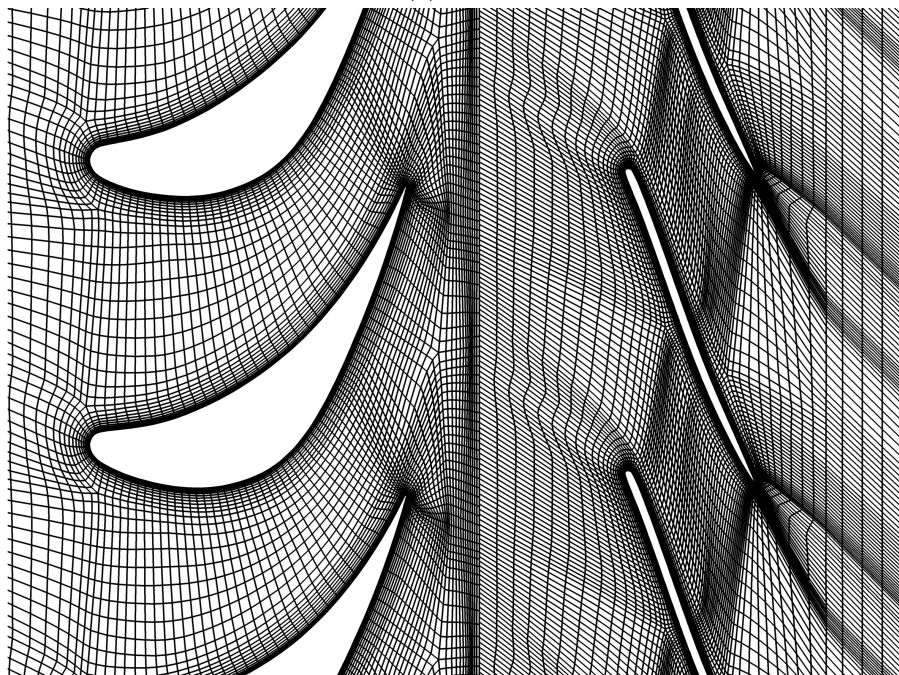
(b) Shroud

Figure 5.3: Details of mesh coarsened by factor 2 and duplicated in pitch-wise direction.

(a) 50 % span   (b) 90 % span
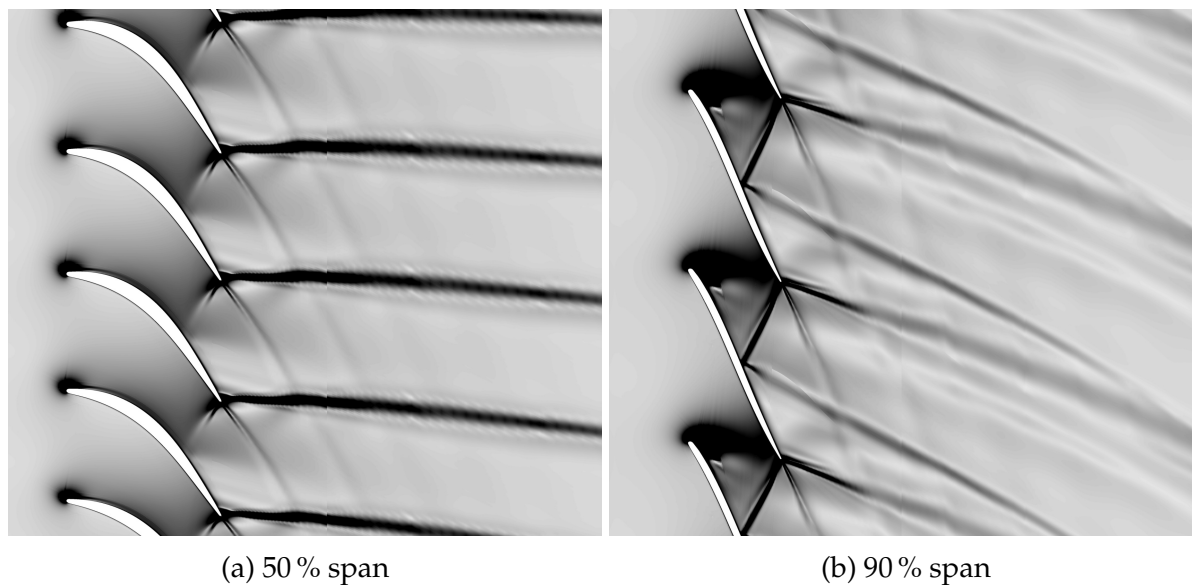
Figure 5.4: Pseudo-schlieren image of the flow in the rotor blade row (solution duplicated in pitch-wise direction).

step. For IBPAs of $-99.7°$, $-72°$, $-45°$, $0°$, $72°$ and $180°$, simulations are carried out using the truncated computational domain (without the diffuser) as well as the long domain (including the diffuser). The IBPAs are chosen such that the calculations with negative IBPA cover the region of maximum excitation while the IBPA of $72°$ is close to the point of maximum damping . At these IBPAs, the corresponding nodal diameters are integers for a given blade count of 65 blades, with the exception of $-45°$, which is chosen for comparison with the KTH references.

5.1.2 Steady Results

The mean flow in the rotor is characterized by a system of trailing edge shocks due to the high exit Mach number compared to a typical gas turbine LPT. Figure 5.4 depicts this shock system by plotting the density gradient magnitude to mimic schlieren images of slices at 50% and 90% relative span. In particular at 90% span, the pressure side branch of the trailing edge shock impinges on the neighbouring blade's suction side at about 50% chord length. Additionally, a strong expansion zone at the suction side's leading edge region, indicating a considerable incidence angle, can be observed at 90% span.

These features also become evident in Figure 5.5. It plots the rotor blade pressure distribution at the same radial positions in comparison to results from Sun *et al.* (2017) obtained with LUFT. Both solvers predict the steady blade pressure in good agreement. However, the leading edge suction peak and the subsequent shock are predicted stronger in the TRACE result. The same is true for the pressure rise related to the incident shock at about half chord in the tip region (Fig. 5.5b). At midspan, the more pronounced pressure plateau in the TRACE result at about 75 % chord is also caused by the incident shock (see Fig. 5.5a). A wall shear stress analysis reveals that the flow is still attached in this region (not shown here). A possible explanation for these differences is the fact that the mesh used in this work comprises about twice as many cells in the rotor domain as the mesh used in the references.

(a) 50 % span

(b) 90 % span
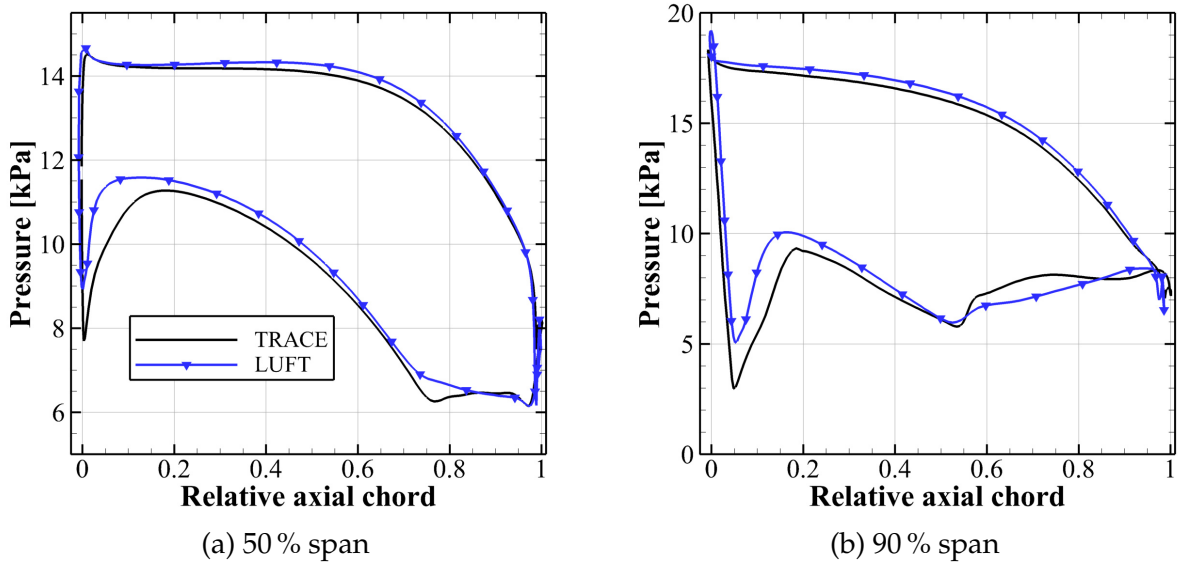
Figure 5.5: Steady blade pressure distribution at two radial positions.

Nevertheless, the steady flow solutions can be considered similar so that they pose a suitable basis for the following investigation of flutter. This is supported by the analysis of global performance quantities. TRACE predicts a mass flow of $\dot{m} = 85.43 \, \mathrm{kg \, s^{-1}}$, a total-to-static isentropic efficiency $\eta_{ts} = 83.676\%$ and a power output of $P = 11.71 \, \mathrm{MW}$. These values agree well with the results in Sun *et al.* (2017) and Qi *et al.* (2017) considering the different modelling of the tip gap.

5.1.3   Flutter analysis

To analyse flutter, let us consider the non-dimensional damping coefficient Ξ according to Equation (4.3). Here $\alpha = d_{max}/c$ denotes the normalized amplitude of the bending mode at hand (instead of the pitching angle in Section 4.3). The averaged dynamic pressure in the rotor inlet plane is $p_{dyn} = 2127.7 \, \mathrm{Pa}$.

Figure 5.6 plots the non-dimensional aerodynamic damping as a function of the IBPA for both types of boundary conditions and both domains including references from Sun *et al.* (2017).

In general, there is good agreement between the results and the LUFT references. In particular, in the range of aerodynamic excitation, i.e. negative damping, the predicted damping values almost coincide when using the spectral 2D NRBC or the characteristic 1D boundary condition along with the longer domain. The latter boundary condition, however, leads to a significant deviation when employed in combination with the short domain.

The predicted damping values depend only to a small extent on the domain length in case of two-dimensional boundary conditions. As the position of the boundary plane is expected to have an impact on the unsteady pressure field if reflections occur, the above observation suggests that there is only a small amount of reflection when employing two-dimensional boundary conditions. Since also the divergent diffuser geometry may interact with the radiated pressure field from the moving blade, solutions from the long and the short domain cannot be expected to match perfectly. Moreover, the assumptions of the flow being purely two-dimensional and perturbations being small
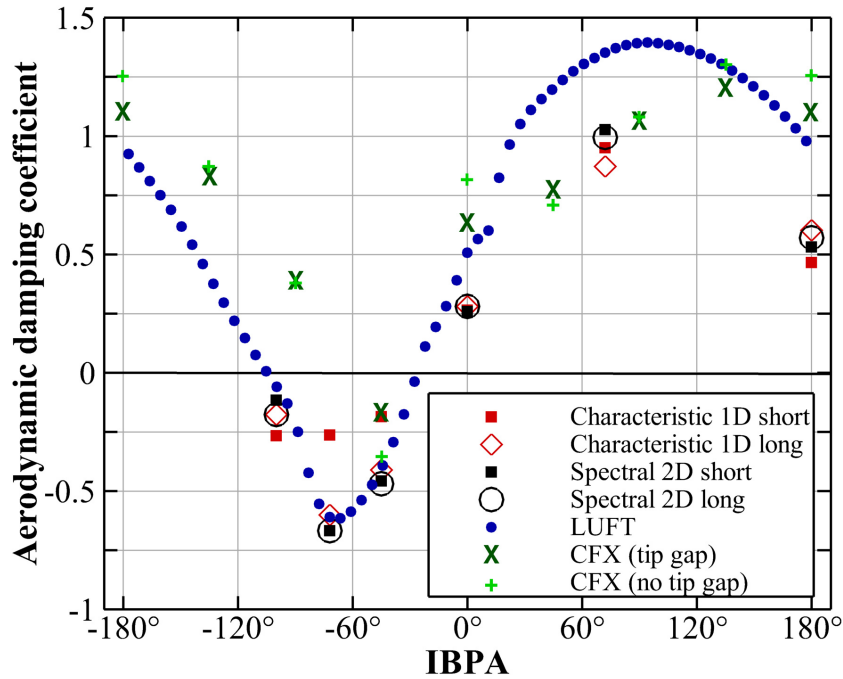
Figure 5.6: Non-dimensional aerodynamic damping versus IBPA.

are not fulfilled. Still, the small differences between the results from both domains using the two-dimensional boundary conditions indicate superior reflection properties of the spectral boundary conditions over the one-dimensional boundary conditions.

Note that for the $\sigma = 0°$ case the one-dimensional boundary conditions produce almost the same damping values as the two-dimensional boundary conditions with both exit locations. This is due to the fact that, in this specific case of synchronously vibrating blades, plane waves arise that leave the domain orthogonally to the boundary and, hence, can also be absorbed by one-dimensional boundary conditions.

The CFX results display a weaker agreement with the other solutions, especially in the region in which TRACE and LUFT predict excitation. Yet, they serve to give an estimation of the influence of the tip gap modelling. This influence on the integral damping appears not very strong for most IBPAs.

In the following, we will examine the $\sigma = -45°$ case more extensively as detailed reference data are available for this IBPA. Although the corresponding nodal diameter is non-integer ($m = -8.125$) and therefore not relevant for the full wheel configuration, the aerodynamic response can be modelled for arbitrary IBPAs using a single passage computational domain with appropriately phase-shifted periodic boundaries. Figure 5.7 plots the imaginary part of the first pressure harmonic on the rotor suction side. As the imaginary part of the pressure, along with the associated structural mode, determines the aerodynamic work and damping, this figure reveals where the differences in global damping emerge. In the solution using one-dimensional boundary conditions and the short mesh, the distinct line at the position, where the oscillating shock from the neighbouring blade impinges, is diminished in comparison to all other solutions. Furthermore, in the tip region, a spot of large pressure (imaginary part) appears in the short 1D solution.
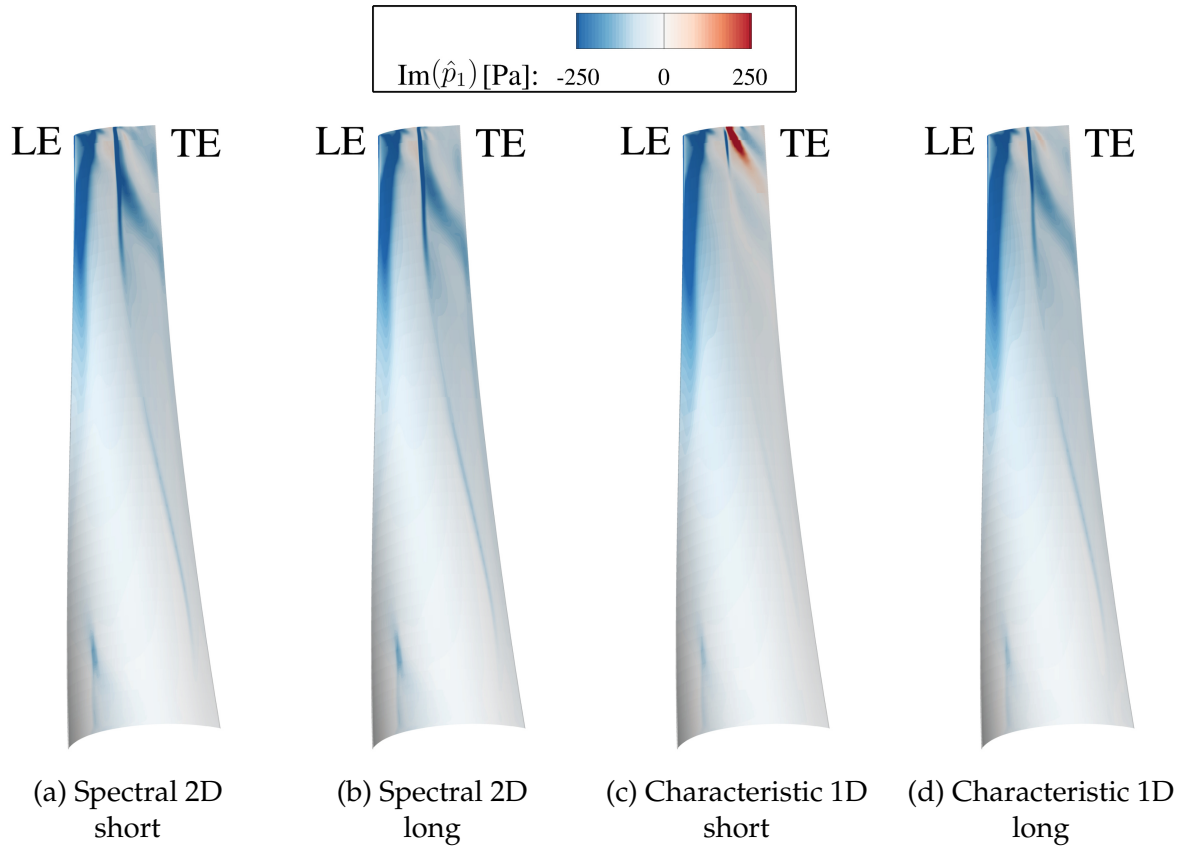
Figure 5.7: Distribution of unsteady pressure on rotor suction side associated to fundamental harmonic of blade vibration frequency (imaginary part, $\sigma = -45°$).
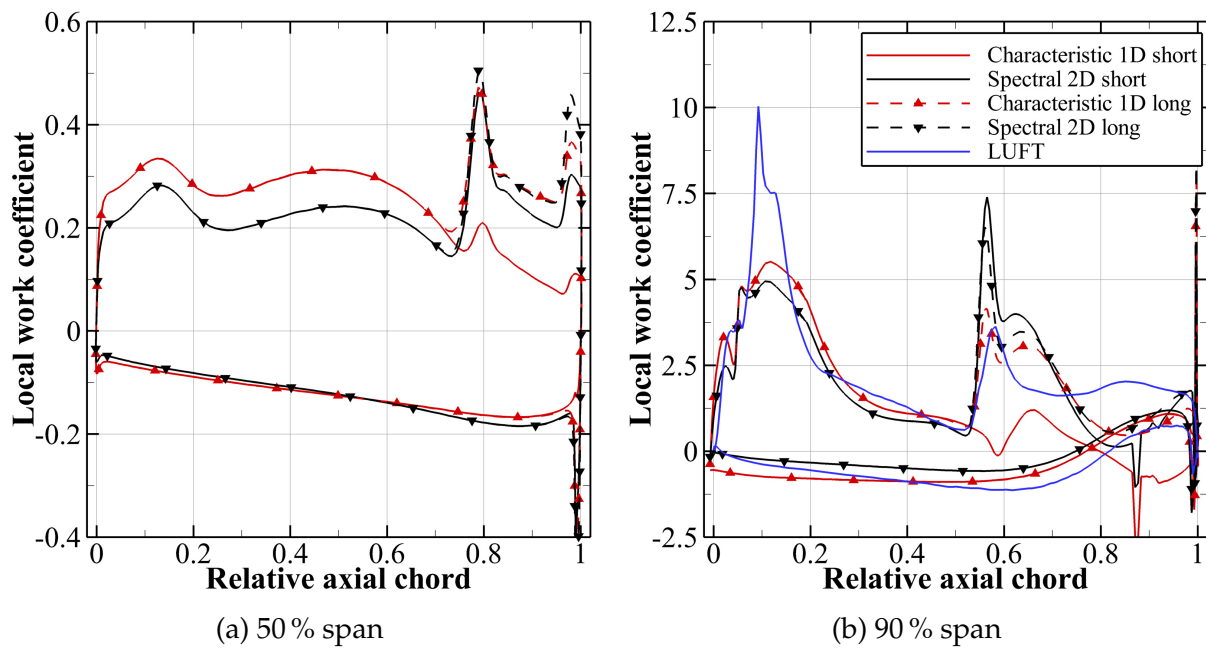
Figure 5.8: Local work coefficients at two radial positions ($\sigma = -45°$).

To compare this observation with the references, the local work coefficient

$$w = \frac{dW_{aero}/dA}{\pi \alpha^2 \, c \, p_{dyn}}. \tag{5.1}$$

with W_{aero} according to Equation (4.4) is introduced. Figure 5.8 shows the local work coefficient at 50% and 90% relative span. Several conclusions can be drawn from this figure: Firstly, the solutions, apart from the result with the short domain and one-dimensional NRBC, agree qualitatively with the LUFT results at 90% span. The largest differences occur close to the suction side's leading and trailing edges. Sun *et al.* (2017) investigate the impact of the tip clearance. They observe that including the tip gap causes the front peak to be flattened. Unlike the present work, which includes the original tip gap, Sun et al. compare a downsized gap of 0.25 % relative span and a model without tip gap. Thus, the effects of the tip gap can be expected to be stronger in the present work and the smaller work coefficient in the leading edge region in this work possibly results from the larger tip gap model. In a succeeding article, Sun *et al.* (2019) study the tip gap flow by means of URANS and detached eddy simulations. While the development of the tip gap vortex in stream-wise direction differs significantly depending on the representation of turbulence, both simulation approaches show good agreement in the front section of the tip region supporting the validity of the statement drawn from Sun *et al.* (2017). Additionally, it has been observed (see Section 5.1.5) that time-linearized methods produce a stronger peak at the leading edge close to the tip gap compared to nonlinear time or frequency domain methods independently of turbulence modelling. This might as well explain deviations from the (time-linearized) LUFT solutions.

The larger peak in the present solutions at 55% chord length, where the neighbouring blade's trailing edge shock hits the suction side, is related to the observation from the steady results, that the pressure rise due to the impinging shock is predicted stronger than by the LUFT results. This, again, is probably related to the finer mesh used in this work. The solution with the short domain and one-dimensional NRBC, however, deviates especially in this region from the other TRACE results.

Moreover, the work coefficient distributions at both radial positions reveal that the solution upstream of the shock impingement position is independent of the exit position and hence not affected by possible reflections from the outlet as the supersonic flow in front of the shock prevents the propagation of upstream travelling disturbances beyond the shock position. However, in the front region, the work coefficient varies with the inflow boundary method, yet to a smaller extent. Note that the rotor inlet position is constant for all simulations. Thus, the solutions obtained with the long and the short domains coincide in the front region.

In the following, we will study the acoustic mode generated by the blade motion with the corresponding frequency and a non-dimensional circumferential wavenumber of $m = -8.125$. Figure 5.9a plots the pressure amplitude of this wave at the inlet boundary depending on the radial position. This mode can be decomposed into fundamental waves by means of the same two-dimensional wave splitting approach used for the spectral NRBC. It should be emphasized that this analysis is simplified and does not correctly describe possible radial modes. Therefore, it only serves to give a certain estimation, but not a quantitatively precise evaluation of the real upstream and downstream propagating modes. The contribution of the incoming, downstream propagating acoustic mode is depicted in Figure 5.9b. As expected, the amplitude of the incoming acoustic mode equals zero when using the spectral boundary conditions.
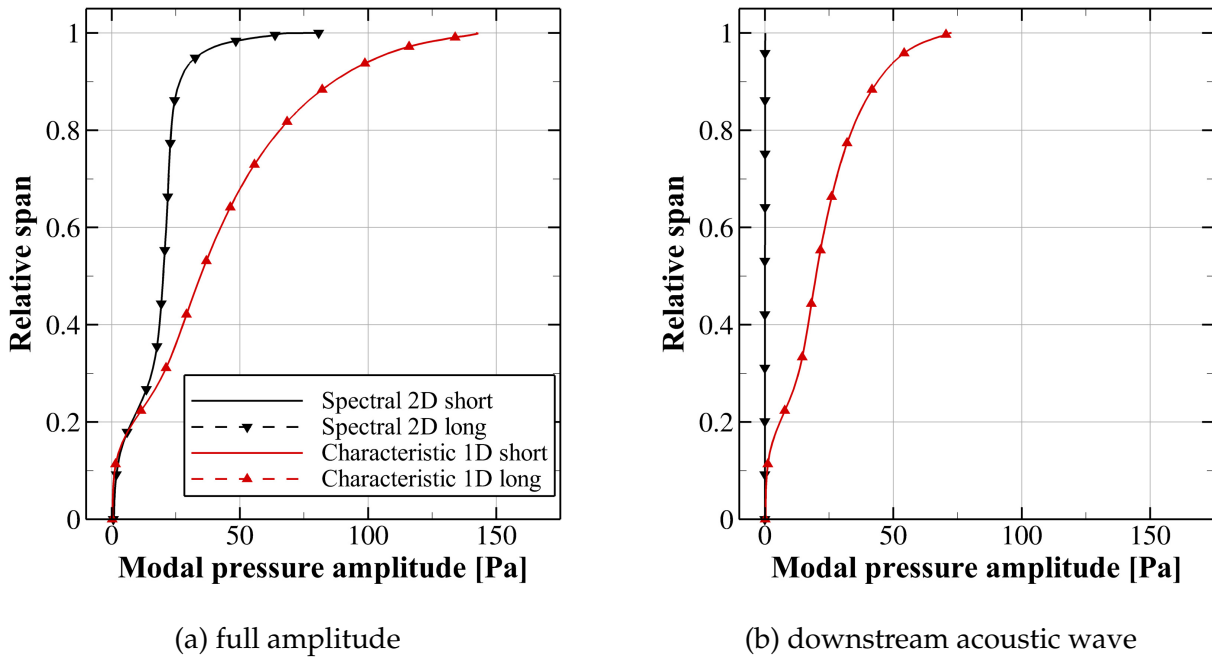
(a) full amplitude   (b) downstream acoustic wave

Figure 5.9: Pressure amplitude of blade vibration induced mode along span at rotor inlet ($\sigma = -45°$).
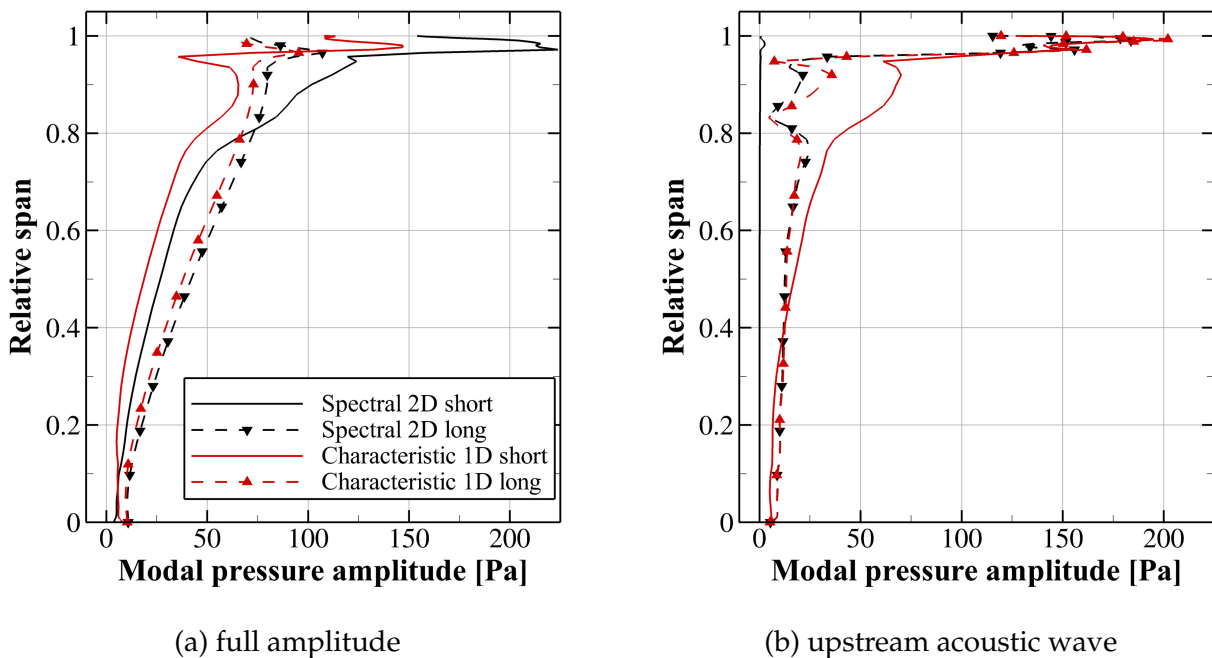

(a) full amplitude   (b) upstream acoustic wave

Figure 5.10: Pressure amplitude of blade vibration induced mode along span at rotor outlet ($\sigma = -45°$).

The discrepancy in Figure 5.9a between the solutions using the spectral 2D NRBC and the characteristic 1D NRBC is consistent with the amplitude of the incoming acoustic mode of the characteristic 1D NRBC. This indicates that the differences of the local work coefficient in the front region can be attributed to numerical reflections from the inlet boundary.

The same analysis is performed at the rotor outlet plane and shown in Figure 5.10. Both the long and the short mesh results are evaluated at the short rotor outlet plane. The analysis yields findings similar to the ones from the inflow boundary. Furthermore, it shows the impact of the outlet boundary position. There is a considerably stronger incoming wave in the outer 25% span region when one-dimensional NRBC are applied on the short mesh. Additionally, one observes that the tip leakage vortex produces strong perturbations close to the casing. Such three-dimensional, nonlinear perturbations cannot be correctly dealt with by both boundary condition methods. Figure 5.10b exhibits a relatively weak, but significant incoming wave for the long domain simulations. As its amplitude is approximately constant over the whole span, it is supposed that this mode does not stem directly from the blade motion because, unlike the amplitude in pressure, the blade displacement is approximately proportional to the relative spanwise position. Further investigation is needed to clarify which of the following possible reasons is responsible for this observation. Firstly, the circumferential Fourier decomposition is not corrected for the residual grid motion at the short rotor outlet as the imposed grid motion decays from the blade to the actual outlet boundary at the diffuser exit. Thus, this might be a pure postprocessing artefact. Another possible explanation is that there is a true three-dimensional interaction of the diffuser geometry with the original downstream travelling acoustic mode from the blade. Beyond, the upstream wave could be an artificial reflection from the outlet boundary as the prerequisites of the boundary condition theory are not strictly fulfilled. However, the one-dimensional and the two-dimensional NRBC produce consistent incoming perturbations which seems unlikely regarding the substantial differences in the formulation of both boundary conditions.
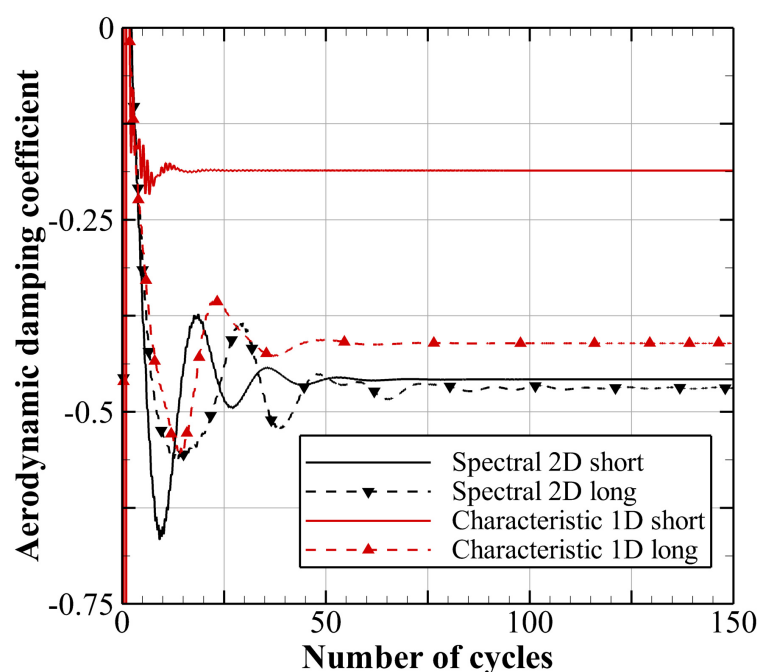
Figure 5.11: Temporal development of integral damping ($\sigma = -45°$).

5.1.4 Convergence and computational costs

Figure 5.11 plots the temporal development of integral damping over time for an IBPA of $-45°$. The spectral NRBC need about twice as many time steps to converge as the one-dimensional boundary conditions. This is due to the fact, that the spectral NRBC depend on the temporal Fourier coefficients of the boundary solution, which themselves converge rather slowly in phase lag simulations. However, there are no stability issues related to the boundary conditions in this study.

Furthermore, the reduced reflections of spectral NRBC allow shorter domains. The possibility to use shorter domains, in turn, reduces the number of time steps required for convergence as one can infer from Figure 5.11. In this case, the spectral NRBC applied on the short domain and the one-dimensional NRBC along with the long domain take roughly the same number of time steps to reach convergence and comparably accurate damping predictions. Note that the long mesh comprises more cells and, hence, demands more computational resources if the run time is to be kept constant. On the other hand, the more complex spectral NRBC enlarge the computational effort of the boundary treatment. However, throughout all computations carried out in this work, the run time per time step of simulations using spectral NRBC is increased by only 0.5-1.5% compared to the computations with one-dimensional boundary conditions while all other parameters are kept constant. Therefore, there is no clear answer to the question which boundary method is favourable if solely the computational effort is considered. Altogether, the computational costs of unsteady time domain simulations using spectral boundary conditions remain comparable to the costs of simulations using characteristic boundary conditions.

5.1.5 Comparison to frequency domain methods

With the development of robust spectral NRBCs for time domain simulations presented in this thesis and the advancing progress towards a mature harmonic balance solver to tackle industry relevant turbomachinery problems, the TRACE code offers, to the author's knowledge, a unique capability to simulate unsteady turbomachinery flows based on either linear or nonlinear frequency domain approaches as well as on conventional time marching methods with a very high level of consistency regarding spatial discretization techniques, state-of-the-art turbulence and transition modelling and non-reflecting boundary conditions. While the comparability of time and frequency domain methods is often subject to uncertainties regarding the inconsistencies of these numerical methods and physical models, a true apples-with-apples comparison is now feasible with TRACE. Thus, Frey *et al.* (2019), with participation of the author of this thesis, analyse the sources of the remaining variations in solutions from different approaches of capturing unsteady flow phenomena based on the same steam turbine flutter configuration.

Aside from cost and runtime considerations, the central outcome in a nutshell is showcased in Figure 5.12. The overall agreement of results obtained with different solution approaches is very good. Note that the time domain result is not identical to the results from this work as Frey *et al.* (2019) consider a reduced tip gap size in order to stabilize the frequency domain simulations, in particular the time-linearized solver.

The largest contribution to the difference in global damping between time-linearized and nonlinear time or frequency domain solutions can be attributed to the choice of reference plane for the 2D spectral NRBCs (cf. Section 3.2.1). While being implemented
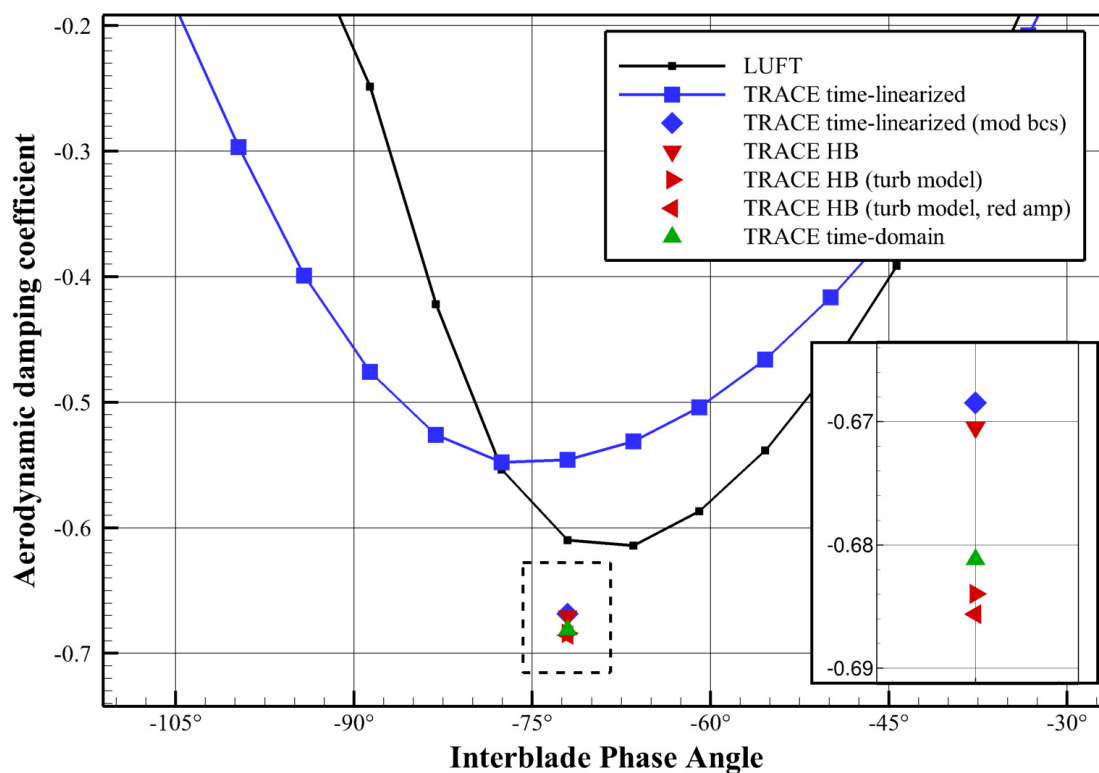
Figure 5.12: Detail of damping curve comparing different modelling approaches in the vicinity of maximum excitation ($\sigma = -72°$), adapted from Frey *et al.* (2019).

such that the reference plane can be adjusted by the user, the default reference plane in TRACE is only based on the circumferentially averaged meridional velocity if the time-mean flow is constant, e.g. in the linear solver. If the background flow is part of the solution, i.e. in time domain simulations or in harmonic balance computations that allow for a variable zeroth harmonic, it is beneficial from our experience to rather use the boundary-normal definition of the reference plane for stability reasons. The addition "mod bcs", therefore, refers to the time-linearized solution using the boundary-normal NRBC formulation analogously to the nonlinear results. This solution is in very close agreement to the harmonic balance solution that does not include the turbulence model in its harmonic solution, i.e. the effect of turbulence is assumed to only depend on the time-averaged mean flow disregarding any coupling of unsteady flow phenomena and local eddy viscosity. This constant eddy viscosity simplification is made in the time-linearized solver as well. If the turbulence model is accounted for in the harmonic balance solver, i.e. if the transport equations are part of the harmonic solution, then the harmonic balance solution is in very good agreement with the nonlinear time domain solution.

Furthermore, reducing the blade's bending amplitude by factor 4 yields a virtually identical non-dimensional damping value based on a harmonic balance simulation with unsteady turbulence modelling. From this, we can conclude that the amplitude used to predict flutter onset is still in the realm of linear aerodynamic response (under the assumption that the reduced tip gap does not fundamentally affect the validity of this finding).

Yet, the conclusions from Fig. 5.12 regarding the excellent agreement of linear and nonlinear methods refer to integral damping only. The full paper shows, that the time-linearized solver predicts a strong peak in aerodynamic work in the tip leading edge

region similar to the observation in Fig. 5.8. The time domain solution and the harmonic balance solution with and without unsteady turbulence modelling on the other hand do not exhibit this strong peak. However, these discrepancies are locally confined. In this region, the flow cannot be expected to behave in a linear fashion due to e.g. transonic effects and the tip gap vortex.

5.2 Compressor blade row interaction

5.2.1 Test case design and numerical setup

The second application of the spectral NRBC to real-world turbomachinery flows is based on DLR's Rig250, which represents the front stages of a modern, highly loaded compressor. The entire compressor comprises four stages plus a variable inlet guide vane with the first two stages being transonic. Its layout is outlined in Figure 5.13 including blade counts.

Row Name	Strut	IGV	R1	S1	R2	S2	R3	S3	R4	S4
Blade Count	7	40	23	36	28	48	38	68	47	80
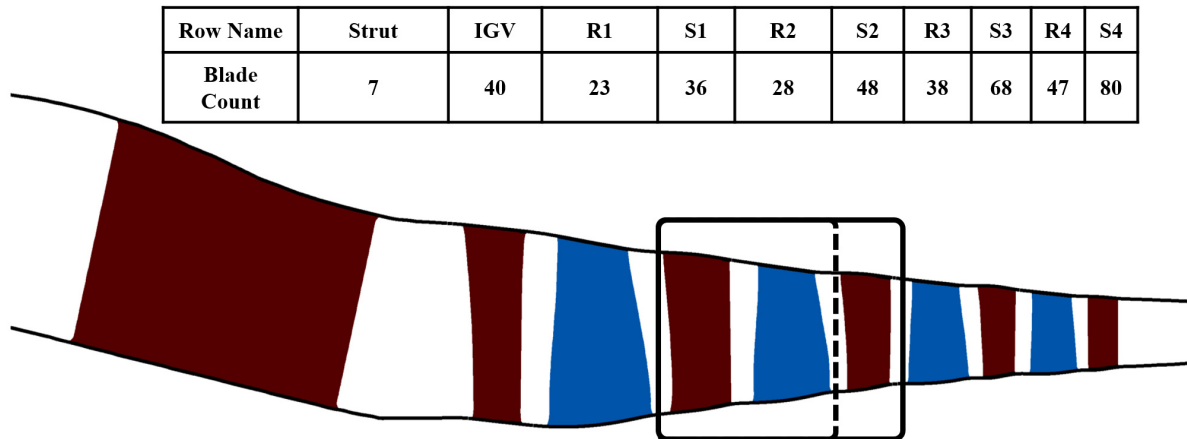
Figure 5.13: Outline of DLR's compressor Rig250 with blade row designations and blade counts. Rotor blades are coloured blue. Black boxes show computational domains used in this work.

The purpose of this test case is to demonstrate the prediction of unsteady, transonic blade row interactions with truncated computational domains which comprise only the blade rows of interest rather than the whole compressor or possibly additional duct segments or buffer zones in order to mitigate the influence of spurious, numerical reflections. In this case, the interaction of stator 1 and rotor 2 is examined with regard to unsteady blade pressure distributions. Although no aeroelastic evaluation is presented, this can be viewed as an example of a forced response (or high cycle fatigue) analysis since the prediction of unsteady blade pressure distributions is vital to the calculation of aerodynamic forcing.

Two objectives can be pursued with this choice of blades rows. In a first step, a comparison to available reference data of stator 1 is presented in Section 5.2.3. These reference data include both experimental blade pressure measurements and CFD data from very costly and time-consuming full annulus simulations of the first two stages including the IGV as well as the swan neck and strut section (see Reutter *et al.*, 2018). As this CFD setup has several blade rows between stator 1 and the artificial inlet and outlet boundaries, the impact of possible, numerical reflections on the region of interest is very small.

The second part deals with the unsteady pressure distribution on rotor 2 which is more demanding with regards to non-reflecting boundary conditions as shown in Sections 5.2.4 and following. It is demonstrated that an accurate prediction of unsteady blade pressure requires the use of a suitable non-reflecting boundary condition when no additional blade rows are kept in the computational domain. For this purpose, time

domain simulations with the spectral, two-dimensional and the characteristic, one-dimensional NRBCs are performed. Reference results for the assessment of those computations are obtained from an additional computation on an extended domain with the spectral, two-dimensional NRBC, including also the stator 2 downstream of rotor 2 (see Fig. 5.13).

Furthermore, the test case shows that the harmonic balance method and time domain simulations produce consistent results when using consistent NRBCs. This is an important result because the availability of spectral, two-dimensional NRBCs in the time domain solver is deemed a crucial aspect of time domain simulations being a consistent, high-fidelity tool for the validation, backup or complement to the harmonic balance method, which represents a cost-effective reduced-order method (see Chapter 1.1).

The study considers a single operating point characterized by a total pressure ratio of 5.2 and a reduced mass flow of 47 kg/s at nominal shaft speed. These conditions are close to the aerodynamic design point. The boundary values for the blade rows of interest are extracted from flux-averaged, radial distributions of a steady-state precursor simulation of the entire compressor which is based on boundary conditions from rig tests. All unsteady computations are initialized with the steady-state flow solution.

The time domain simulations with the shorter domain (S1-R2) as well as all HB computations are carried out as single-passage computations with phase-shifted periodic boundary conditions while a multi-passage mesh is used for the time domain simulation with the extended domain (S1-R2-S2). With the given blade counts, truly periodic boundary conditions are realized with a 90° segment comprising 9, 7 and 12 blades of each row, respectively. On the one hand, the multi-passage computation becomes necessary as phase-shifted boundaries are only available for time domain simulations with a single base frequency in TRACE, which prevents their application to configurations with more than two blade rows (unless scaling or favourable blade counts allow for coincident blade passing frequencies). On the other hand, thereby an application of the spectral NRBC with both phase-shifted boundaries and a multi-passage setup in one test case is demonstrated.

Time integration is performed by means of an implicit Crank-Nicolson scheme with pseudo-time stepping (see Crank & Nicolson, 1947; Ashcroft *et al.*, 2013). Single passage (phase-lag) simulations resolve the blade interaction frequency with 72 time steps. Correspondingly, 648 time steps are used to describe one passing of the quarter annulus segment in the multi-passage simulation, such that the BPF of S1 is resolved with 72 time steps in the R2 system. For each physical time step, 40 pseudo-time subiterations are carried out.

The two row HB computations incorporate the mean flow and four harmonics of the respective blade interaction modes. In the HB computation with the additional S2 row, the harmonic sets of S1 and R2 remain unchanged, i.e. the upstream effect of the S2 potential field is disregarded. The harmonic set of S2 is set up such that a specific mode from the S1-R2 interaction is matched instead of the R2 wake modes. This mode has a nodal diameter of 64 at S1 BPF in the frame of reference of R2 and translates to a mode of equal nodal diameter with the R2 BPF in the stationary frame of reference (or in other words having an IBPA of -120° with respect to S2). The frequency shift is due to the Doppler effect when a mode is observed from different frames of reference with relative rotational motion to each other. Further explanation and the mathematical description can be found in Junge *et al.* (2015). The mean solution and four harmonics of the mode described above are resolved in the S2 row. The reason for resolving this
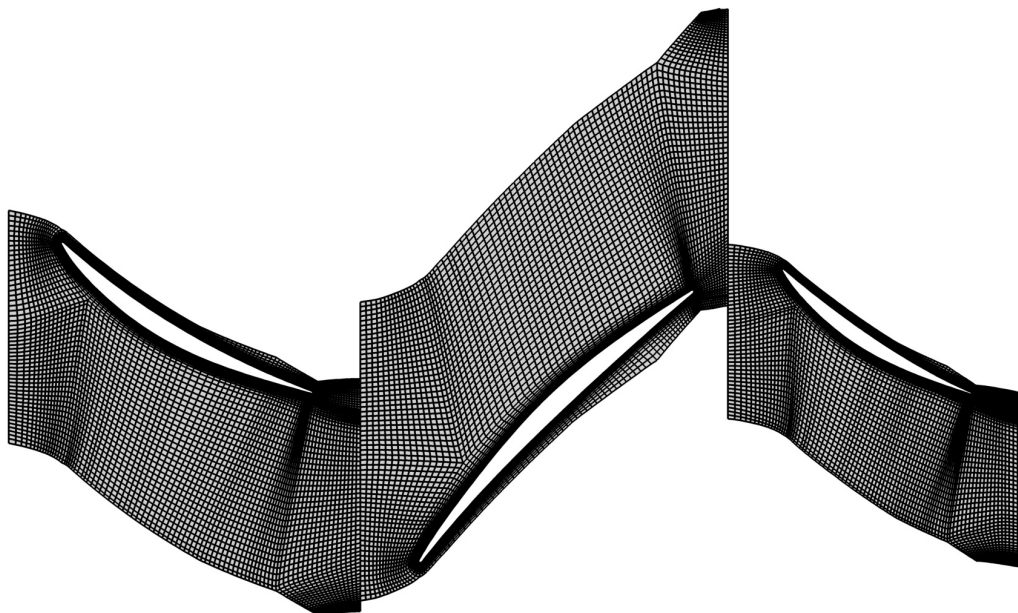
Figure 5.14: Blade-to-blade cut of the computational mesh at mid-span, every second grid line shown.

mode will become clearer in Sections 5.2.5 and following. This HB computation will be used to help explain differences between the time domain solutions obtained with the short and long domains. All HB computations employ the HB implementation of the spectral, two-dimensional NRBC at inlets, outlets and blade row interfaces.

Figure 5.14 depicts a mid-span cut through the computational mesh (coarsened by factor two in the picture), which is identical on individual blade level to the one used and described by Reutter *et al.* (2018). It comprises 5.04M (S1), 4.92M (R2) and 4.55M (S2) cells per blade, totalling 134.7M cells for the S1-R2-S2 multi-passage mesh (in comparison to nearly one billion cells in the full annulus computation presented by Reutter). Solid walls are modelled with the low-Reynolds approach and an average wall-normal cell size of $y^+ \approx 1$.

All boundary layers are regarded as fully turbulent without transition modelling. The (U)RANS equations are closed employing the two equation k-ω model by Wilcox (1988) with extensions for the stagnation point anomaly (see Kato & Launder, 1993) and effects of rotating flows (see Bardina *et al.*, 1985). This turbulence model is consistent with Reutter's setup. For robustness reasons, the HB computations solve the turbulence model equations for the mean flow solution only, producing a temporally invariant eddy viscosity field.

5.2.2   Mean Flow

Figure 5.15 shows the time-averaged blade pressure distribution on stator 1 and rotor 2 at 50 % relative span. For stator 1, time domain and harmonic balance computations with the spectral, two-dimensional boundary conditions show excellent agreement with each other as well as with Reutter's full annulus computation. The solution obtained with the characteristic, one-dimensional boundary condition exhibits a slightly reduced pressure level along the pressure side and the also along the suction side except for the first 10 % of axial chord. The flow accelerates slower resulting in down-

(a) Stator 1   (b) Rotor 2
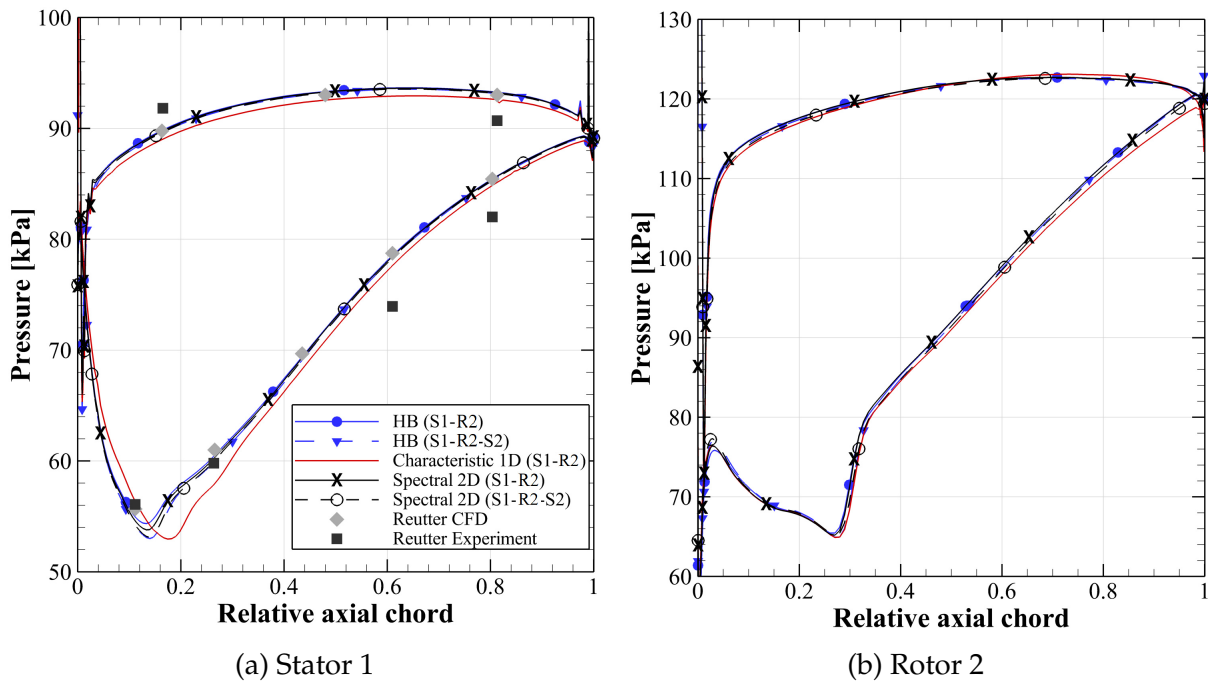
Figure 5.15: Time-mean blade pressure distributions at mid-span.

stream shift of the suction peak by about 5 % axial chord compared to the solutions obtained with the spectral NRBC. For reference, the peak Mach number in the three-dimensional flow field is found to be about 1.05 in the vicinity of this blade surface region. Altogether, differences between the numerical solutions are small.

The agreement with rig test results is generally satisfactory, but varies along the blade. While in particular the numerical solutions with the spectral NRBC match the measurements very well in the first half of the suction side, the latter present a reduced pressure build-up towards the trailing edge on the suction and pressure side.

However, the excellent correspondence of the computations presented in this work to the numerical references by Reutter et al. is the central finding with regards to validating boundary conditions since the numerical results obtained with the reduced domain can ideally meet the results obtained from a full annulus, multi-stage computation with otherwise consistent models and numerical parameters.

The disparity of CFD and rig test results can generally be rooted in a variety of causes that are beyond the scope of this work. These can be the use of the (U)RANS equations with respective turbulence, transition and gas modelling, simplification and idealization of the real world geometry (including intrusive measurement equipment), uncertainties and assumptions regarding boundary conditions (in this case boundary values, not numerical boundary condition methods for the underlying differential equations), numerical dissipation and dispersion and measurement uncertainties to name just the most important, usual suspects.

Reference results of rotor 2 are not available. Here, all flow solutions predict an almost coincident mean blade pressure distribution with a clearly discernible shock at about 30 % normalized axial chord. The solution obtained with the characteristic, one-dimensional boundary condition presents the most significant deviations from all other solutions, but the overall agreement can still be considered very good.

5.2.3 Unsteady blade pressure: Stator 1
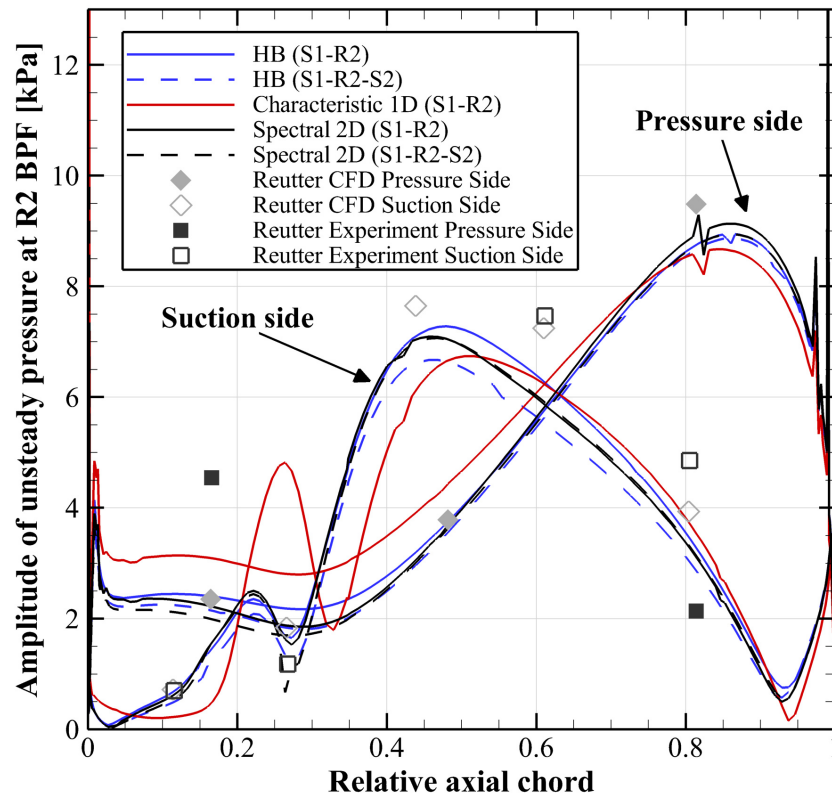
Figure 5.16: Unsteady blade pressure amplitudes on stator 1 at 50 % span .

In the following, the unsteady pressure field is analysed beginning with stator 1. Amplitudes of pressure fluctuations with the blade passing frequency of rotor 2 at 50 % relative span are plotted in Figure 5.16.

Again the pressure fields predicted by all computations with the spectral NRBC are in very good agreement with each other while the characteristic boundary condition leads to a qualitatively similar, yet significantly different unsteady blade pressure. The inlet boundary is located immediately upstream of this blade row and, thus, the variations stemming from different boundary condition methods are more prominent in the front section of the blade. Here, the characteristic boundary condition produces about 30-50 % larger pressure amplitudes on the pressure side. The front section of the suction side is to some extent shielded from upstream travelling perturbations associated with the S1-R2 interaction as the flow reaches transonic conditions in the suction peak region. Hence, only relatively weak pressure fluctuations are observed here. All flow solutions exhibit a peak followed by a local minimum in the area of sonic flow conditions. These local extrema are much more pronounced with the characteristic boundary condition.

The computations based on spectral boundary conditions correspond very well to the numerical results presented by Reutter *et al.* (2018) in the front part of the blade. In the rear half, the agreement is still sound although the reference solution predicts larger amplitudes throughout the rear part.

Numerical results by Reuter et al. as well as the ones with spectral NRBCs show good agreement with rig test data along the suction side, especially in the front area. Com-

pared to the calculations of this work, the slightly larger amplitudes found in Reutter's CFD data in the rear section appear to better reflect the rig test data although the limited number of data points and the varying degree of agreement does not allow a concluding assessment.

In contrast, the pressure-sided agreement of CFD and experiment is poor. The reasons for that remain unclear and are not addressed in the paper by Reutter et al. As this disparity is also evident in the full annulus computation with a much larger computational domain, it cannot be due to potential inaccuracy of the boundary condition method that are presented and examined in this work.

Although the characteristic boundary condition yields a qualitatively similar prediction of unsteady blade pressure, the analysis of unsteady pressure on stator 1 demonstrates that, by means of the spectral NRBC, a prediction can be achieved on a truncated domain that is almost equivalent with respect to this specific blade row interaction to the large-scale simulation of the whole compressor.

5.2.4   Unsteady blade pressure: Rotor 2
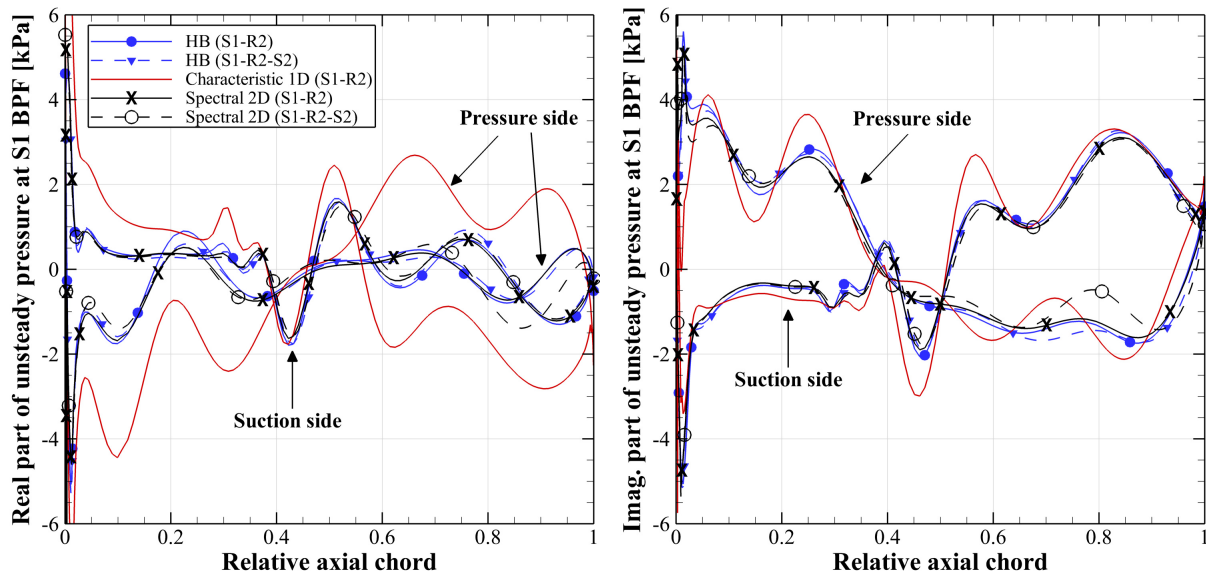
Figure 5.17: Blade surface distribution of complex unsteady pressure associated with S1 BPF on rotor 2 at mid-span.

Subsequently, the blade pressure resulting from the stator-rotor interaction on rotor 2 is studied in more detail. Figure 5.17 shows the complex-valued unsteady pressure at 50 % relative span.

In accordance with observations from the previous sections, the solutions with the spectral NRBC show excellent agreement for the majority of the surface while the solution with the characteristic boundary condition differs significantly along the entire chord. Overall, higher levels of unsteady pressure are found in particular in the vicinity of the leading and trailing edges when the latter boundary condition is employed. Moreover, local extrema are overestimated compared to the spectral NRBC solutions and partly offset towards mid-chord by up to 10 % relative axial chord, e.g. the double peak in the pressure-sided trailing edge region.
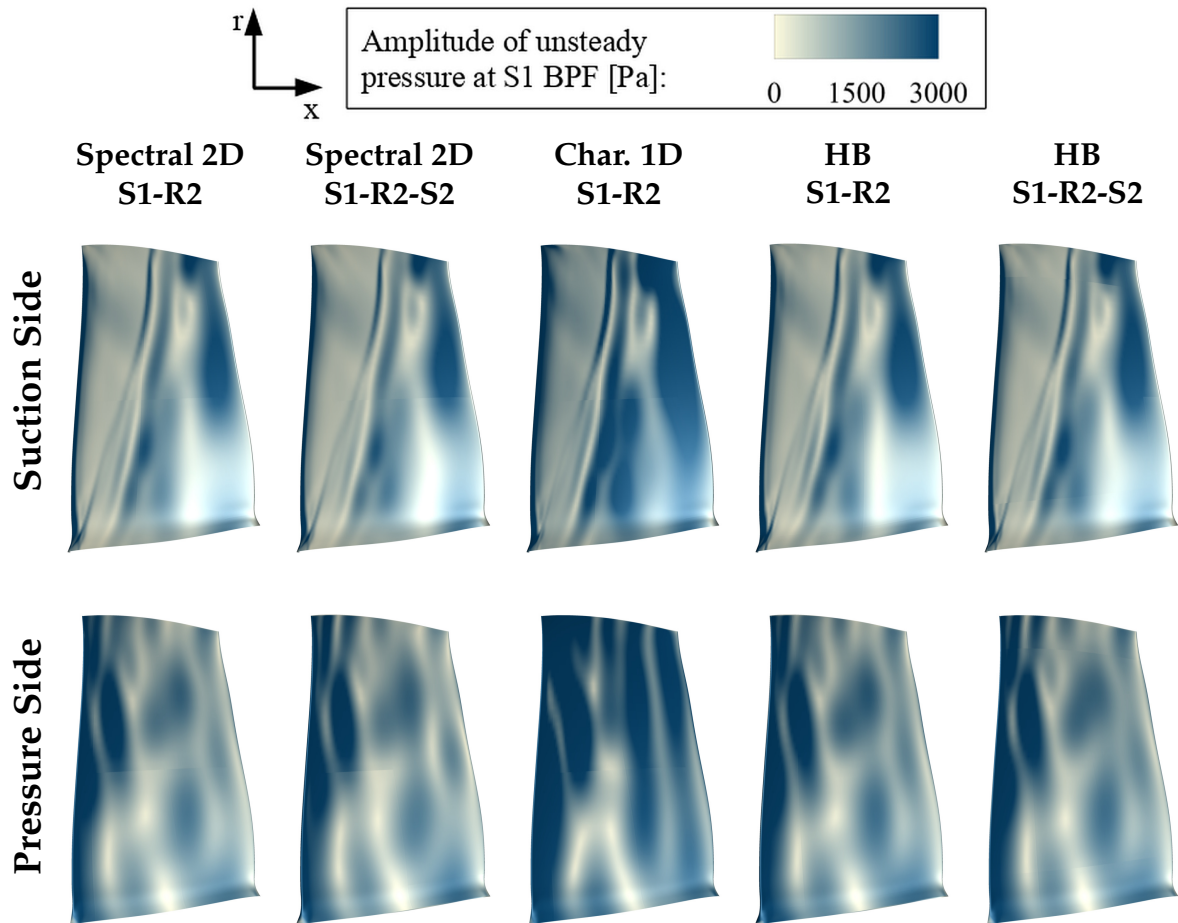
Figure 5.18: Blade surface distribution of unsteady pressure amplitudes associated with S1 BPF on rotor 2.

As these differences are more pronounced for the real part of the unsteady pressure, it should be noted that the unsteady blade pressure differs not only in magnitude but also in phase. Note that again only weak fluctuations are observed in the supersonic region of the suction side.

Local deviations between the results from time domain simulation of the S1-B2-S2 domain on the one hand and the time and frequency domain solutions with the spectral NRBC and the S1-B2 domain on the other hand are found in the trailing edge region of the pressure side. The HB solution of the extended domain also exhibits minor differences here, but corresponds much more closely to the short domain solutions. As the modal content resolved in the S2 row is limited to modes of certain circumferential periodicity when using HB, only the time domain simulation can be considered a reference solution in order to assess the reflection properties of the exit boundaries in the short domain computations. As the pressure side is oriented backwards, towards either the exit boundary or the downstream blade row, these local differences can be explained by incoming waves from downstream or the absence of those waves. Whether these waves are numerical artefacts in the short domain computations and the HB computation on the extended domain or physically explicable, will be discussed in the following sections.

However, in comparison to the differences observed when using the characteristic NRBC, the differences mentioned above are small and localized. Therefore, it can
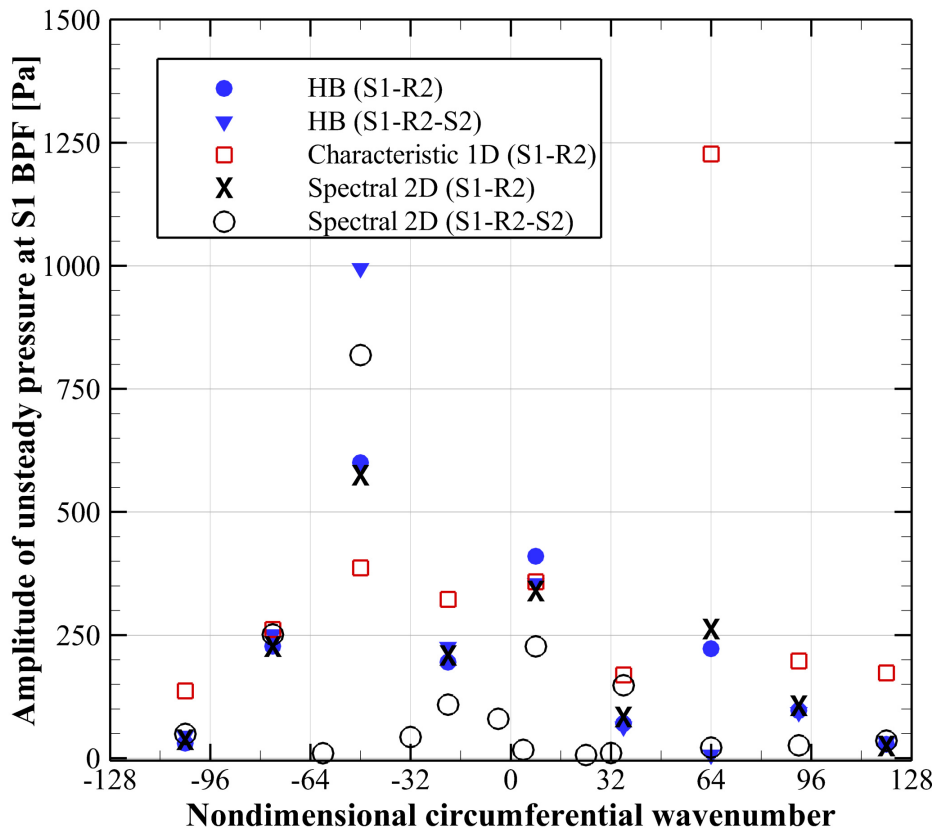
Figure 5.19: Circumferential decomposition of the pressure field at the exit boundary or blade row interface (50 % relative span).

be concluded that artificial reflections can drastically impair the prediction of the unsteady pressure field when the characteristic, one-dimensional boundary condition is used together with an exit plane in the vicinity of the region of interest. On the other hand, the non-reflecting properties of the spectral, two-dimensional boundary condition allow in this case to omit the subsequent blade row without a substantial loss of prediction accuracy.

Figure 5.18 shows the amplitude of unsteady pressure on the entire blade surface in order to indicate that the above observations are not limited to the mid-span cut, but apply to other radial positions as well. While all distributions obtained with the spectral NRBC appear almost indistinguishable, the characteristic boundary condition leads to regions of increased pressure amplitudes, in particular in the proximity of the trailing edge, in the transonic region on the suction side and in the pressure-sided leading edge area.

5.2.5   Modal decomposition

To further explore the impact of the boundary/interface flow field on the blade pressure, the unsteady pressure field at the exit boundary or the blade row interface (see dashed line in Fig. 5.13) is Fourier-decomposed along the circumference to identify modes of different circumferential periodicity, depicted in Figure 5.19.

Recall from Equation (3.67) that the wavenumber spectrum is determined by the circumferential periodicity of the computational model, depending on the pitch-wise ex-

tent of the computational domain and the (a priori specified) phase shift of the periodic boundaries. Therefore, the spectral resolution of the computations which are based on single-passage models, i.e. the S1-R2 time domain and both HB computations, is identical while the multi-passage time domain computation of the S1-R2-S2 domain yields a finer resolution. However, these additionally resolved wavenumbers do theoretically not carry any signal because of the perfectly periodic blade geometry and mesh. For the sake of clarity, modes with an amplitude smaller than 5 Pa have been blanked out and thereby only a few additional modes remain in the plot (e.g. at m = -32). All of these are small compared to the relevant modes resolved by the single-passage models.

Moreover, note that these circumferentially decomposed modes are used only for analysis purposes in the S1-R2-S2 time domain computation, as the sliding interface does not rely on spectral data but uses a local interpolation of flow states. This also applies to the time domain simulation with the characteristic, locally formulated boundary condition. In contrast, HB and short domain computations with the spectral boundary condition use the same spectral representation, as it is plotted here, as input to the wave decomposition presented in Section 3.2.2, either for the exit boundary (time domain and short HB computation) or for the modal row coupling in HB (S1-R2-S2 HB computation, see Frey *et al.* (2014); Junge *et al.* (2015) for a detailed description of the coupling technique).

The time domain and HB computations with the spectral NRBC and the S1-R2 domain present almost identical spectra. The amplitudes found in the solution of the characteristic boundary condition are larger than the aforementioned ones for most wavenumbers, the only exceptions being found at m = -76, where amplitudes match, and at m = -48, where the characteristic NRBC produces the smallest amplitude of all computations. Note that smaller, relative differences are observed for smaller circumferential wavenumbers. This is due to the fact that the characteristic approach is an approximation to the exact wave splitting operator, which is only exact for one-dimensional waves (dominant) and becomes less accurate with increasing absolute value of the circumferential wavenumber.

The degree of conformity of the solutions from the S1-R2-S2 domain with each other as well as with their S1-R2 domain counterparts is less consistent than the mutual agreement between the latter. For example, all solutions with the spectral NRBC exhibit similar amplitudes for wavenumbers -104, -76 or 120. On the other hand, at m = 8 and m = -20, the HB S1-R2-S2 computation agrees closely with the short domain computations, but the S1-R2-S2 time domain computation shows amplitudes reduced by about 50 %. In these cases, the former does not incorporate these modes in the set of modes resolved by this specific HB setup in the stator 2 row. Since the HB blade row interface acts like an exit boundary condition with respect to modes that are not resolved in the adjacent blade row, the observed agreement with short domain results is to be expected for such modes.

Conversely, the time domain computation including S2 is capable of rendering all modes in the S2 row that are already rendered in the rotor 2 row due to the identical circumferential periodicity with respect to a 90° segment. Therefore, it is the only computation in this study that can naturally represent all kinds of upstream effects of the second stator, including possible physical reflections from the blade surfaces or (possibly rather involved) mode scattering effects.

Although the previous section has shown that the impact of those phenomena is rather limited in the configuration considered here and that the R2 blade pressure is predicted with sufficient accuracy based on the truncated domain and the spectral NRBC, this
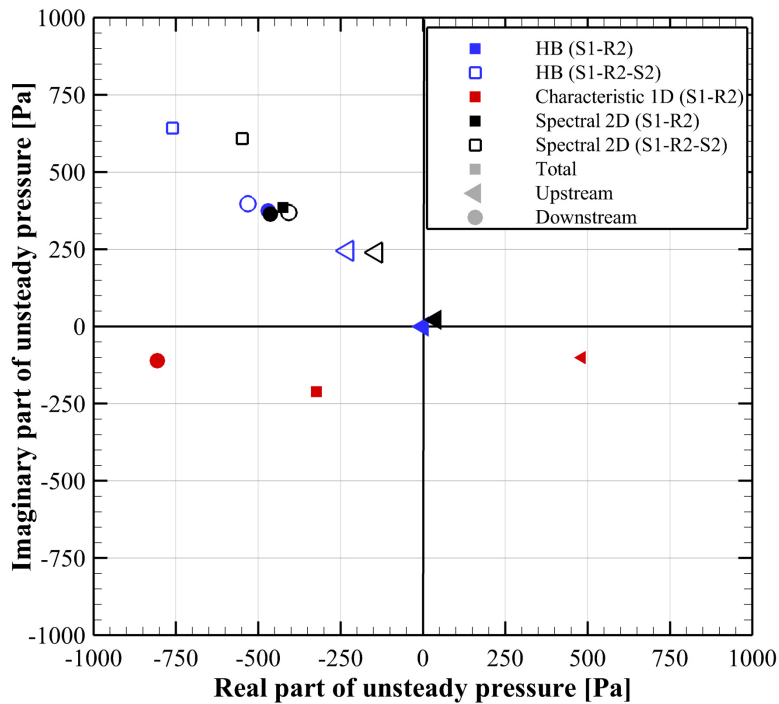
Figure 5.20: Decomposition of the m = -48 mode into upstream and downstream propagating components.

analysis underlines why the availability of high-quality time domain simulations is deemed important despite their large computational effort. Albeit it is feasible to resolve additional modes in the HB setup, this approach can become very sophisticated and quickly negate the cost advantage of the HB technique if all uncertainties about which modes need to be resolved are to be removed; even in a moderately complex three row configuration like this.

In the following, the analysis focuses on the two modes with wavenumbers -48 and 64 as these are, firstly, the most dominant ones and, secondly, they feature the most pronounced variance.

5.2.6   Tyler-Sofrin mode with upstream component

First, the mode associated with wavenumber -48 is examined. This mode is resolved in the S2 row in the respective HB computation. However, it must not be confused with the upstream effect of the potential field of this stator. Although the nodal diameter matches the blade count of stator 2, the stationary potential field of stator 2 is observed at the blade passing frequency associated with this stator in the rotor domain while our analysis deals with modes associated with the blade passing frequency of stator 1. Instead the origin of this mode is explicable with the theory of Tyler & Sofrin (1962) about the generation of tonal noise.

Figure 5.20 depicts Fourier coefficients of the unsteady pressure associated with this mode in the complex plane, shown as squares in the illustration. Additionally, the total amount is decomposed according to Equation (3.53) into modal amplitudes of upstream (triangles) and downstream (circles) travelling waves.

The figure shows that, for the short domain solutions with the spectral NRBC, the

mode observed at the exit represents a downstream travelling wave only. Therefore, the outgoing component and the total value coincide while the incoming component is located in the origin of the complex plane. This reflects the concept of the spectral NRBC.

In contrast, the solutions including stator 2 exhibit an additional incoming wave with about the same phase such that the overall magnitude of the mode is predicted larger than by the short domain computations. Since this mode is cut-on under the given flow conditions (see Eq. (3.44)), this incoming wave could be a reflection of the outgoing wave by the stator 2 blades. Alternatively, it could originate in the stator 2 row as the result of another mode being scattered. For our purpose, the exact generation mechanism does not matter. Either way, this is an example of an actual, physically explainable incoming mode that is neglected when using the short domain.

The slightly smaller amplitudes and the small, but uniform shift in phase of the S1-R2-S2 time domain computation compared to its HB counterpart could be due to the fact that time integration always produces some numerical dissipation and dispersion error.

The short domain solution produced by the characteristic boundary condition also presents an incoming wave. Yet, this incoming mode lacks any physical justification and must therefore be considered a spurious artefact. The incoming and outgoing waves are of considerably larger magnitude than the superposed wave since they display almost 180° phase difference. This means, although the total amplitude is smaller than the corresponding amplitudes of the S1-R2 computation with the two-dimensional NRBC, there is a relatively strong incoming mode caused by the one-dimensional boundary condition.

5.2.7   Wake mode

The results of the decomposition of the mode with wavenumber m = 64 into upstream and downstream propagating parts are shown in Figure 5.21. As the amplitude observed with the characteristic boundary condition is much larger, this computation is excluded from the plot for clarity in order to realize an adequate scale for the remaining data.

Again, we find a significant incoming contribution only if stator 2 is regarded. Otherwise, the S1-R2 solutions correspond to the outgoing waves of the solutions from the extended domain. In this case, however, the situation is different and this section discusses why the extended domain leads to a different solution although the difference is primarily caused by the boundary condition rather than by an upstream effect of stator 2.

The overall amplitude observed in the S1-R2-S2 solutions is very low and the incoming and outgoing contributions, as determined by the two-dimensional approach based on the linearized Euler equations, appear to almost completely cancel out each other. Since this mode is cut-off, this observation cannot be explained with an acoustic wave being perfectly reflected at the subsequent stator 2.

The existence of an upstream travelling mode, originating from the S2 blade row, either by mode scattering or as an independent Tyler-Sofrin mode, destructively interfering with a downstream propagating Tyler-Sofrin mode from the S1-R2 interaction, is theoretically possible. However, it is improbable that they cancel out each other almost perfectly.
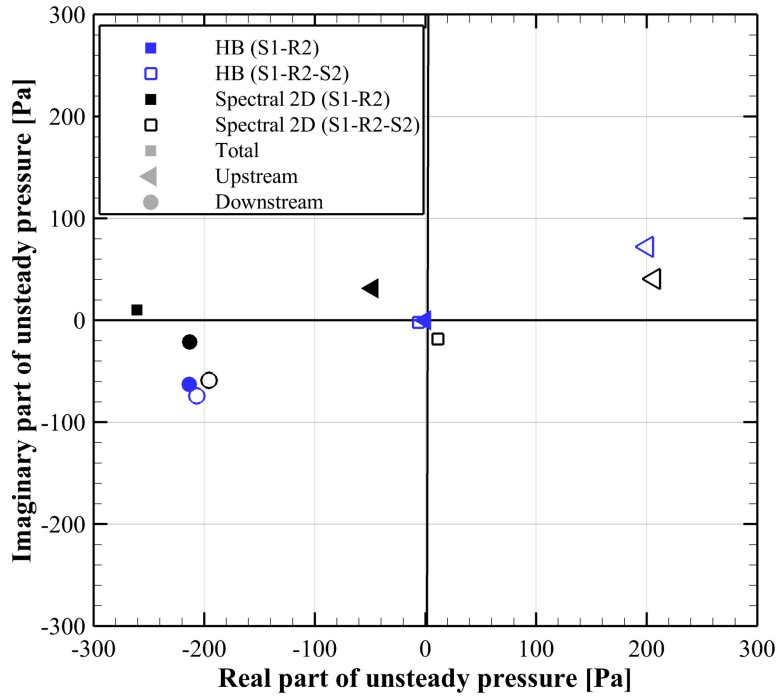
Figure 5.21: Decomposition of the m = 64 mode into upstream and downstream propagating components.

Moreover, Figure 5.22 shows that this situation can be found along the entire radial range of the interface. The plot shows the radial distribution of total amplitudes of each computation using the spectral NRBC and the upstream and downstream contributions of the S1-R2-S2 time domain computation. The other upstream and downstream parts are left out for clarity.

The overall pressure found in the short domain computations matches the outgoing portions of the long domain computations since the incoming waves are suppressed by the exit boundary condition in the short domain computations.

The S1-R2-S2 solutions from the time domain and the HB solver exhibit only small overall pressure amplitudes at all radial positions. Consequently, the upstream and downstream contributions of the HB solution closely follow their respective time domain equivalents (not shown here for clarity, but in accordance with the findings from Fig. 5.21).

As the flow field is three-dimensional and non-uniform in radial direction, it is virtually impossible that an independent upstream travelling mode from stator 2 corresponds to the downstream travelling mode from the S1-R2 interaction with equal magnitude and opposing phase along the entire radius.

In fact, this mode with a circumferential wavenumber of 64 is related to the pattern of wakes. The rotor wakes are observed as a stationary pattern in the rotor system and, therefore, they are primarily represented by the zeroth temporal harmonic rather than by the harmonic associated with the BPF of S1, which is considered in this analysis. Yet, as the rotor flow is subject to unsteady perturbations associated with the S1 BPF, the stationary rotor wake pattern oscillates at the same frequency. This means, in addition to the 36 convected wakes of stator 1, some signal stemming from the 28 rotor wakes can be found at S1 BPF as well.

Figure 5.23 depicts the real part of the Fourier-transformed eddy viscosity at the BPF
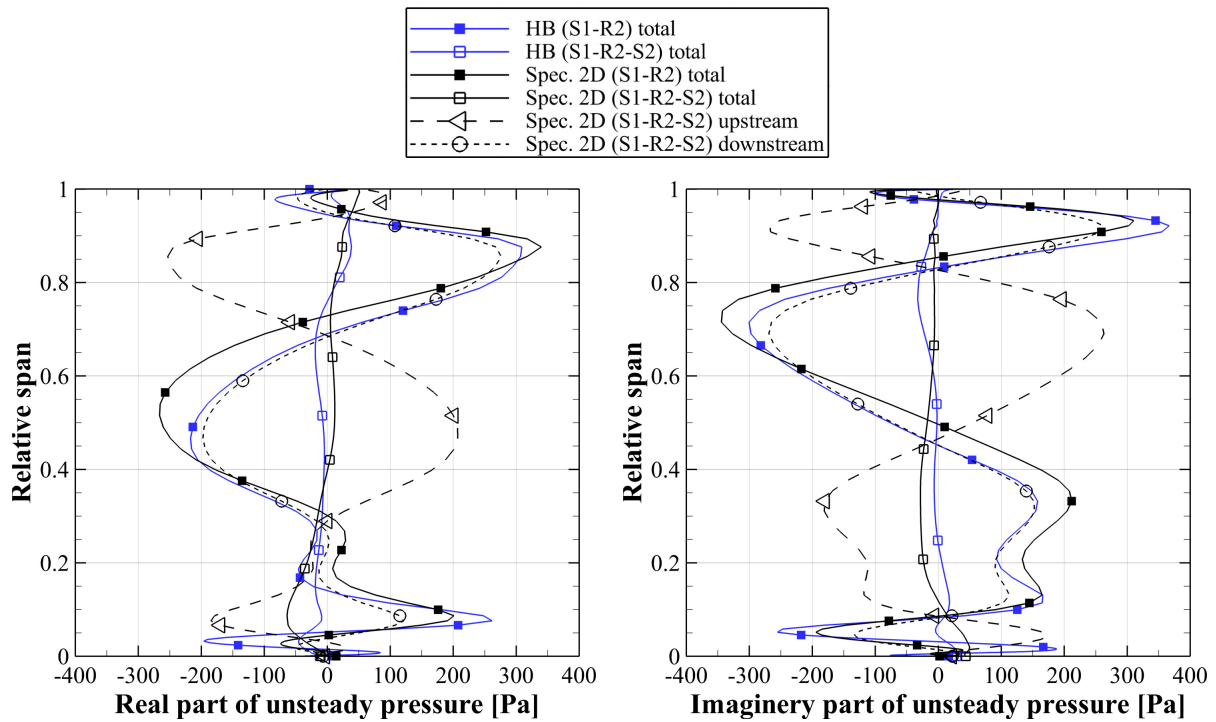
Figure 5.22: Radial distribution of complex pressure for the m = 64 mode at outlet plane of R2.

of stator 1 taken from the time domain simulation with the extended domain. Eddy viscosity itself does not play any role for the spectral NRBC as they are derived from the Euler equations. But eddy viscosity is closely linked with wakes, which represent entropy and vorticity modes in the context of spectral NRBCs. The latter are, however, more difficult to visualize distinctively.

Recall that the computational domain covers 90° degree in pitch-wise direction, i.e. one quarter of the full blade row. We can clearly identify 9 maxima and minima at the inlet of the blade row, corresponding to 36 incoming wakes of S1. At the outlet, however, we find a pattern of 16 maxima and minima, corresponding the mode discussed in this section with circumferential wavenumber 64.

Only in flows that can be described by the two-dimensional, linearized Euler equations with constant mean flow, the modal decomposition is exact such that convective and acoustic modes can actually be decoupled. Therefore, this procedure is only approximately accurate in complex, nonlinear turbomachinery flows. Since the combined pressure amplitude is small in the time domain solution including stator 2 and it was concluded that the small amplitude is not due to cancelling out of two opposite waves, the relatively high amplitudes of upstream and downstream travelling waves must be an artefact of the imperfect modal decomposition.

The fact that this limitation of the wave splitting approach is especially significant for this specific wavenumber associated with the wake pattern suggests two possible explanations. Firstly, the imperfect decoupling could be caused by viscosity effects. Secondly, this could be an example of nonlinear effects and a flow field that cannot be described correctly by superposition of plane wave solutions (cf. Eq. (3.31)) in constant background flow because the wake pattern with nodal diameter 64 does not spin uniformly along the circumference. Only the 36 wakes of stator 1 move continuously along in circumferential direction. While the positions of the 28 wakes associated with
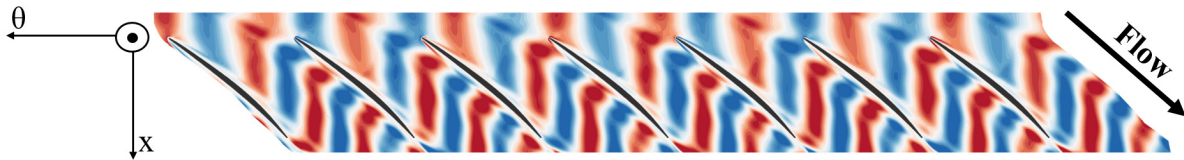
Figure 5.23: Real part of unsteady eddy viscosity field in the R2 blade row at BPF of S1. Cut at 50 % relative span. Positive values coloured red, negative values blue.

the rotor remain stationary in the rotating frame of reference, the local fluctuation of these wakes is synchronous with the relative motion of stator 1. Therefore, the overall signal with S1 BPF and circumferential wavenumber 64 does not correspond to a single, plane wave as assumed when deriving the dispersion relation and its eigenvector decomposition.

As mentioned above, the sliding interface in this computation is independent of the modal decomposition approach. Here, this is only a postprocessing matter while the wave splitting approach is a cornerstone to both the exit boundary condition of the short domain computation and to the modal blade row coupling approach of the HB solver.

This explains why the solutions of the S1-R2 model differ from their S1-R2-S2 counterparts. The exit boundary conditions falsely identifies an upstream and a downstream travelling acoustic wave induced by the wake pattern, but suppresses the incoming, upstream propagating portion, resulting in a considerably stronger total modal pressure amplitude at m = 64 in the wavenumber spectrum.

In the HB computation including the S2 row, both the upstream and downstream propagating (spurious) waves occur because the respective mode is resolved in the S2 domain. Hence, the interface algorithm suppresses neither of the two waves and, by superposition, the interface flow field is reconstructed such that it corresponds to the one observed at the sliding interface of the time domain computation.

The one-dimensional, characteristic NRBC does not rely on the modal decomposition in spectral space. Recall from Section 3.3.1 that the calculation of characteristic variables is, nevertheless, a simplification of the spectral wave splitting approach. Thus, the characteristic boundary condition is even less accurate at decoupling acoustic and and convective perturbations that do not propagate perpendicularly to the boundary. Therefore, a strong wake-induced reflection is produced leading to the strong artificial pressure amplitude found in Figure 5.19.

For the sake of completeness, it should be noted that the above analysis does not imply that there is no Tyler-Sofrin mode with this wavenumber. However, three reasons suggest that its impact is small compared to the effect described above. First, the observed overall pressure amplitude of this mode is relatively small in the reference time domain computation including stator 2. Second, this mode is cut-off. Third, the variance among the different computations is considerably more pronounced for this particular wavenumber indicating that the effect of the wake plays the dominant role here.

To conclude, it must be emphasized that, when employing the spectral NRBC, the impact of local differences at the boundary, found in the modal analysis in this and the preceding sections, on the unsteady blade pressure distribution is small as discussed in Section 5.2.4. In contrast, using the one-dimensional, characteristic boundary condition yields a significantly different solution.

6 Summary and Outlook

A spectral, two-dimensional non-reflecting boundary condition for unsteady, time-marching flow computations has been implemented into DLR's turbomachinery CFD solver TRACE and applied to five different test cases of increasing complexity. It was found that the NRBC provides significantly improved accuracy, i.e. suppression of artificial reflections, compared to existing boundary conditions for time domain simulations while good overall stability and convergence properties allow for a wide utilization in real-world turbomachinery research and design scenarios.

Therefore, this work contributes to meeting the growing demand for accurate simulations of unsteady turbomachinery flow phenomena. Time domain URANS simulations are commonly considered the highest (feasible) level of turbomachinery flow simulation because, in contrast to frequency domain methods, they involve no further simplifications or assumptions. However, frequency domain methods often employ superior NRBC formulations. The present work closes this gap. The approach for the NRBC presented in this thesis has been chosen because linear and nonlinear frequency domain methods have been employing this type of of boundary condition successfully since the emergence of frequency domain methods in turbomachinery CFD. Unfortunately, these boundary conditions are not only non-local in space, but also in time because they rely on a modal representation of the boundary flow field. This results in additional difficulty for the implementation into time domain simulation methods.

Thus, approximate NRBC have usually been used for time domain simulations so far, not only in TRACE, but also in the literature. Apart from accuracy improvements for the time domain solver, a consistent method for time and frequency domain simulations is deemed highly valuable because it enables the parallel use and comparability of time and frequency domain methods such that they complement each other with their respective strengths and weaknesses.

A thorough description of the theory and implementation has been presented. The NRBC are derived from the two-dimensional, linearized Euler equations. In this context, they are exact. For three-dimensional flows, they are applied using a quasi-three-dimensional approach. Therefore, one cannot expect them to be perfectly non-reflecting in nonlinear, three-dimensional flows. The section about implementation details emphasizes aspects that are specific to the adaption of the spectral NRBC to time domain simulations. These include

- the transient calculation of the necessary temporal Fourier transform of the boundary flow field,

- the formulation of the NRBC in terms of characteric variables with suitable relaxation of incoming characteristics,

- distinguishing between updates of the boundary flow field with respect to pseudo-time and phyisical time,

- an exceptional, local handling of waves with wave fronts parallel to the boundary as these cause a shift in cirumferential averages and, hence, interfere with the control of mean boundary values.

Subsequently, three basic, two-dimensional test cases have been studied to validate the improved accuracy of the NRBC:

A transonic turbine cascade has shown that reflecting boundary conditions do not only affect unsteady waves, but can also impair the prediction of the underlying mean flow. In this case, the prediction of a suction-sided shock is subject to artificial reflections at the outflow boundary unless an accurate NRBC is used. This has a significant impact on the blade pressure distribution. Even though the NRBC are derived from the linearized Euler equations, the spectral NRBC exhibit little sensitivity to a variation of the boundary location in presence of a shock, indicating still low levels of artificial reflections.

The second test case demonstrated the capability of the spectral NRBC to impose incoming modes. By studying a single acoustic mode in a thin, circular duct, a quantitative analysis of reflection coefficients of different boundary conditions was presented. The generally better accuracy of the spectral NRBC in comparison to existing boundary conditions could be underlined. Especially in situations, in which existing boundary conditions are known to perform poorly, the spectral NRBC offer a reduction of spurious reflections by at least a factor of 10. Moreover, it has been shown that a variation of the unsteady pressure amplitude from 0.02 % to 20 % of the mean flow pressure leads to less then 3 % difference in the reflection coefficient. This supports the above observation, that the spectral NRBC remain reasonably accurate for relatively large perturbations despite their linear nature.

An academic flutter test case called tenth standard configuration, which is known to be sensitive to reflections from boundary conditions, has also supported the increased accuracy of the spectral NRBC. With these NRBC, very good agreement with widely accepted reference results has been achieved whereas existing, approximate NRBC fail to meet the reference results, especially under conditions close to acoustic resonance. In particular, the critical point of minimal aerodynamic damping is not well predicted by the approximate NRBC. Moreover, identical results of single-passage simulations using phase-shifted periodic boundaries and truly periodic multi-passage simulations have verified that the spectral NRBC is correctly implemented for both approaches.

Beyond these academic validation test cases, two more realistic turbomachinery applications have been presented.

Very similar conclusions to those from the tenth standard configuration can be drawn from a flutter analysis of a transonic low pressure steam turbine rotor blade. Only the results obtained with the spectral NRBC agree well with reference results, particularly in the unstable region of negative aerodynamic damping. Moreover, the analysis has been performed with and without a downstream (bladeless) diffuser section. In contrast to a one-dimensional NRBC, the spectral, two-dimensional NRBC shows very similar results for both domains, confirming the strong suppression of spurious reflections when using the spectral NRBC in this demanding, three-dimensional case where a trailing edge shock interacts with the outflow boundary. Convergence is slightly lagged with the spectral NRBC as they depend temporal Fourier coefficients, which need to be evaluated in a transient manner. On the other hand, the use of an accurate NRBC allows a smaller computational domain which in turn reduces the computational effort and leads to faster convergence. Therefore it cannot be concluded that

the spectral NRBC generally increase the computational costs due to slower convergence. Additionally, a comparison of time domain and harmonic balance results with consistent spectral NRBC has been presented. The agreement is excellent.

Also, an application considering the unsteady blade row interaction in a modern, transonic compressor has proven the practical usability of the presented NRBC for realistic turbomachinery flows. With the spectral NRBC, reference results from a much more expensive full-wheel, multi-stage simulation could be well reproduced on reduced computational domains. Again, a comparison to harmonic balance simulations has been presented. The agreement is very good as well. However, harmonic balance simulations do typically not resolve all possible interaction modes in multi-row configurations. Therefore, a detailed analysis has identified local differences that can be explained by modes which are not taken into account by the specific harmonic balance setup. This showcases that for complex configurations, time domain simulations are the more universal tool, yet the impact on unsteady blade pressure is small in this case. Furthermore, it has been shown that wakes can induce acoustic reflections. However, this reflection is much more pronounced with a less accurate one-dimensional NRBC and the impact on the respective unsteady blade pressure distribution is small for the spectral NRBC in this case.

Altogether it can be concluded that the spectral NRBC have been successfully implemented in TRACE. The NRBC is characterized by significantly reduced artificial reflections even in three-dimensional flows with nonlinear phenomena. Stability or convergence issues due to the boundary condition have not been observed with any of the test cases and applications presented in this work. This is a critical advancement compared to the few other attempts of implementing such NRBC into time domain solvers found in the literature, where stability issues and drastically slowed convergence have been reported even for simple duct flows.

The additional computational costs of this NRBC appear acceptable. In smaller setups, the overhead regarding CPU time per time step and memory requirements is negligible. However, convergence is usually reached a bit later than with local, approximate boundary conditions. Yet, the high accuracy of the NRBC permits the use of smaller computational domains which can remedy delayed convergence or even yield reduced overall costs depending on the configuration at hand. For larger setups, in particular when low base frequencies are resolved with many time steps, memory consumption and computational overhead grow substantially unless the user is able to specify relevant frequencies a-priori. In this case, the computational effort and memory requirements are comparable to local boundary conditions.

Future developments could address this topic, e.g. by automatically reducing the frequency spectrum of the NRBC by means of an on-the-fly amplitude estimation and filtering of insignificant modes. An extension to almost periodic Fourier transformations could provide an automatic detection of relevant frequencies even beyond spectra that consist of harmonics of a common base frequency (see Battistoni *et al.*, 2022). This would enable an accurate analysis of interactions between turbomachinery components with unrelated shaft speeds or other non-synchronous effects.

The author of this thesis is optimistic that it is possible to find a more efficient way of controlling mean boundary values. In the current form, the control law reacts proportionally to deviations of temporally and spatially averaged mean quantities from specified target values. For large configurations with low base frequencies and, hence, large averaging periods, these averages develop with a significant time lag. This in itself adverse condition necessitates additional relaxation of the control law in order to

prevent overshooting or loss of stability. However, this issue is not specific to the spectral NRBC presented in this thesis, but applies to all unsteady boundary conditions controlling a time-averaged boundary value.

Bibliography

Abarbanel, S., Gottlieb, D. & Hesthaven, J. 1999 Well-posed perfectly matched layers for advective acoustics. *Journal of Computational Physics* **154** (2), 266–283.

van Albada, G. D., van Leer, B. & Roberts, Jr., W. W. 1982 A comparative study of computational methods in cosmic gas dynamics. *Astron. Astrophys.* **108** (1), 76–84.

Alpert, B., Greengard, L. & Hagstrom, T. 2002 Nonreflecting boundary conditions for the time-dependent wave equation. *Journal of Computational Physics* **180** (1), 270–296.

Amecke, J. 1967 Auswertung von Nachlaufmessungen an ebenen Schaufelgittern. Technischer Bericht 67A49. *Tech. Rep.*. AVA, Göttingen, Germany.

Arts, T., Lambertderouvroit, M. & Rutherford, A. W. 1990 Aero-thermal investigation of a highly loaded transonic linear turbine guide vane cascade. A test case for inviscid and viscous flow computations, VKI Technical Note 174.

Arts, T. & Lambert de Rouvroit, M. 1992 Aero-Thermal Performance of a Two-Dimensional Highly Loaded Transonic Turbine Nozzle Guide Vane: A Test Case for Inviscid and Viscous Flow Computations. *Journal of Turbomachinery* **114** (1), 147–154.

Ashcroft, G., Frey, C., Heitkamp, K. & Weckmüller, C. 2012 Advanced numerical methods for the prediction of tonal noise in turbomachinery, Part I: Implicit Runge Kutta schemes. *ASME Paper No. GT2012-69447* .

Ashcroft, G., Frey, C., Heitkamp, K. & Weckmüller, C. 2013 Advanced numerical methods for the prediction of tonal noise in turbomachinery–part I: Implicit Runge-Kutta schemes. *J. Turbomach.* **136** (2), 021002–021002.

Ashcroft, G., Frey, C., Kersken, H.-P., Kügeler, E. & Wolfrum, N. 2018 On the simulation of unsteady turbulence and transition effects in a multistage low pressure turbine, part i: Verification and validation. In *Proceedings of the ASME Turbo Expo 2018*.

Ashcroft, G. & Schulz, J. 2004 Numerical modelling of wake-jet interaction with application to active noise control in turbomachinery. In *10th AIAA/CEAS Aeroacoustics Conference*.

Bardina, J., Ferziger, J. H. & Rogallo, R. S. 1985 Effect of rotation on isotropic turbulence: computation and modelling. *J. Fluid Mech.* **154**, 321–336.

Battistoni, C., Müller, H., Wolfrum, N. & Ashcroft, G. 2022 Numerical simulation of turbomachinery flows considering two-spool effects: Application of the almost-periodic fourier transform. In *AIAA SCITECH 2022 Forum*.

Bayliss, A. & Turkel, E. 1982 Far field boundary conditions for compressible flows. *Journal of Computational Physics* **48** (2), 182–199.

Becker, K., Heitkamp, K. & Kügeler, E. 2010 Recent progress in a hybrid-grid CFD solver for turbomachinery flows. In *Proceedings Fifth European Conference on Computational Fluid Dynamics ECCOMAS CFD 2010*. Lisbon, Portugal.

Berenger, J.-P. 1994 A perfectly matched layer for the absorption of electromagnetic waves. *Journal of Computational Physics* **114** (2), 185–200.

Bergmann, M., Gölden, R. & Morsbach, C. 2018 Numerical investigation of split form nodal discontinuous galerkin schemes for the implicit les of a turbulence channel flow. *7th European Conference on Computational Fluid Dynamics* .

Bergmann, M., Morsbach, C. & Ashcroft, G. 2020 Assessment of split form nodal discontinuous galerkin schemes for the les of a low pressure turbine profile. In *Direct and Large Eddy Simulation XII*, pp. 365–371. Springer International Publishing.

Berthold, C., Groß, J., Frey, C. & Krack, M. 2022 Fully Coupled Analysis of Flutter Induced Limit Cycles: Frequency vs. Time Domain Methods. In *Proceedings of the ASME Turbo Expo 2022*.

Blazek, J. 2001 *Computational fluid dynamics: principles and applications*. Elsevier Science.

Brind, J. & Pullan, G. 2020 Effect of Blade Row Interaction on Rotor Film Cooling. *Journal of Turbomachinery* **142** (9), 091011.

Burton, Z. 2014 Analysis of low pressure steam turbine diffuser and exhaust hood systems. PhD thesis, Durham University.

Bécache, E., Fauqueux, S. & Joly, P. 2003 Stability of perfectly matched layers, group velocities and anisotropic waves. *Journal of Computational Physics* **188** (2), 399–433.

Chassaing, J. & Gerolymos, G. 2004 Time-domain implementation of nonreflecting boundary-conditions for the nonlinear euler equations. In *10 th AIAA/CEAS Aeroacoustics Conference*.

Chassaing, J. & Gerolymos, G. 2007 Time-domain implementation of nonreflecting boundary-conditions for the nonlinear euler equations. *Applied mathematical modelling* **31** (10), 2172–2188.

Chernysheva, O. V. 2004 Flutter in sectored turbine vanes. PhD thesis, KTH, Energy Technology, Stockholm.

Chilla, M., Hodson, H. & Newman, D. 2013 Unsteady Interaction Between Annulus and Turbine Rim Seal Flows. *Journal of Turbomachinery* **135** (5), 051024.

Chuang, H. A. & Verdon, J. M. 1999 A Nonlinear Numerical Simulator for Three-Dimensional Flows Through Vibrating Blade Rows. *Journal of Turbomachinery* **121**.

Clark, W. S. & Hall, K. C. 1999 A Time-Linearized Navier–Stokes Analysis of Stall Flutter . *Journal of Turbomachinery* **122** (3), 467–476.

Collado Morata, E., Gourdain, N., Duchaine, F. & Gicquel, L. 2012 Effects of free-stream turbulence on high pressure turbine blade heat transfer predicted by structured and unstructured les. *International Journal of Heat and Mass Transfer* **55** (21), 5754–5768.

Collino, F. 1993 High order absorbing boundary conditions for wave propagation models. straight line boundary and corner cases. In *Second International Conference on Mathematical and Numerical Aspects of Wave Propagation (Newark)*, pp. 161–171.

Colonius, T. 2004 Modeling artificial boundary conditions for compressible flow. *Annual Review of Fluid Mechanics* **36** (1), 315–345.

Colonius, T. & Lele, S. K. 2004 Computational aeroacoustics: progress on nonlinear problems of sound generation. *Progress in Aerospace Sciences* **40** (6), 345–416.

Colonius, T., Lele, S. K. & Moin, P. 1993 Boundary conditions for direct computation of aerodynamic sound generation. *AIAA Journal* **31** (9), 1574–1582.

Cosmo, G. D. & Salvadori, S. 2019 Implementation of non-reflecting boundary conditions in a finite volume unstructured solver for the study of turbine cascades. *13th European Conference on Turbomachinery Fluid Dynamics and Thermodynamics* .

Courant, R., Friedrichs, K. & Lewy, H. 1928 Über die partiellen Differenzengleichungen der mathematischen Physik. *Math. Ann.* **100**, 32–74.

Crank, J. & Nicolson, P. 1947 A practical method for numerical evaluation of solutions of partial differential equations of the heat-conduction type. In *Proceedings of the Cambridge Philosophical Society*, , vol. 43, pp. 50–67. Cambridge University Press.

Crespo, J., Corral, R. & Pueblas, J. 2015 An Implicit Harmonic Balance Method in Graphics Processing Units for Oscillating Blades. *Journal of Turbomachinery* .

Cumpsty, N. A. & Horlock, J. H. 2006 Averaging nonuniform flow for a purpose. *J. Turbomach.* **128** (1), 120–129.

Dahmen, W. & Reusken, A. 2008 *Numerik für Ingenieure und Naturwissenschaftler*. Berlin Heidelberg New York: Springer-Verlag.

Dowell, E. H. 2015 *A Modern Course in Aeroelasticity*. Springer International Publishing.

Dzung, L. 1971 Konsistente Mittelwerte in der Theorie der Turbomaschinen für kompressible Medien. *BBC-Mitteilungen* **58**, 485–492.

Ekici, K. & Hall, K. C. 2007 Nonlinear analysis of unsteady flows in multistage turbomachines using harmonic balance. *AIAA J.* **45** (5), 1047–1057, aIAA 44th Aerospace Sciences Meeting and Exhibit, Reno, NV, JAN 09-12, 2006.

Engquist, B. & Majda, A. 1977 Absorbing boundary conditions for the numerical simulation of waves. *Math. Comp.* **31** (5), 629–651.

Erdos, J. I., Alzner, E. & McNally, W. 1977 Numerical solution of periodic transonic flow through a fan stage. *AIAA J.* **15** (11), 1559–1568.

Fan, S. & Lakshminarayana, B. 1996 Time-Accurate Euler Simulation of Interaction of Nozzle Wake and Secondary Flow With Rotor Blade in an Axial Turbine Stage Using Nonreflecting Boundary Conditions. *Journal of Turbomachinery* **118** (4), 663–678.

Franke, M., Röber, T., Kügeler, E. & Ashcroft, G. 2010 Turbulence treatment in steady and unsteady turbomachinery flows. In *Proceedings Fifth European Conference on Computational Fluid Dynamics ECCOMAS CFD 2010*. Lisbon, Portugal.

Fransson, T. H., Jöker, M., Bölcs, A. & Ott, P. 1999 Viscous and Inviscid Linear/Nonlinear Calculations Versus Quasi-Three-Dimensional Experimental Cascade Data for a New Aeroelastic Turbine Standard Configuration. *Journal of Turbomachinery* **121** (4), 717–725.

Fransson, T. H. & Verdon, J. M. 1992 Updated report on Standard Configurations for the Determination of unsteady Flow Through Vibrating Axial-flow Turbomachine-Cascades. *Tech. Rep.* TRITA/KRV/92.009. KTH, Stockholm.

Frey, C., Ashcroft, G. & Kersken, H.-P. 2015 Simulations of unsteady blade row interactions using linear and non-linear frequency domain methods. In *ASME Turbo Expo 2015: Turbine Technical Conference and Exposition*.

Frey, C., Ashcroft, G., Kersken, H.-P. & Schlüß, D. 2019 Flutter analysis of a transonic steam turbine blade with frequency and time-domain solvers. *International Journal of Turbomachinery, Propulsion and Power* **4** (2).

Frey, C., Ashcroft, G., Kersken, H.-P., Schönweitz, D. & Mennicken, M. 2018 Simulation of indexing and clocking with harmonic balance. *Int. J. Turbomach. Propuls. Power* **3** (1).

Frey, C., Ashcroft, G., Kersken, H.-P. & Voigt, C. 2014 A harmonic balance technique for multistage turbomachinery applications. In *ASME Turbo Expo 2014: Turbine Technical Conference and Exposition*.

Frey, C., Ashcroft, G., Kersken, H.-P. & Weckmüller, C. 2012 Advanced numerical methods for the prediction of tonal noise in turbomachinery, Part II: Time-linearized methods. In *Proceedings of ASME-GT2012*.

Frey, C., Ashcroft, G., Kersken, H.-P. & Weckmüller, C. 2013 Advanced numerical methods for the prediction of tonal noise in turbomachinery — Part II: Time-linearized methods. *J. Turbomach.* **136** (2), 021002.

Frey, C. & Kersken, H.-P. 2016 On the regularisation of non-reflecting boundary conditions near acoustic resonance. In *ECCOMAS Congress 2016 VII European Congress on Computational Methods in Applied Sciences and Engineering, Crete Island, Greece*.

Frey, C., Schlüß, D., Wolfrum, N., Bechlars, P. & Beck, M. 2020 On the formulation of nonreflecting boundary conditions for turbomachinery configurations: Part i—theory and implementation. In *ASME Turbo Expo 2020: Turbomachinery Technical Conference and Exposition*. American Society of Mechanical Engineers Digital Collection.

Gallardo, J. M., Sotillo, A. & Bermejo, O. 2019 Study of the Effect of the Scatter of Acoustic Modes on Turbine Flutter. *Journal of Turbomachinery* .

Geiser, G., Wellner, J., Kügeler, E., Weber, A. & Moors, A. 2019 On the simulation and spectral analysis of unsteady turbulence and transition effects in a multistage low pressure turbine. *Journal of Turbomachinery* **141** (5).

German Aerospace Center 2021 *DLR's new aviation strategy: Towards zero-emission aviation*.

Gerolymos, G. A., Michon, G. J. & Neubauer, J. 2002 Analysis and application of chorochronic periodicity in turbomachinery rotor/stator interaction computations. *Journal of Propulsion and Power* **18** (6), 1139–1152.

Giles, M. 1991 UNSFLO: A numerical method for the calculation of unsteady flow in turobmachinery. *Tech. Rep.*. Gas Turbine Laboratory Report GTL 205, MIT Dept. of Aero. and Astro.

Giles, M. B. 1988 Non-reflecting boundary conditions for the Euler equations. *Tech. Rep.*. MIT Dept. of Aero. and Astr., CFDL Report 88-1.

Giles, M. B. 1990 Nonreflecting boundary conditions for Euler calculations. *AIAA J.* **28** (12), 2050–2058.

Givoli, D. 1991 Non-reflecting boundary conditions. *Journal of Computational Physics* **94** (1), 1–29.

Givoli, D. 2004 High-order local non-reflecting boundary conditions: a review. *Wave Motion* **39** (4), 319–326.

Goinis, G., Voß, C. & Nicke, E. 2021 The potential of casing treatments for transonic compressors: Evaluation based on axial-slot and rotor blade optimization. In *32nd Congress of the International Council of the Aeronautical Sciences*.

Goodrich, J. & Hagstrom, T. 1996 Accurate algorithms and radiation boundary conditions for linearized euler equations. In *AIAA and CEAS Aeroacoustics Conference*, p. 1660.

Gourdain, N., Duchaine, F., Gicquel, L. Y. M. & Collado, E. 2010 Advanced Numerical Simulation Dedicated to the Prediction of Heat Transfer in a Highly Loaded Turbine Guide Vane. In *Proceedings of ASME Turbo Expo 2010*, pp. 807–820.

Hagstrom, T. 1997 On high-order radiation boundary conditions. In *Computational Wave Propagation* (ed. B. Engquist & G. A. Kriegsmann), pp. 1–21. Springer.

Hagstrom, T. & Goodrich, J. 2003 Accurate radiation boundary conditions for the linearized euler equations in cartesian domains. *SIAM Journal on Scientific Computing* **24** (3), 770–795.

Hagstrom, T., Goodrich, J., Nazarov, I. & Dodson, C. 2005 High-order methods and boundary conditions for simulating subsonic flows. In *11th AIAA/CEAS Aeroacoustics Conference*, p. 2869.

Hall, K. & Clark, W. 1991 Prediction of unsteady aerodynamic loads in cascades using the linearized euler equations on deforming grids. In *27th Joint Propulsion Conference*.

Hall, K., Lorence, C. & Clark, W. 1993 *Nonreflecting boundary conditions for linearized unsteady aerodynamic calculations*.

Hall, K. C. 1987 A linearized Euler analysis of unsteady flows in turbomachinery. PhD thesis, Massachusetts Institute of Technology.

Hall, K. C. & Crawley, E. F. 1989 Calculation of unsteady flows in turbomachinery using the linearizedeuler equations. *AIAA Journal* **27** (6), 777–787.

Hall, K. C., Thomas, J. P. & Clark, W. S. 2002 Computation of unsteady nonlinear flows in cascades using a harmonic balance technique. *AIAA J.* **40** (5), 879–886.

He, L. 1990 An euler solution for unsteady flows around oscillating blades. *J. Turbomach.* **112** (4), 714–722.

He, L. 1992 Method of simulating unsteady turbomachinery flows with multiple perturbations. *AIAA J.* **30** (11), 2730–2735.

He, L. & Ning, W. 1998 Efficient approach for analysis of unsteady viscous flows in turbomachines. *AIAA J.* **36** (11), 2005–2012.

Hedstrom, G. 1979 Nonreflecting boundary conditions for nonlinear hyperbolic systems. *Journal of Computational Physics* **30** (2), 222–237.

Heners, J. P. 2022 *A Lanczos-filtered harmonic balance method for aeroelastic applications of turbomachinery resolving unsteady turbulence effects*. Aachen, Germany: Shaker Verlag.

Heners, J. P., Frey, C., Grüber, B. & Carraro, T. 2022 Evaluating the Aerodynamic Damping At Shock Wave Boundary Layer Interacting Flow Conditions With Harmonic Balance. *Journal of Engineering for Gas Turbines and Power* **145** (3), 031012.

Heners, J. P., Vogt, D. M., Frey, C. & Ashcroft, G. 2019 Investigation of the impact of unsteady turbulence effects on the aeroelastic analysis of a low-pressure turbine rotor blade. *Journal of Turbomachinery* pp. 1–12.

Henninger, S. 2019 Zeitbereichsimplementierung höherwertiger nichtreflektierender Randbedingungen für die Simulation instationärer Turbomaschinenströmungen; 1. Auflage. PhD thesis, RWTH Aachen University.

Henninger, S., Jeschke, P., Ashcroft, G. & Kügeler, E. 2015 Time-domain implementation of higher-order non-reflecting boundary conditions for turbomachinery applications. In *Proceedings of ASME Turbo Expo 2013*.

Higdon, R. L. 1986*a* Absorbing boundary conditions for difference approximations to the multidimensional wave equation. *Mathematics of Computation* **47** (176), 437–459.

Higdon, R. L. 1986*b* Initial-boundary value problems for linear hyperbolic systems. *SIAM Rev.* **28** (2), 177–217.

Hirsch, C. 1990 *Numerical Computation of Internal and External Flows, Volume 2: Computational Methods for Inviscid and Viscous Flows*. Wiley & Sons Ltd.

Hirsch, C. 2007 *Numerical Computation of Internal and External Flows, Volume 1: Fundamentals of Computational Fluid Dynamics*. Elsevier.

Hu, F. Q. 1996 On absorbing boundary conditions for linearized euler equations by a perfectly matched layer. *Journal of Computational Physics* **129** (1), 201–219.

Hu, F. Q. 2005 A perfectly matched layer absorbing boundary condition for linearized euler equations with a non-uniform mean flow. *Journal of Computational Physics* **208** (2), 469–492.

Huang, H. 2013 Shape optimization of turbomachinery blades using an adjoint harmonic balance method. PhD thesis, University of Tennessee.

Huang, H. & Ekici, K. 2014 Stabilization of high-dimensional harmonic balance solvers using time spectral viscosity. *AIAA J.* **52** (8), 1784–1794.

Junge, L., Ashcroft, G., Jeschke, P. & Frey, C. 2015 On the application of frequency-domain methods to multistage turbomachinery. In *Proceedings of the ASME Turbo Expo 2015*.

Junge, L., Ashcroft, G., Kersken, H.-P. & Frey, C. 2018 On the development of harmonic balance methods for multiple fundamental frequencies. In *Proceedings of the ASME Turbo Expo 2018*.

Junge, L., Frey, C., Ashcroft, G. & Kügeler, E. 2021 A New Harmonic Balance Approach Using Multidimensional Time. *Journal of Engineering for Gas Turbines and Power* **143** (8), 081007.

Kahl, G. & Klose, A. 1993 Computation of Time Linearized Transonic Flow in Oscillating Cascades. In *Proceedings of the ASME 1993 International Gas Turbine and Aeroengine Congress and Exposition, Turbo Expo: Power for Land, Sea, and Air*, vol. Volume 3B: General.

Karni, S. 1996 Far-field filtering operators for suppression of reflection from artificial boundaries. *SIAM Journal on Numerical Analysis* **33** (3), 1014–1047.

Kato, M. & Launder, B. E. 1993 The modeling of turbulent flow around stationary and vibrating square cylinders. In *9th Symposium on Turbulent Shear Flows*, pp. 10.4.1–10.4.6.

Keiner, J., Kunis, S. & Potts, D. 2009 Using nfft 3—a software library for various nonequispaced fast fourier transforms. *ACM Trans. Math. Softw.* **36** (4).

Kersken, H.-P., Ashcroft, G., Frey, C., Wolfrum, N. & Korte, D. 2014 Nonreflecting boundary conditions for aeroelastic analysis in time and frequency domain 3D RANS solvers. In *Proceedings of ASME Turbo Expo 2014*.

Kersken, H.-P., Frey, C., Voigt, C. & Ashcroft, G. 2012 Time-linearized and time-accurate 3D RANS methods for aeroelastic analysis in turbomachinery. *J. Turbomach.* **134** (5), 051024.

Klose, B., Morsbach, C., Bergmann, M. & Kügeler, E. 2022 Implicit les of the transonic flow over a high-pressure turbine cascade using dg subcell shock capturing. In *ECCOMAS Congress 2022*.

Kozulovic, D. 2007 Modellierung des Grenzschichtumschlags bei Turbomaschinenströmungen unter Berücksichtigung mehrerer Umschlagsarten. Phd thesis, Ruhr-Universität Bochum, also DLR-FB 2007-20.

Kreiss, H.-O. 1970 Initial boundary value problems for hyperbolic systems. *Communications on Pure and Applied Mathematics* **23** (3), 277–298.

KTH Website 2021 3D Steam Turbine Flutter Test Case, Department of Energy Technology, KTH Royal Institute of Technology, Stockholm, Sweden. Online; Accessed on 02-02-2021.

Kügeler, E., Geiser, G., Wellner, J., Weber, A. & Moors, A. 2018 On the Simulation of Unsteady Turbulence and Transition Effects in a Multistage Low Pressure Turbine: Part III — Comparison of Harmonic Balance and Full Wheel Simulation. In *Proceeding of the ASME TurboExpo 2018*.

Langtry, R. & Menter, F. 2009 Correlation-based transition modeling for unstructured parallelized computational fluid dynamics codes. *AIAA J.* **47** (12), 2894–2906.

van Leer, B. 1979 Towards the ultimate conservative difference scheme. V. A second-order sequel to Godunov's method. *J. Comput. Phys.* **32** (1), 101 – 136.

LeVeque, R. J. 2002 *Finite Volume Methods for Hyperbolic Problems*, 1st edn. New York, NY, USA: Cambridge University Press.

Lindblad, D. 2020 Numerical methods for aeroacoustic analysis of turbomachines. PhD thesis, Chalmers University Of Technology.

Lindblad, D., Wukie, N., Villar, G. M. & Andersson, N. 2019 *A Nonreflecting Formulation for Turbomachinery Boundaries and Blade Row Interfaces*.

Majda, A. & Osher, S. 1975 Initial-boundary value problems for hyperbolic equations with uniformly characteristic boundary. *Communications on Pure and Applied Mathematics* **28** (5), 607–675.

Marciniak, V. 2016 Phenomenological transition modelling for turbomachinery flows. PhD thesis, Ruhr-Universität Bochum.

McMullen, M. S. 2003 The application of non-linear frequency domain methods to the Euler and Navier-Stokes equations. Phd thesis, Stanford University.

Mennicken, M., Schoenweitz, D., Schnoes, M. & Schnell, R. 2022 Fan design assessment for bli propulsion systems. *CEAS Aeronautical Journal* **13** (1), 3–19.

Message Passing Interface Forum 2005 MPI: A Message-Passing Interface Standard, Version 3.1. *Tech. Rep.*. University of Tennesse.

Moinier, P. & Giles, M. 2005 Eigenmode analysis for turbomachinery applications. *J. Propul. Power* **21** (6), 973–978.

Moinier, P., Giles, M. B. & Coupland, J. 2007 Three-dimensional nonreflecting boundary conditions for swirling flow in turbomachinery. *J. Propul. Power* **23** (5), 981–986.

Montgomery, M. D. & Verdon, J. M. 1997 A three-dimensional linearized unsteady euler analysis for turbomachinery blade rows. *Tech. Rep.* NASA CR-4770. United Technologies Research Center, East Hartford, Connecticut, USA.

Morsbach, C. 2016 Reynolds stress modelling for turbomachinery flow applications. Phd thesis, TU Darmstadt.

Morsbach, C. & Bergmann, M. 2020 Critical analysis of the numerical setup for the large-eddy simulation of the low-pressure turbine profile t106c. In *Direct and Large Eddy Simulation XII*, pp. 343–348. Springer International Publishing.

Mueller, T. R., Vogt, D. M., Fischer, M. & Phillipsen, B. A. 2021 On the far-field boundary condition treatment in the framework of aeromechanical computations using ansys cfx. *Proceedings of the Institution of Mechanical Engineers, Part A: Journal of Power and Energy* **235** (5), 1103–1118.

Müller, M., Kersken, H.-P. & Frey, C. 2022 A log-ω turbulence model formulation for flutter analysis with harmonic balance. *16th International Symposium on Unsteady Aerodynamics, Aeroacoustics & Aeroelasticity of Turbomachines (ISUAAAT16)* .

Mårtensson, H. 2021 Harmonic forcing from distortion in a boundary layer ingesting fan. *Aerospace* **8** (3).

Nürnberger, D. 2004 Implizite Zeitintegration für die Simulation von Turbomaschinenströmungen. Dissertation, Ruhr-Universität Bochum.

Petrie-Repar, P., Makhnov, V., Shabrov, N., Smirnov, E., Galaev, S. & Eliseev, K. 2014 Advanced flutter analysis of a long shrouded steam turbine blade. In *Proceedings of the ASME Turbo Expo 2014: Turbine Technical Conference and Exposition*, pp. V07BT35A022–V07BT35A022. American Society of Mechanical Engineers.

Petrie-Repar, P. J. 2010 Three-dimensional non-reflecting boundary condition for linearized flow solvers. In *Proceedings of the ASME Turbo Expo 2010: Power for Land, Sea, and Air*, pp. 1247–1252. American Society of Mechanical Engineers.

Petrie-Repar, P. J., McGhee, A., Jacobs, P. A. & Gollan, R. 2006 Analytical maps of aerodynamic damping as a function of operating condition for a compressor profile. In *Proceedings of the ASME Turbo Expo 2006.*

Petrie-Repar, P. J., McGhee, A. M. & Jacobs, P. A. 2007 Three-dimensional viscous flutter analysis of standard configuration 10. In *Proceedings of the ASME Turbo Expo 2007.*

Pianko, M. & Wazelt, F. 1983 Suitable averaging techniques in non-uniform internal flows. *Tech. Rep..* AGARD AR, Propulsion and Energetic Panel Working Group, no. 182.

Poinsot, T. & Lele, S. K. 1992 Boundary conditions for direct simulations of compressible viscous flows. *Journal of Computational Physics* **101** (1), 104–129.

Prasad, A. 2005 Calculation of the mixed-out state in turbomachine flows. *J. Turbomach.* **127** (3), 564–572.

Qi, D., Petrie-Repar, P., Gezork, T. & Sun, T. 2017 Establishment of an open 3D steam turbine flutter test case. In *Proceedings of 12th European Conference on Turbomachinery Fluid dynamics & Thermodynamics.*

Rai, M. M. & Moin, P. 1993 Direct numerical simulation of transition and turbulence in a spatially evolving boundary layer. *Journal of Computational Physics* **109** (2), 169–192.

Reutter, O., Ashcroft, G., Nicke, E. & Kügeler, E. 2018 Comparison of experiments, full-annulus calculations and harmonic-balance-calculations of a multi-stage compressor. In *Proceedings of Montreal 2018 Global Power and Propulsion Forum.*

Rienstra, S. W. 1999 Sound transmission in slowly varying circular and annular lined ducts with flow. *J. Fluid Mech.* **380**, 279–296.

Roe, P. L. 1981 Approximate Riemann solvers, parameter vectors, and difference schemes. *J. Comput. Phys.* **43** (2), 357 – 372.

Rowley, C. W. & Colonius, T. 2000 Discretely nonreflecting boundary conditions for linear hyperbolic systems. *Journal of Computational Physics* **157** (2), 500–538.

Rudy, D. H. & Strikwerda, J. C. 1980 A nonreflecting outflow boundary condition for subsonic navier-stokes calculations. *Journal of Computational Physics* **36** (1), 55–70.

Sanders, C., Terstegen, M., Jeschke, P., Schoenenborn, H. & Heners, J. P. 2019 Rotor–Stator Interactions in a 2.5-Stage Axial Compressor—Part II: Impact of Aerodynamic Modeling on Forced Response. *Journal of Turbomachinery* **141** (10), 101008.

Saxer, A. P. & Giles, M. B. 1993 Quasi-three-dimensional nonreflecting boundary conditions for Euler equations calculations. *J. Propul. Power* **9** (2), 263–271.

Schlüß, D. & Frey, C. 2018 Time domain flutter simulations of a steam turbine stage using sptectral 2d non-reflecting boundary conditions. In *15th International Symposium on Unsteady Aerodynamics, Aeroacoustics & Aeroelasticity of Turbomachines (ISUAAAT15).*

Schlüß, D., Frey, C. & Ashcroft, G. 2016 Consistent non-reflecting boundary conditions for both steady and unsteady flow simulations in turbomachinery applictations. In *VII European Congress on Computational Methods in Applied Sciences and Engineering (ECCOMAS Congress 2016).*

Schlüß, D. & Frey, C. 2018 Mixing losses in steady and unsteady simulations of turbomachinery flows. In *Proceedings of the ASME Turbo Expo 2018.*

Schlüß, D. & Frey, C. 2019 Time domain implementation of a spectral non-reflecting boundary condition for unsteady turbomachinery flows. *Proceedings of the 24th IS-ABE Conference .*

Schnell, R. 2004 Numerische Simulation des akustischen Nahfeldes einer Triebwerksgebläsestufe. Phd thesis.

Schoenenborn, H. & Ashcroft, G. 2014 Comparison of non-linear and linearized CFD analysis of the stator-rotor interaction of a compressor stage. In *Proceedings of ASME Turbo Expo 2014.*

Schuepbach, P., Abhari, R. S., Rose, M. G. & Gier, J. 2010 Influence of Rim Seal Purge Flow on the Performance of an Endwall-Profiled Axial Turbine. *Journal of Turbomachinery* **133** (2), 021011.

Segui, L., Gicquel, L., Duchaine, F. & de Laborderie, J. 2017 Les of the ls89 cascade: influence of inflow turbulence on the flow predictions. In *European conference on turbomachinery fluid dynamics & thermodynamics.*

Sivel, P. 2018 Analysis of spectral non-reflecting boundary conditions for unsteady simulations of turbomachinery flows in terms of predictive quality and computational effort. Master's thesis, RWTH Aachen University.

Sotillo, A. & Gallardo, J. M. 2018 Study of the Impact of Multi-Row Interaction on Flutter Analysis for a Representative LPT Geometry. In *Proceedings of the ASME Turbo Expo 2018: Turbine Technical Conference and Exposition.* V07CT36A011.

Steelant, J. & Dick, E. 2000 Modeling of Laminar-Turbulent Transition for High Freestream Turbulence . *Journal of Fluids Engineering* **123** (1), 22–30.

Sun, T., Petrie-Repar, P. & Qi, D. 2017 Investigation of tip clearance flow effects on an open 3d steam turbine flutter test case. In *ASME TurboExpo 2017*, pp. V008T29A024–.

Sun, T., Petrie-Repar, P., Vogt, D. M. & Hou, A. 2019 Detached-Eddy Simulation Applied to Aeroelastic Stability Analysis in a Last-Stage Steam Turbine Blade. *Journal of Turbomachinery* **141** (9).

Ta'asan, S. & Nark, D. 1995 An absorbing buffer zone technique for acoustic wave propagation. In *33rd AIAA Aerospace Sciences Meeting and Exhibit*.

Terstegen, M., Sanders, C., Jeschke, P. & Schoenenborn, H. 2019 Rotor–Stator Interactions in a 2.5-Stage Axial Compressor—Part I: Experimental Analysis of Tyler–Sofrin Modes. *Journal of Turbomachinery* **141** (10), 101002.

Thompson, K. W. 1987 Time dependent boundary conditions for hyperbolic systems. *Journal of Computational Physics* **68** (1), 1–24.

Thompson, K. W. 1990 Time-dependent boundary conditions for hyperbolic systems, ii. *Journal of Computational Physics* **89** (2), 439–461.

Toro, E. F. 1999 *Riemann solvers and numerical methods for fluid dynamics*, 2nd edn. Berlin, Germany: Springer.

Tyler, J. M. & Sofrin, T. G. 1962 Axial flow compressor noise studies. *Transactions of the Society of Automotive Engineers* **70**, 309–332.

Vagnoli, S. 2016 Assessment of advanced numerical methods for the aero-thermal investigation of combustor-turbine interactions. PhD thesis, University of Florence.

Vahdati, M., Sayma, A. I., Imregun, M. & Simpson, G. 2005 Multibladerow Forced Response Modeling in Axial-Flow Core Compressors. *Journal of Turbomachinery* **129** (2), 412–420.

Vahdati, M., Zhao, F. & Sureshkumar, P. 2019 A review of computational methods for aeroelastic instabilities of multi-stage compressor. In *Proceedings of Global Power and Propulsion Society*.

Verdon, J., Caspar, J. & Adamczyk, J. 1975 Subsonic flow past an oscillating cascade with steady blade loading - basic formulation. In *Unsteady Aerodynamics* (ed. R. B. Kinney). Univ. of Arizona, Tucson, AZ.

Verdon, J. M. & Caspar, J. R. 1980 Subsonic flow past an oscillating cascade with finite mean flow deflection. *AIAA Journal* **18** (5), 540–548.

Verdon, J. M. & Usab, W. J. 1986 *Application of a linearized unsteady aerodynamic analysis to standard cascade configurations*. National Aeronautics and Space Administration.

Weber, A., Morsbach, C., Kügeler, E., Rube, C. & Wedeking, M. 2016 Flow analyis of a high flowrate centrifugal compressor stage and comparison with test rig data. In *Proceedings of ASME Turbo Expo 2016*. ASME, Seoul, South Korea.

Whitehead, D. S. 1982 The calculation of steady and unsteady transonic flow in cascades. *Tech. Rep.*. Cambridge University Engineering Department, report 118.

Whitham, G. B. 1974 *Linear and Non-linear Waves*. John Wiley and Sons.

Wilcox, D. C. 1988 Reassessment of the scale-determining equation for advanced turbulence models. *AIAA J.* **26** (11), 1299–1310.

Wilcox, D. C. 2006 *Turbulence Modeling for CFD*, 3rd edn. DCW Industries, La Cañada, USA.

Wolfrum, N., Bechlars, P., Beck, M., Frey, C. & Schlüß, D. 2020 On the formulation of nonreflecting boundary conditions for turbomachinery configurations: Part ii—application and analysis. In *ASME Turbo Expo 2020*.

Wukie, N. A., Orkwis, P. D., Lindblad, D. & Andersson, N. 2019 Nonreflecting boundary conditions for the euler equations in a discontinuous galerkin discretization. In *AIAA Scitech 2019 Forum*.

List of Figures

121

List of Tables

Daniel Schlüß

Bildungslebenslauf

Ruhr-Universität Bochum   Bochum
Promotion Dr.-Ing.   Nov. 2018 – Dez. 2023

RWTH Aachen   Aachen
M.Sc. Luft- und Raumfahrttechnik   Apr. 2012 – Nov. 2013

RWTH Aachen   Aachen
B.Sc. Maschinenbau, Vertiefung Luft- und Raumfahrttechnik   Okt. 2008 – Aug. 2012

Bischöfliches St.-Josef-Gymnasium   Bocholt
Allgemeine Hochschulreife   1998 – 2007